2008

Exploration of New Ternary Gallides and Investigation of Their Structure-Property Relationships

Jung Young Cho
Louisiana State University and Agricultural and Mechanical College, jcho1@lsu.edu

EXPLORATION OF NEW TERNARY GALLIDES AND INVESTIGATION OF THEIR STRUCTURE-PROPERTY RELATIONSHIPS

A Dissertation

Submitted to the Graduate Faculty of the
Louisiana State University and
Agricultural and Mechanical College
in partial fulfillment of the
requirements for the degree of
Doctor of Philosophy

In

Department of Chemistry

By
Jung Young Cho
B.S., Chung-Ang University, 2001
M.S., Chung-Ang University, 2003
December 2008

DEDICATION

To my family

and

Especially my lovely wife, Eun Jeong, who supported me in this long journey

ACKNOWLEDGEMENTS

First of all, I thank GOD!

I would like to express my appreciation to my advisor, Professor Julia Y. Chan for her generous and continuous support of my dissertation work. She has provided many opportunities to broaden my academic career and resources to be honored for several awards. She always taught and encouraged me to be an independent scientist. Without her guidance, my success would not have been possible.

I would like to thank my committee members Professor George G. Stanley, Andrew W. Maverick, David P. Young, and Roger A. Laine for your advice and guidance throughout my dissertation work. Special thanks to my collaborators Professor David P. Young, Dr Amar K. Karki, Dr Cidem Capan, Dr Monica Moldovan, Professor John Ditusa, Professor Satoru Nakatsuji, Yuske Nambu, and Kentarou Kuga who shared scientific discussions with me. Also, deep appreciation goes to Dr. Frank Fronczek who was always willing to answer the questions about crystallography. I also would like to thank the Chan group members Edem K. Okudzeto, Dixie P. Gautreaux, Kandace R. Thomas, Jasmine N. Millican, Evan L. Thomas, new colleagues, and undergraduates who worked with me. It was a great pleasure to work with you.

I would like thank my family, especially my wife, Eun Jeong, for their never-ending support and belief in me. Without their thoughtful concern and love, I would not have been successful for my Ph. D. study.

TABLE OF CONTENTS

LIST OF TABLES

LIST OF FIGURES

xi

ABSTRCT

This dissertation focuses on the investigation of new ternary intermetallic gallides, which may exhibit exotic physical properties such as heavy-fermion behavior, large magnetoresistance, and even superconductivity. In particular, the Ln-Cu-Ga (Ln = lanthanides) system has been systematically investigated by changing a reaction ratio and/or using a different temperature profile to optimize desired phases. Single crystals of Ln_2MGa_{12} (Ln = La, Ce; M = Ni, Cu) have been synthesized using Ga flux and compared to their Pd analogues. Interestingly, Ce_2MGa_{12} (M = Ni, Cu) show enhanced Sommerfeld coefficient of $\approx$ 191 mJmol^{-1}K^{-2} and $\approx$ 69 mJmol^{-1}K^{-2} for Ni and Cu compounds, respectively.

Three different structure types such as $Ln(Cu,Ga)_{13}$ (Ln = La − Nd, Eu), $SmCu_4Ga_8$, and $Ln(Cu,Ga)_{12}$ (Ln = Y, Gd − Er, Yb) have been synthesized by increasing Cu concentration. A large positive magnetoresistance up to 154 % at a field of 9 T is observed for $Pr(Cu,Ga)_{13}$. Most interestingly, $Pr(Cu,Ga)_{13}$ shows T^2 temperature-dependent resistivity and satisfies Kadowaki-Woods relation, which is indicative of heavy-fermion behavior. The ordered $SmCu_4Ga_8$ grown by flux method has been compared to its isostructural disordered analogue, $SmCu_{4.1}Ga_{6.9}$. $Ln(Cu,Ga)_{12}$ (Ln = Gd − Er) compounds order antiferromagnetically at 12.5 K, 13.5 K, 6.7 K, and 3.4 K for Gd-, Tb-, Dy-, and Er-analogues, respectively.

Ln_4MGa_{12} (Ln = Dy − Er; M = Pd, Pt) have been grown from Ga flux. Magnetic measurements show that Dy_4PdGa_{12} and Er_4PdGa_{12} are antiferromagnetic with transitions at T_N = 10 K and 5.2 K, respectively, while Ho_4PdGa_{12} does not show any magnetic ordering down to 2 K. Ln_4PtGa_{12} (Ln = Dy − Er) order antiferromagnetically at T_N = 9.8 K, 3.6 K and 5.1 K for Dy-, Ho-, and Er-analogues, respectively. The electrical resistivity data show metallic behavior.

Large positive magnetoresistance is shown up to 900 % at 3 K and 9 T for the Ho_4PtGa_{12} analogue.

Single crystals of $LnAg_yX_{4-y}$ (Ln = La, Ce; X = Al, Ga; $y \approx 0.72$) have been synthesized by aluminum or gallium flux. These compounds show an occupational disorder for Ag sites. $CeAg_{0.72}Al_{3.28}$ and $CeAg_{0.67}Ga_{3.33}$ are metallic, and magnetic measurements indicate that both order ferromagnetically near 3 K.

CHAPTER 1. INTRODUCTION

1.1 Motivation

Strongly correlated electron systems at low temperatures have been of interest during the last four decades because they are responsible for exotic physical properties such as heavy-fermion behavior, magnetism and superconductivity in f-electron intermetallic materials.[1-14] It is well known that the Kondo effect plays an important role in the physics of correlated electron systems which is the spin dependent scattering of conduction electrons by localized magnetic moments.[15] When the magnetic moments such as Fe, Co, or f-electrons in rare earths are surrounded as impurity in nonmagnetic metal environments, the moment can be quenched through the Kondo effect (the spin or angular momentum of the magnetic materials are screened by free electrons through a diamagnetic interaction between spins of the magnetic materials and spins of free electrons).[5,6,15] Also, with the competition between the Kondo effect and the long-range RKKY (Ruderman-Kittel-Kasuya-Yosida) interaction, the possibility of both nonmagnetic and magnetic states can be explained.[16-18] Among various interesting physical properties in strongly correlated electron systems, heavy-fermion superconductivity has attracted much attention since the first heavy fermion superconductor; $CeCu_2Si_2$ was discovered by Steglich *et al.* in 1979.[4,7,12,13] Heavy-fermions have large electronic specific heat coefficients, $\gamma = C/T$, corresponding to effective masses ($m^* \geq 100\ m_e$) of over several hundred times the mass of the free electron. Another interesting heavy-fermion compounds ($CeMIn_5$; M = Co, Rh, and Ir) have shown superconductivity at low temperatures.[19-22]

In our group, several structure types of ternary layered intermetallic compounds containing rare earths, transition metals, and main group elements have been synthesized by flux growth methods and investigated to correlate structures as they relate with physical properties.[23]

For example, both $CePdGa_6$ and Ce_2PdGa_{12} are ordered antiferromagnetically at 5.5 K and 11 K, respectively and exhibit heavy-fermion behavior with $\gamma \approx 400$ and 140 mJ/molK^2.[24,25] The focus of my research involves the crystal growth, structures, and physical properties of *Ln-T-X* (*Ln* = rare-earth; *T* = Cu, Ag; *X* = Al, Ga) systems to investigate strongly correlated electron phenomena in *f*-electron intermetallics.

1.2 Crystal Growth and Characterization

1.2.1 Metal Flux Growth

Intermetallic compounds are defined as the material containing more than two different metal atoms. As explained above, their importance for scientific area has been increased. However, it is not easy to synthesize intermetallic compounds because their reactions normally accompany with high temperatures due to high melting points of metals. Arc-melting and radio frequency induction heating methods have frequently been used to synthesize intermetallic compounds. Those high temperature methods lead materials scientists to obtain thermodynamically stable phase in the most time and limit the formation of metastable phases.[26] In addition, the fast cooling of the reactants from arc-melting and radio frequency induction heating methods does not provide a suitable environment for crystal growth.

The metal flux growth method has been used as a synthetic route to form intermetallic compounds. Here, the flux is a molten main group metal which serves as a reaction medium. Several main group elements such as aluminum, gallium, indium, tin, antimony, and lead are good candidates as fluxes which should have a relatively low melting point and a large difference between its melting point and boiling point. As a result, the metal flux method allows solid state chemists an opportunity to discover new phases by changing a reaction temperature profile, which is a critical synthetic tool in solid state chemistry.

Although it is not necessary to completely dissolve the constituents of the desired materials, it should be considered for the flux to have reasonable solubilities for the constituents. The binary phase diagrams provide helpful information for solubility between elements and the known stable binary compounds. By considering the binary phase diagrams for the constituent elements, the temperature profile and the reaction ratio are designed. Each element is mixed into an alumina crucible which is covered with quartz wool, and then sealed into evacuated fused silica tubes. After finishing the reaction with the designed temperature profile, the tube is immediately inverted and spun with a centrifuge to remove an excess flux mechanically (i.e. in this case the spin temperature should be higher than the melting point of the metal flux). To remove the remaining flux on the surface of the crystals, a chemical method such as etching is used.

1.2.2 X-ray Diffraction

All structural determinations of the presented intermetallic compounds in this dissertation were performed by using single crystal X-ray diffraction. In general, intensity data are collected on a Bruker Nonius KappaCCD single-crystal diffractometer equipped with Mo K$_\alpha$ radiation (λ = 0.71073 Å) up to θ = 30.0° at room temperature (~ 298 K) by using Nonius SuperGUI software. In the case that the system needs to be considered to have a dynamic disorder or a structural change as a function of temperature, data collection at low temperatures can be executed. Data reduction and integration are performed with the maXus package. Direct methods are used to solve the structure. SHELXL97[27] is used to refine the structural model of the compounds, and data are corrected with extinction coefficients and refined with anisotropic displacement parameters. The other factors such as site occupancy, occupational disorder, and static disorder can be considered to obtain the final structural model. Powder X-ray diffraction (using a Bruker

D-8 X-ray Diffractometer with monochromatized Cu K_α radiation, = 1.540562 Å) is used to determine the phase homogeneity of each sample batch by collecting data on ground single crystals. Data are collected in the range of $2\theta = 20°$ to $80°$ at room temperature. Collected powder X-ray diffraction patterns of the samples are compared to the known powder patterns in the database from the Joint Committee on Powder Diffraction Standards (JCPDS).

1.2.3 Powder Neutron Diffraction

Although X-ray diffraction is a powerful and easily accessible technique for structural determination, the neutron technique is complementary in many situations such as incoherent scattering, atomic disorder, and magnetic scattering. One of the presented crystal systems showed an indication of a statistical disorder from X-ray diffraction experiment. To verify a statistical disorder, a neutron powder diffraction experiment was performed using the BT-1 32 detector neutron powder diffractometer at the NIST Center for Neutron Research (NCNR). A Cu(311) monochromator with a $90°$ take-off angle, $\lambda = 1.5403(2)$ Å, and in-pile collimation of 15' of arc were used. Data were collected over the range of $3°$ to $166°$ 2θ with a step size of $0.05°$ under ambient conditions. Rietveld refinement of the structure was performed using the GSAS software package with the EXPGUI interface.[28,29]

1.2.4 Elemental Analysis

Qualitative and quantitative analysis should be considered as a complementary technique although X-ray diffraction experiments can provide electron density data, allowing us to determine the elemental information. In the case that elements have similar Z values, it is difficult to distinguish between elements from X-ray diffraction data. Here, electron probe microanalysis was performed using a JEOL JSM-5060 scanning electron microscope equipped with an energy dispersive spectrometer to determine the composition of elements. The

accelerating voltage was 15 kV with beam to sample distance of 20 mm. An average of 5-7 scans was performed on each single crystal. ICP-OES experiment was also performed with a Perkin Elmer Optima Model 5300V at Galbraith Laboratories, Inc. to confirm the stoichiometry of the crystal.

1.3 Physical Properties

1.3.1 Magnetism

The magnetic properties of materials have been of basic interest and also brought great practical attention due to the wide range of applications that magnetic materials fit in magnetic recording, in electrical power generation, transmission in communications, and even magnetic imaging in medical purpose. The origin of magnetism results from the electron spins, orbital motions and the magnetic moments of electrons, and the resulting magnetic moments of atoms and ions. Inorganic solids containing unpaired electrons which are mainly transition metals and lanthanides exhibit magnetic effects. Several magnetic effects can be categorized as below. In the case that unpaired electrons are randomly oriented on the different atoms, the material is considered paramagnetic. When electron spins or magnetic moments are aligned parallel, the material shows a spontaneous magnetic moment and is ferromagnetic. The electron spins may be ordered in an anti-parallel manner with zero net magnetic moment, which is called antiferromagnetic behavior. If the electron spins are aligned anti-parallel but with unequal numbers in the two orientations, as a result, the material displays a net magnetic moment and is considered ferrimagnetic.

1.3.1.1 Magnetic Behavior in Materials

When a substance is placed in an external magnetic field (H), the relationship between the magnetic induction or magnetic flux density (B) and an external magnetic field (H) is

expressed using the following equation:[30]

$$B = \mu H \qquad (1.1)$$

The magnetic permeability of the material,

$$\mu = \frac{B}{H}, \qquad (1.2)$$

can be related to both temperature and magnetic field. The magnetic behavior of the material can be written alternatively in terms of its magnetization or magnetic moment per unit volume M induced by the field H, as below:

$$\chi = \frac{M}{H}, \qquad (1.3)$$

where χ is the magnetic susceptibility of the material.

In SI system of units, B, H, and M are related by the following equation:

$$B = \mu_0 (H + M) = (1 + \chi)\mu_0 H = \mu_r\mu_0 H, \qquad (1.4)$$

where H is considered as the internal magnetic field and μ, χ, and μ_r are related by $\mu = (1 + \chi)\mu_0 = \mu_r\mu_0$. Here $\mu_0 = 4\pi \times 10^{-7}$ N/A^2 is the permeability of free space and μ_r is the dimensionless relative permeability of the material. The values of χ are often used to distinguish the type of magnetic behavior of the material. For instance, χ is very small and slightly negative for diamagnetic materials. For paramagnetic materials, small and positive χ is usually observed. Ferromagnetic materials show $\chi \gg 1$ and are strongly attracted to a magnetic field. Antiferromagnetic materials display positive and small but somewhat less χ than for paramagnetic substances.

1.3.1.2 Curie and Curie-Weiss Law

The interaction of applied field and thermal randomization leads to the temperature dependence described the Curie law[30] as below:

$$\chi = \frac{C}{T} \qquad (1.5)$$

Here, C is the Curie constant and T is temperature. Most paramagnetic materials follow this simple Curie law at high temperatures which means that there is no spontaneous interaction between neighboring magnetic moments. They are subject to line up when a magnetic field is applied, but with increasing temperature it is more difficult to align and χ decreases. When spontaneous interaction between magnetic moments exists in ferro- or antiferromagnetic materials at low temperatures, different temperature dependence is developed by the Curie-Weiss law:

$$\chi = \frac{C}{T-\theta} \qquad (1.6)$$

where θ is the Weiss constant. These three types of magnetic behavior are shown in Figure 1.1. Ferromagnetic materials show the saturation of χ and deviate from Curie-Weiss behavior below the ferromagnetic Curie temperature, T_C. Above T_C, χ follows Curie-Weiss law. Antiferromagnetic materials show very small magnetic susceptibility (χ) in the ordered state. χ increases with temperature due to thermally-induced disorder into the antiferromagnetic state and then after a maximum point at Néel temperature (T_N) decreases at higher temperatures, following the Curie-Weiss law. From the linear fit of inverse magnetic susceptibility (χ^{-1}) versus T above the ordering temperature, the Curie constant can be obtained. An experimental effective moment is related to the Curie constant as below:

$$\mu_{\text{eff}}^2 = \frac{3kC}{N\mu_B^2} \qquad (1.7)$$

where μ_{eff} is effective moment, μ_B is Bohr magneton, k is Boltzmann constant, and N is Avogadro's number. Extrapolation of the linear fit of χ^{-1} gives the Weiss temperature (θ). The
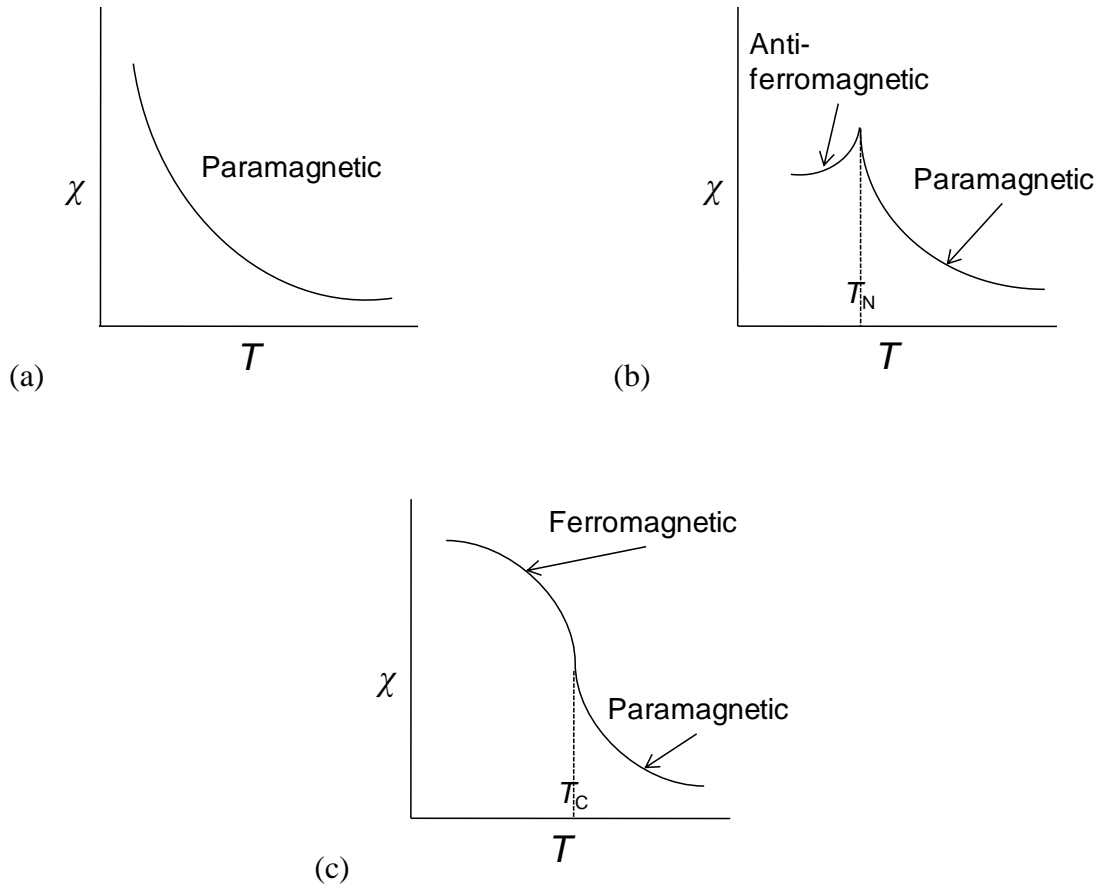
Figure 1.1 Variation of magnetic susceptibility with temperature for (a) a paramagnetic material, (b) an antiferromagnetic material, and (c) a ferromagnetic material.

linear fit of the paramagnetic material normally extrapolates to 0 K. The sign of θ is indicative of the alignment of the magnetic moments. The positive and negative sign of θ correspond to ferromagnetic and antiferromagnetic ordering, respectively. An experimental effective moment can be compared to a calculated effective moment which is given by this equation,

$$\mu_{\text{eff}} = g\sqrt{J(J+1)},$$ (1.8)

where g is the gyromagnetic ratio:[31,32]

$$g = 1 + \frac{S(S+1) - L(L+1)}{2J(J+1)}$$ (1.9)

8

Here, S is the total spin momentum, L is the total orbital momentum, and J is the total angular momentum. As stated above, the magnetic property of the material arises from the electron spins, orbital motions and the magnetic moments of electrons, and the resulting magnetic moments of atoms and ions. Although the electron spins are the most important factor to determine an effective moment, a full treatment with orbital moments and spin-orbital coupling should be considered to obtain the accurate moments for lanthanide systems.

1.3.2 Resistivity and Magentoresistance

The electrical resistivity, ρ,[30] is defined as the reciprocal of the conductivity,

$$\rho = \frac{1}{\sigma} = \frac{m}{ne^2\tau},$$ (1.10)

where σ is the electrical conductivity, m is the mass, n is the number of electrons, e is the electron charge, and τ is the time. Collisions between the electrons and lattice phonon are mainly responsible for the electrical resistivity of most metals at room temperature. However, at liquid helium temperature the electrical resistivity is governed by collisions with impurity atoms and mechanical imperfections in the lattice. The net resistivity is described as below:

$$\rho = \rho_L + \rho_i,$$ (1.11)

where ρ_L is the resistivity caused by the thermal phonons, and ρ_i is the resistivity due to scattering of the electron waves by static lattice defects. The resistivity ratio of the sample defining as the ratio of its resistivity at room temperature to its residual resistivity, $\rho_i(0)$, is usually used as an indicator of sample purity.

Magnetoresistance (MR)[30] is a change in resistance by applied magnetic fields and expressed as below:

$$\text{MR} (\%) = \frac{\rho_H - \rho_0}{\rho_0} \times 100,$$ (1.12)

where ρ_H is the electrical resistance at an external magnetic field (H), and ρ_0 is the electrical resistance at zero field.

1.3.3 Heat Capacity

1.3.3.1 Heat Capacity of Electron

A heat capacity of $3/2k_B$ for a free particle, where k_B is the Boltzmann constant, is given by classical statistical mechanics. If there are free N electrons, the electronic contribution to the heat capacity should be $3/2Nk_B$.[30] However, the observed electronic contribution at room temperature is usually less than the theoretical value because only a fraction of the order of T/T_F can be excited thermally at temperature T, where T_F is called the Fermi temperature. When the sample is heated from absolute zero, the order of T/T_F electrons gains energy, k_BT as expected classically. Therefore, the total electronic thermal kinetic energy U can be described as

$$U \approx (NT/T_F)k_BT. \tag{1.13}$$

The electronic heat capacity is obtained by

$$C_{el} = \partial U/\partial T \approx Nk_B(T/T_F). \tag{1.14}$$

The electronic heat capacity at low temperatures $k_BT \ll \varepsilon_F$ can be expressed quantitatively by using the Fermi-Dirac function, $f(\varepsilon)$ as below:

$$C_{el} = \frac{dU}{dT} = \int_0^\infty d\varepsilon(\varepsilon - \varepsilon_F)\frac{df}{dT}D(\varepsilon), \tag{1.15}$$

where $D(\varepsilon)$ is the number of orbitals per unit energy range. This equation can be integrated with an approximation as below:

$$C_{el} = \frac{1}{3}\pi^2 D(\varepsilon_F)k_B^2 T, \tag{1.16}$$

where $D(\varepsilon_F) = 3N/2\varepsilon_F = 3N/2k_BT_F$. Thus, this equation becomes for a free electron gas with $k_BT_F \equiv \varepsilon_F$ as below:

$$C_{el} = \frac{1}{2}\pi^2 N k_B T/T_F.$$
(1.17)

1.3.3.2 Heat Capacity of Metals and Heavy-Fermion Behavior

The total heat capacity of metals can be described as the sum of electron and phonon contributions:

$$C_P = \gamma T + AT^3,$$
(1.18)

where γ is the Sommerfeld coefficient of electronic specific heat and A is the phonon contribution to the total specific heat. The electronic component is dominant at low temperatures. Therefore, this equation can be rearranged as $C/T = \gamma + AT^2$ and plotted as C/T versus T^2. The relation between a ratio of thermal effective mass m^* to the electron mass m and the ratio of the observed to the free electron values of the electronic heat capacity can be described as below:

$$\frac{m^*}{m} \equiv \frac{\gamma(\text{observed})}{\gamma(\text{free})}.$$
(1.19)

Heavy-fermions have large electronic specific heat coefficients γ corresponding to effective masses ($m^* \geq 100\ m_e$) of over several hundred times the mass of the free electron due to the weak overlap of wavefunctions of f-electrons on neighboring ions.

1.4 References

(1)   Fisk, Z.; Sarrao, J. L.; Smith, J. L.; Thompson, J. D. *Proc. Natl. Acad. Sci.USA* **1995**, *92*, 6663-6667.

(2)   Lohneysen, H. *Hyperfine Interact.* **1997**, *104*, 127-139.

(3)   De Chatel, P. F. *Philos. Mag. B* **2001**, *81*, 1389-1395.

(4)   Sato, N. K. *J. Phys.: Condens. Matter* **2003**, *15*, S1937-S1943.

(5)   Maple, M. B. *J. Phys. Soc. Jpn.* **2005**, *74*, 222-238.

(6)   Kanamori, J. *J. Alloys Compd.* **2006**, *408-412*, 2-8.

(7)   Steglich, F.; Aarts, J.; Bredl, C. D.; Lieke, W.; Meschede, D.; Franz, W.; Schaefer, H. *Phys. Rev. Lett.* **1979**, *43*, 1892-1896.

(8)   Bickers, N. E.; Cox, D. L.; Wilkins, J. W. *Phys. Rev. B: Condens. Matter* **1987**, *36*, 2036.

(9)   Kouwenhoven, L.; Glazman, L. *Phys. World* **2001**, *14*, 33-38.

(10)   Coleman, P.; Pepin, C. *Acta Phys. Pol., B* **2003**, *34*, 691-705.

(11)   Si, Q.; Zhu, J.-X.; Grempel, D. R. *J. Phys.: Condens. Matter* **2005**, *17*, R1025-R1040.

(12)   Thalmeier, P.; Zwicknagl, G.; Stockert, O.; Sparn, G.; Steglich, F. *Front. Supercond. Mater.* **2005**, 109-182.

(13)   Flouquet, J.; Knebel, G.; Braithwaite, D.; Aoki, D.; Brison, J.-P.; Hardy, F.; Huxley, A.; Raymond, S.; Salce, B.; Sheikin, I. *C. R. Phys.* **2006**, *7*, 22-34.

(14)   Fulde, P.; Thalmeier, P.; Zwicknagl, G. *Los Alamos National Laboratory, Preprint Archive, Condensed Matter* **2006**, 1-207, arXiv:cond-mat/0607165.

(15)   Kondo, J. *Progr. Theoret. Phys. (Kyoto)* **1964**, *32*, 37-69.

(16)   Ruderman, M. A.; Kittel, C. *Phys. Rev.* **1954**, *96*, 99-102.

(17)   Kasuya, T. *Prog. Theor. Phys.* **1956**, *16*, 45-57.

(18)   Yosida, K. *Phys. Rev.* **1957**, *106*, 893.

(19)   Hegger, H.; Petrovic, C.; Moshopoulou, E. G.; Hundley, M. F.; Sarrao, J. L.; Fisk, Z.; Thompson, J. D. *Phys. Rev. Lett.* **2000**, *84*, 4986-4989.

(20)   Petrovic, C.; Movshovich, R.; Jaime, M.; Pagliuso, P. G.; Hundley, M. F.; Sarrao, J. L.; Fisk, Z.; Thompson, J. D. *Europhys. Lett.* **2001**, *53*, 354-359.

(21)   Petrovic, C.; Pagliuso, P. G.; Hundley, M. F.; Movshovich, R.; Sarrao, J. L.; Thompson, J. D.; Fisk, Z.; Monthoux, P. *J. Phys.: Condens. Matter* **2001**, *13*, L337-L342.

(22)   Moshopoulou, E. G.; Sarrao, J. L.; Pagliuso, P. G.; Moreno, N. O.; Thompson, J. D.; Fisk, Z.; Ibberson, R. M. *Appl. Phys. A* **2002**, *74*, S895-S897.

(23)   Thomas, E. L.; Millican, J. N.; Okudzeto, E. K.; Chan, J. Y. *Comments Inorg. Chem.* **2006**, *27*, 1-39.

(24)   Macaluso, R. T.; Nakatsuji, S.; Lee, H.; Fisk, Z.; Moldovan, M.; Young, D. P.; Chan, J. Y. *J. Solid State Chem.* **2003**, *174*, 296-301.

(25)   Macaluso, R. T.; Millican, J. N.; Nakatsuji, S.; Lee, H.-O.; Carter, B.; Moreno, N. O.; Fisk, Z.; Chan, J. Y. *J. Solid State Chem.* **2005**, *178*, 3547-3553.

(26)   Kanatzidis, M. G.; Pöttgen, R.; Jeitschko, W. *Angew. Chem. Int. Ed.* **2005**, 44, 6996-7023

(27)   Sheldrick, G. M.; University of Gottingen: Germany, **1997**.

(28)   Larson, A. C.; Von Dreele, R. B. *GSAS-Generalized Structure Analysis System*: LANSCE, MS-H805, Los Alamos National Laboratory, Los Alamos, NM 87545 USA, **2000**.

(29)   Toby, B. H. *J. Appl. Crystallogr.* **2001**, *34*, 210-213.

(30)   Kittel, C. Introduction to Solid State Physics; 7th ed.; John Wiley & Sons, Inc.: New York, 1996.

(31)   West, A. R. Basic Solid State Chemistry; 2nd ed.; John Wiley & Sons, Ltd.: New York, 1999.

(32)   Smart, L. E.; Moore, E. A. Solid State Chemistry: An Introduction; 3rd ed.; Taylor & Francis Group: Boca Raton, 2005.

CHAPTER 2. CRYSTAL GROWTH, STRUCTURE, AND PHYSICAL PROPERTIES
OF Ln_2MGa_{12} (Ln = La, Ce; M = Ni, Ga)[*]

2.1 Introduction

Ce-containing heavy-fermion ternary compounds, which show large electronic masses ($m^* \approx$ 100-1000 m_e), have been of interest because of their exotic physical properties, such as magnetic ordering and superconductivity.[1-4] In these systems there is a competition between the tendency towards magnetic order of f-electrons via hybridization pathways with the conduction electrons (RKKY mechanism) and the tendency towards the screening of magnetic moments (Kondo effect) producing large effective electron masses. Recently the structure and properties of Ce_2PdGa_{12} and $CePdGa_6$ have been reported.[5] $CePdGa_6$ consists of alternating layers of $CeGa_{8/4}$ and $PdGa_{8/2}$ in a 1:1 ratio, and in contrast Ce_2PdGa_{12} consists of Ce bilayers including Ga-only segments and single layers of $CuGa_{8/2}$ along the crystallographic c-axis.[5] In the case of Ce_2PdGa_{12}, the bilayer structure seems to favor magnetic ordering mediated by RKKY, in contrast to the single Ce layered compound, which tends to favor Kondo behavior with enhanced quasiparticle mass. Also, $CeCoIn_5$ has been reported as a heavy-fermion compound (Sommerfeld coefficient of specific heat, $\gamma \approx$ 500 mJmol^{-1}K^{-2}), which also shows a superconducting transition temperature (T_c = 2.3 K) at ambient pressure.[6] The superconductivity in this family of compounds Ce_nMIn_{3n+2} (n = 1) is unusual, in that it tends to coexist with static magnetism. Also, the related compounds, Ce_2MIn_8 (M = Co, Rh, and Ir), exhibit heavy-fermion behavior with $\gamma \approx$ 500, 400, and 700 mJmol^{-1}K^{-2} for the Co, Rh, and Ir containing compounds, respectively.[7-9] Although various experiments have been performed on many systems in this interesting class of compounds, a comprehensive understanding of heavy-fermion properties at

low temperature is still lacking.

We have synthesized Ln_2MGa_{12} (Ln = La, Ce; M = Ni, Cu), which are isomorphous to Ce_2PdGa_{12}.[5] Our major interest in investigating these materials lies with the fact that Ce-based heavy Fermion superconductors at ambient pressure are very rare. The original heavy Fermion superconductor, $CeCu_2Si_2$, was the only example until very recently.[10] Searching chemical phase space allows the opportunity to discover other intermetallic Ce compounds that share similar physical properties to $CeCu_2Si_2$ and Ce_nMIn_{3n+2}. If this new class of compounds is found to superconduct, at ambient pressure or otherwise, the presence of strong magnetic interactions between the $4f$ levels and itinerant electrons inherent in these systems, may give rise to unconventional superconductivity, where the pairing mechanism is mediated by something other than phonons.

These structures can be viewed as a three-dimensional network of [MGa] (M = Cu, Ni) with Ce atoms occupying cavities made of Ga atoms. In this paper, we compare the structures of Ce_2MGa_{12} (M = Ni, Cu) and Ce_2PdGa_{12} and investigate the role of the transition metal environments as they relate to the physical properties of these compounds. A partial contribution to the total electron DOS, which refers to the total number of available states for occupation at each energy level, at the Fermi surface from the transition metal has been suggested by band structure calculations of Sm_2NiGa_{12}.[11] By substituting Cu for Ni, we would expect to change the electronic properties. The properties of the Ce_nMIn_{3n+2} family of compounds are intimately tied to the choice of the transition metal. In previous studies, a change in γ has been observed to occur when Pd is substituted by Cu or Ni. For example, the heavy-fermion $CePd_2Si_2$[12,13] has a $\gamma \approx 250$ mJmol^{-1}K^{-2} while the isostructural Cu analogue[10,14] shows enhanced electron mass with $\gamma \approx 1100$ mJmol^{-1}K^{-2}. Several other copper-containing compounds such as $CeCu_4Al$, $CeCu_3Al_2$, and

CeCu$_4$Ga also show heavy-fermion behavior with $\gamma \approx 1000$ mJmol^{-1}K^{-2}, 490 mJmol^{-1}K^{-2}, and 3000 mJmol^{-1}K^{-2}, respectively.[15-17]

2.2 Experimental

2.2.1 Synthesis

Single crystals of Ln_2MGa$_{12}$ (Ln = La, Ce; M = Ni, Cu) were prepared by gallium flux growth method. La or Ce ingot (3N, Ames Laboratory), Cu or Ni powder (5N, Alfa Aesar), and Ga (6N, Alfa Aesar) were placed into alumina crucibles in a 1.5:1:15 ratio. The crucible containing the starting materials was then sealed into an evacuated fused silica tube and heated up to 1423 K at a rate of 170 K/h and allowed to dwell for 7 h at that temperature. After fast cooling at a rate of 150 K/h to 773 K, the fused silica tube was allowed to cool slowly down to 673 K at a rate of 8 K/h and immediately inverted and centrifuged. Silver-colored plate-like aggregates of crystals were found and mechanically separated from gallium flux. Typical crystal size ranged from 1 × 2 × 2 to 1 × 2 × 5 mm^3. The crystals were stable in air. Single crystals from several growths of La$_2$CuGa$_{12}$ were ground for powder neutron experiment.

2.2.2 Powder and Single-Crystal X-ray Diffraction

Silver-colored fragments ($\approx$ 0.01 mm × 0.01 mm × 0.01 mm to 0.03 mm × 0.03 mm × 0.05 mm) of La$_2$NiGa$_{12}$ and Ce$_2M$Ga$_{12}$ (M = Ni, Cu) were attached on a thin glass fiber using a two-component adhesive and mounted onto the goniometer of a Nonius KappaCCD diffractometer equipped with a MoK$_\alpha$ radiation (λ = 0.71073 Å) X-ray tube. Single crystal data were collected at 298 K for all samples, and additional data were collected at 90 K to examine disorder in Ce$_2$CuGa$_{12}$. Direct methods were used to solve the structure. SHELXL97 was used to refine the structural model of the La$_2$NiGa$_{12}$ and Ce$_2M$Ga$_{12}$ (M = Ni, Cu) compounds, and data were corrected with extinction coefficients and refined with anisotropic displacement parameters.

The obtained structural model was compared to the crystallographic data from Sm_2NiGa_{12}. Crystallographic parameters for La_2NiGa_{12} and Ce_2MGa_{12} (M = Ni, Cu) are provided in Table 2.1. Atomic positions and displacement parameters for the compounds are given in Table 2.2, and selected interatomic distances are also provided in Table 2.3. Powder X-ray diffraction data were collected on several ground single crystals of each compound to examine the phase purity. The diffraction patterns show peaks which are consistent with their calculated powder patterns. Although the single crystals of La_2CuGa_{12} were not of sufficient quality and the structure could not be confirmed using single crystal X-ray diffraction experiments, powder X-ray diffraction techniques were used to index the pattern of La_2CuGa_{12} as isostructural to the analogous 2-1-12 phases. Neutron powder diffraction experiments were ultimately used to solve the structure of La_2CuGa_{12}. Additional crystallographic parameters, atomic positions, and interatomic distances for La_2CuGa_{12} are also provided in Table 2.1-2.3.

2.2.3 Neutron Powder Diffraction (NPD)

A 3.71 g powder sample of La_2CuGa_{12} was loaded in a vanadium container of length 50 mm and diameter 6.0 mm. Neutron powder diffraction data were collected using the BT-1 32 detector neutron powder diffractometer at the NIST Center for Neutron Research (NCNR). A Cu(311) monochromator with a 90° take-off angle, λ = 1.5403(2) Å, and in-pile collimation of 15' of arc were used. Data were collected over the range of 3° to 166° 2θ with a step size of 0.05° under ambient conditions. Rietveld refinement of the structure of La_2CuGa_{12} was performed using the GSAS software package with the EXPGUI interface.[18,19]

2.2.4 Physical Property Measurements

Magnetic data were obtained using a Quantum Design Physical Property Measurement System (PPMS). The temperature-dependent susceptibility data were obtained under zero-field

Table 2.1 Crystallographic Data for Ln_2MGa_{12} (Ln = La, Ce; M = Ni, Cu)

	La$_2$NiGa$_{12}$	Ce$_2$NiGa$_{12}$	La$_2$CuGa$_{12}$	Ce$_2$CuGa$_{12}$ (298 K)	Ce$_2$CuGa$_{12}$ (90 K)
Crystal data					
Formula	La$_2$NiGa$_{12}$	Ce$_2$NiGa$_{12}$	La$_2$CuGa$_{12}$	Ce$_2$CuGa$_{12}$ (298 K)	Ce$_2$CuGa$_{12}$ (90 K)
Crystal system	Tetragonal	Tetragonal	Tetragonal	Tetragonal	Tetragonal
Space group	*P*4/*nbm*	*P*4/*nbm*	*P*4/*nbm*	*P*4/*nbm*	*P*4/*nbm*
a (Å)	6.073(3)	6.036(2)	6.1760(1)	6.108(3)	6.090(2)
c (Å)	15.547(5)	15.506(8)	15.3660(3)	15.375(4)	15.348(7)
V (Å^3)	573.4(4)	564.9(4)	586.11(3)	573.6(4)	569.2(4)
Z	2	2	2	2	2
Crystal dimension (mm^3)	0.03×0.03×0.05	0.05×0.05×0.08	-	0.05×0.05×0.08	0.03×0.05×0.05
2θ range (°)	5.24-60.06	9.56-60.02	3.0- 167.8	7.96-59.96	7.96-60.14
μ (mm^{-1})	36.474	37.516	-	37.161	37.447
Data collection					
Measured reflections	1449	1120	-	1455	1259
Independent reflections	480	456	-	481	476
Reflections with $I>2\sigma(I)$	417	375	-	423	375
R_{int}	0.0310	0.0307	0.0310	0.0504	0.0413
h	-8→8	-8→8	0→8	-8→8	-8→8
k	-6→6	-6→6	0→5	-6→6	-5→6
l	-20→21	-21→11	0→19	-21→20	-16→21
Refinement					
Reflections	480	456	3296	481	476
Parameters	26	26	52	26	26
[a]$R_1[F^2>2\sigma(F^2)]$	0.0272	0.0298	0.0402	0.0558	0.0433
[b]$wR_2(F^2)$	0.0632	0.0627	0.0657	0.1444	0.1045
$\Delta\rho_{max}$ (eÅ^{-3})	2.164	2.485	-	6.689	5.635
$\Delta\rho_{min}$ (eÅ^{-3})	-1.546	-1.396	-	-9.427	-3.352

[a]$R_1 = \sum ||F_o| - |F_c|| / \sum |F_o|$

[b]$wR_2 = [\sum [w(F_o^2 - F_c^2)] / \sum [w(F_o^2)^2]]^{1/2}$

$w = 1/[\sigma^2(F_o^2) + (0.0252\,P)^2 + 4.0550\,P]$

$w = 1/[\sigma^2(F_o^2) + (0.0222\,P)^2 + 2.0096\,P]$,

$w = 1/[\sigma^2(F_o^2) + (0.0775\,P)^2 + 11.6928\,P]$,

$w = 1/[\sigma^2(F_o^2) + (0.0518\,P)^2 + 6.8961\,P]$,

for La$_2$NiGa$_{12}$, Ce$_2$NiGa$_{12}$, Ce$_2$CuGa$_{12}$ (298 K), and Ce$_2$CuGa$_{12}$ (90 K), respectively

Table 2.2 Atomic Positions and Thermal Parameters for Ln_2MGa_{12} (Ln = La, Ce; M = Ni, Cu)

Atom	Wyckoff position	x	y	z	Occ.[a]	U_{eq} (Å^2)[b]
La$_2$NiGa$_{12}$						
La	4h	3/4	1/4	0.24453(3)	1	0.00769(19)
Ni	2c	3/4	1/4	0	1	0.0081(4)
Ga1	4g	3/4	3/4	0.18023(6)	1	0.0091(3)
Ga2	4g	3/4	3/4	0.33936(6)	1	0.0117(3)
Ga3	8m	0.50037(9)	0.00037(9)	-0.08283(4)	1	0.0095(2)
Ga4	8m	0.56689(12)	0.06689(12)	0.42791(5)	1	0.0230(3)
Ce$_2$NiGa$_{12}$						
Ce	4h	3/4	1/4	0.24439(4)	1	0.00734(19)
Ni	2c	3/4	1/4	0	1	0.0078(4)
Ga1	4g	3/4	3/4	0.18140(8)	1	0.0086(3)
Ga2	4g	3/4	3/4	0.33954(9)	1	0.0118(3)
Ga3	8m	0.50023(9)	0.00023(9)	-0.08340(5)	1	0.0092(2)
Ga4	8m	0.57024(12)	0.07024(12)	0.42816(7)	1	0.0211(3)
La$_2$CuGa$_{12}$[c]						
La	4h	3/4	1/4	0.2463(2)	1	0.0090(8)
Cu	2c	3/4	1/4	0	1	0.0120(13)
Ga1	4g	3/4	3/4	0.1764(2)	1	0.0136(13)
Ga2	4g	3/4	3/4	0.3358(2)	1	0.0153(11)
Ga3	8m	0.5011(7)	0.0011(7)	-0.0845(2)	1	0.0151(7)
Ga4a	8m	0.567(4)	0.067(4)	0.4276(11)	0.42(4)	0.065(13)
Ga4b	8m	0.4471(21)	-0.0529(21)	0.4249(6)	0.60(4)	0.048(6)
Ce$_2$CuGa$_{12}$ (298 K)						
Ce	4h	3/4	1/4	0.24637(5)	1	0.0051(4)
Cu	2c	3/4	1/4	0	1	0.0101(7)
Ga1	4g	3/4	3/4	0.17753(12)	1	0.0075(5)
Ga2	4g	3/4	3/4	0.33633(12)	1	0.0104(5)
Ga3	8m	0.50036(14)	0.00036(14)	-0.08508(7)	1	0.0091(4)
Ga4	8m	0.5609(3)	0.0609(3)	0.42611(9)	1	0.0295(7)
Ce$_2$CuGa$_{12}$ (90 K)						
Ce	4h	3/4	1/4	0.24622(5)	1	0.0019(3)
Cu	2c	3/4	1/4	0	1	0.0035(6)
Ga1	4g	3/4	3/4	0.17778(11)	1	0.0032(4)
Ga2	4g	3/4	3/4	0.33677(11)	1	0.0042(4)
Ga3	8m	0.50017(13)	0.00017(13)	-0.08519(8)	1	0.0043(3)
Ga4	8m	0.56536(18)	0.06536(18)	0.42652(9)	1	0.0145(4)

[a] Occupancy of atoms

[b] U_{eq} is defined as one-third of the trace of the orthogonalized U_{ij} tensor.

[c] Thermal parameters for La$_2$CuGa$_{12}$ are corresponding to U_{11}.

Table 2.3 Selected Interatomic Distances (Å) for $Ln_2M\text{Ga}_{12}$ (Ln = La, Ce; M = Ni, Cu)

La$_2$NiGa$_{12}$		Ce$_2$NiGa$_{12}$	La$_2$CuGa$_{12}$		Ce$_2$CuGa$_{12}$ (at 298 K)		Ce$_2$CuGa$_{12}$ (at 90 K)
	La layer	Ce layer		La layer		Ce layer	Ce layer
Ln-Ga1 (×4)	3.1968(15)	3.1721(10)	La-Ga1 (×4)	3.270(1)	Ce-Ga1 (×4)	3.2321(16)	3.2211(12)
Ln-Ga2 (×4)	3.3755(14)	3.3593(11)	La-Ga2 (×4)	3.3805(17)	Ce-Ga4 (×4)	3.3526(16)	3.3471(13)
Ln-Ga4 (×2)	3.2560(13)	3.2363(17)	La-Ga4a (×2)	3.210(18)	Ce-Ga4 (×2)	3.2101(19)	3.1917(19)
Ln-Ga3 (×2)	3.3040(12)	3.2830(14)	La-Ga4b (×2)	3.241(14)	Ce-Ga3 (×2)	3.2863(16)	3.2768(17)
Ln-Ga3 (×2)	3.3081(12)	3.2855(14)	La-Ga3 (×2)	3.315(5)	Ce-Ga3 (×2)	3.2903(16)	3.2787(17)
			La-Ga3 (×2)	3.302(5)			
	NiGa$_{8/2}$ segment	NiGa$_{8/2}$ segment			CuGa$_{8/2}$ segment	CuGa$_{8/2}$ segment	CuGa$_{8/2}$ segment
Ga1-Ga3 (×4)	2.6274(11)	2.6198(11)	Ga1-Ga3 (×4)	2.600(3)	Ga1-Ga3 (×4)	2.5854(14)	2.5798(13)
Ni-Ga3 (×4)	2.5010(12)	2.4936(10)	Cu-Ga3 (×4)	2.532(5)	Cu-Ga3 (×4)	2.5221(15)	2.5178(13)
Ni-Ga3 (×4)	2.5064(12)	2.4969(10)	Cu-Ga3 (×4)	2.549(6)	Cu-Ga3 (×4)	2.5274(15)	2.5203(13)
	Ga-only Segment	Ga-only segment			Ga-only segment	Ga-only segment	Ga-only segment
Ga2-Ga4 (×4)	2.6144(12)	2.6080(12)	Ga2-Ga4a (×4)	2.665(14)	Ga2-Ga4 (×4)	2.6165(17)	2.6174(14)
Ga4-Ga4 (×1)	2.5189(17)	2.530(2)	Ga2-Ga4b (×4)	2.619(7)	Ga4-Ga4 (×1)	2.504(3)	2.521(3)
			Ga4a-Ga4a (×1)	2.517(34)			
			Ga4b-Ga4b (×1)	2.485(21)			

cooled (ZFC) conditions from 2 K to 300 K under an applied field (μ_0H) of 0.1 T, and then measured upon heating to obtain field-cooled (FC) data after cooling to 2 K under field. Field-dependent magnetization data were measured at 3 K with field (μ_0H) up to 9 T. The electrical resistivity and magnetoresistance (MR) were measured by the standard four-probe AC technique. Measurements of the heat capacity were performed using a Quantum Design Physical Property Measurement System at temperatures from 0.35 K to 70 K.

2.3 Results and Discussion

2.3.1 Structure

The structure of Ce$_2$CuGa$_{12}$ is shown in Figure 2.1. Ce$_2M$Ga$_{12}$ (M = Ni, Cu), which are isostructural to Sm$_2$NiGa$_{12}$[11] and Ce$_2$PdGa$_{12}$,[5] crystallize in the tetragonal $P4/nbm$ space group

(No. 125, origin choice 2) with the Ce, M (M = Ni, Cu), Ga1, Ga2, Ga3 and Ga4 occupying the $4h$, $2c$, $4g$, $4g$, $8m$, and $8m$ Wyckoff sites, respectively. This structure can be described as a repeating network of [MGa] (M = Ni, Cu) units with Ce atoms occupying cavities made of Ga atoms, along the crystallographic c-axis. As shown in Table 2.3, in Ce_2MGa_{12} (M = Ni, Cu), the local Ce environment consists of Ce atoms, which are coordinated to 14 Ga atoms: 4 Ga1, 4 Ga2, 4 Ga3, and 2 Ga4. The Ce-centered Ga rectangular prism is capped by two Ga4 atoms and four Ga3 atoms. The Ce-Ga distances, which range from 3.1721(10) Å to 3.2903(16) Å, are in good agreement with typical Ce-Ga interatomic distances in other binary and ternary compounds such as $CeGa_2$, $CeGa_6$, Ce_3Ga, Ce_3Ga_2, Ce_5Ga_3, $CeNiGa_3$, $CeCu_2Ga_2$, and Ce_2PdGa_{12}.[5,20-25] The Ce-Ga4($\times$2) distances of 3.2101(19) Å in Ce_2CuGa_{12} are slightly shorter than the distances of 3.2363(17) Å found in Ce_2NiGa_{12}. However, the Ce-Ga1($\times$4) and Ce-Ga3($\times$2) distances of 3.2321(16) Å and 3.2903(16) Å, respectively, in Ce_2CuGa_{12} are slightly longer than Ce-Ga1($\times$4) and Ce-Ga3($\times$2) distances of 3.1721(10) Å and 3.2855(14) Å, respectively, in the Ni analogue.

The [MGa] (M = Ni, Cu) subunit is composed of edge sharing MGa$_{8/2}$ (M = Ni, Cu) rectangular prisms and Ga-only segments. In the rectangular prisms of Ce_2CuGa_{12}, Cu atoms are connected to four Ga3 atoms with interatomic distances of 2.522(2) Å and four additional Ga3 atoms by 2.527(2) Å, which are slightly longer than the Ni-Ga distances of 2.494(1) Å and 2.497(1) Å in Ce_2NiGa_{12}. These distances are also in good agreement with typical of M-Ga (M = Ni, Cu) bonds in other binary and ternary compounds such as Ni_2Ga, Ni_3Ga, $CuGa_2$, Cu_9Ga_4, $CeNiGa_3$, Ce_2NiGa_{10}, and $CeCu_2Ga_2$.[24-29] The Ga1-Ga3 interatomic distance of 2.585(1) Å found in the $CuGa_{8/2}$ rectangular prisms have shorter contacts than the Ga1-Ga3 distance of 2.620(1) Å in the $NiGa_{8/2}$ rectangular prisms of Ce_2NiGa_{12} along the c-axis.
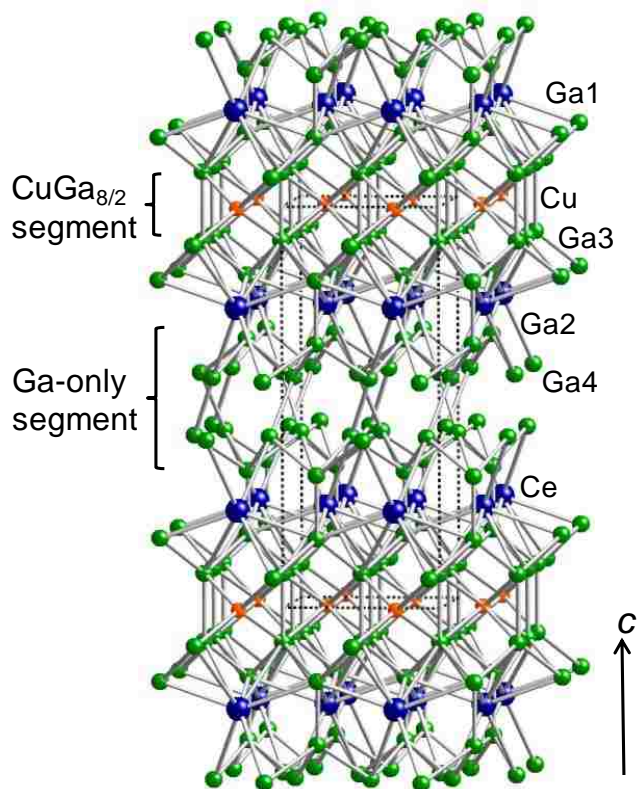
Figure 2.1 The crystal structure of Ce_2CuGa_{12} is shown along the c-axis, where the Ce atoms are represented with big blue spheres; the Cu atoms are denoted as orange spheres; and the Ga atoms are denoted with green spheres. Dashed lines are used to show the unit cell.

The Ga-only segment of the [MGa] (M = Ni, Cu) subunit has two different Ga layers which consist of Ga2 and Ga4 atoms. Within the Ga2 layer for both compounds, Ga-Ga interatomic distances along the ab-plane range from 4.268 to 6.108 Å, which are too far to be considered bonding when compared with the covalent radii of 2.50 Å observed for Ga-Ga bonds. The Ga4-Ga4 interatomic distances of 3.135 Å and 3.143 Å for Ce_2NiGa_{12} and Ce_2CuGa_{12}, respectively, along the ab-plane are also far from typical bond lengths of Ga-Ga and the sum of Ga covalent radii (2.50 Å).[30] However, the Ga4-Ga4 interatomic distances along the c-axis are 2.530(2) Å and 2.504(3) Å for Ce_2NiGa_{12} and Ce_2CuGa_{12}, respectively, which are very close to the sum of Ga covalent radii (2.50 Å).[30] In addition, Ga4 atoms are connected by distances of

2.608(1) Å (Ce_2NiGa_{12}) and 2.617(2) Å (Ce_2CuGa_{12}) with Ga2 atoms along the *c*-axis, which are also in good agreement with the typical interatomic distances in Ga containing binaries such as $CeGa_2$, $CeGa_6$.[20]

From our observation of the difference Fourier syntheses for La_2NiGa_{12} and Ce_2MGa_{12} (*M* = Ni, Cu), another 8*m* Wyckoff site, which is close to the Ga4 position, has been identified. In addition, single crystal X-ray data show an anomalous behavior of the displacement parameters for the Ga4 position, which has its ellipsoid elongated in the *ab*-direction. The former and latter observations may be indicative of statistical and dynamic disorder in the structures, respectively. To examine whether dynamic disorder was present in the structure of Ce_2CuGa_{12}, we collected single crystal X-ray data for Ce_2CuGa_{12} at 90 K as shown in Tables 2.1-2.3. However, the Ga4 atom still shows a large displacement parameter at T = 90 K, implying that a dynamic disorder does not play an important role in this structure. After consideration of that result, a statistical disorder for the Ga4 position was carefully checked. The refinement of partially occupied atoms in two sites, however, did not greatly affect the displacement parameter for Ga4 position nor the other statistical values, such as *R* factor. Therefore, although there might be disorder in the Ln_2MGa_{12} (*Ln* = La, Ce; *M* = Ni, Cu) compounds, we were not able to model the disorder satisfactorily using single crystal X-ray diffraction experiments.

2.3.2 Neutron Powder Diffraction

The structure of La_2CuGa_{12} was refined using neutron powder diffraction techniques. The NPD fit for La_2CuGa_{12} is shown in Figure 2.2. The background was fit using a 13-term shifted Chebychev polynomial. The lattice parameters, zero point, and scale factor were also refined. The peak profile was modeled using Gaussian and Lorentzian terms. The structure of Ce_2CuGa_{12} was used as an initial structural model and reasonable isotropic atomic displacement
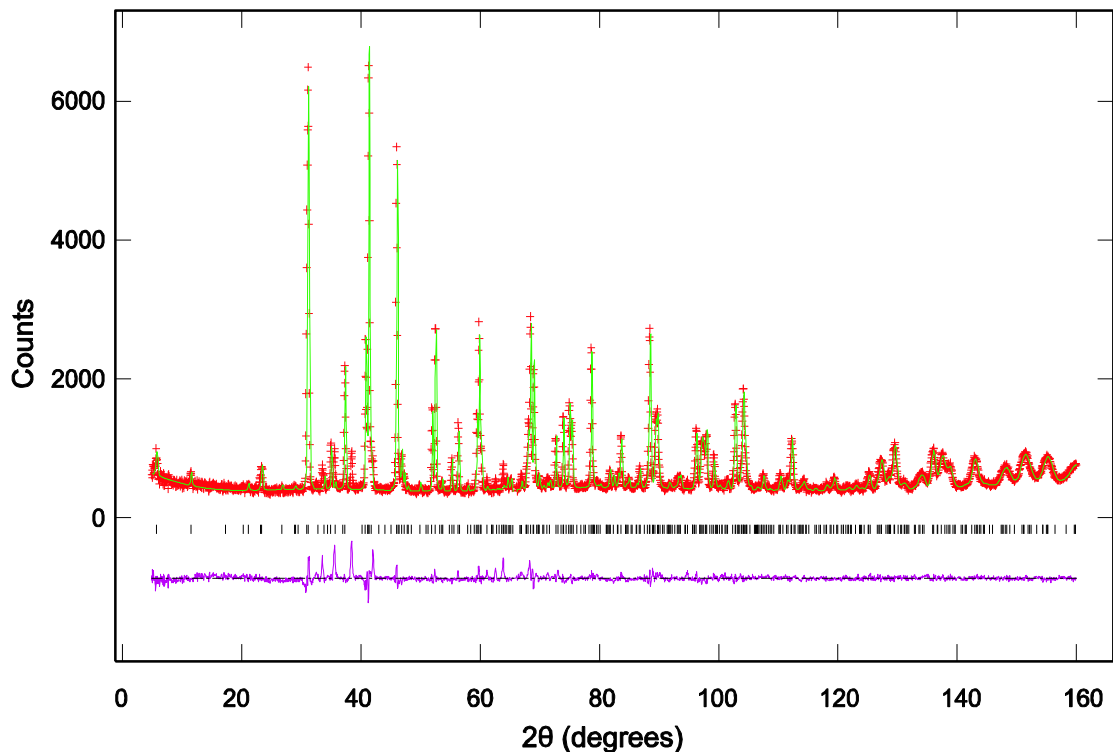
Figure 2.2 The Neutron Powder diffraction data for La_2CuGa_{12} is shown with red crosses. Rietveld refinement fits and the difference curve are shown in green and magenta, respectively. Calculated reflections are marked with black tick marks.

parameters were constrained for the initial least squares cycle. However, upon refinement elongation of the atomic displacement ellipsoid for the Ga4 atom (8*m* Wyckoff site) was observed. The model was refined for statistical disorder, and an additional Ga atom, which is referred to as Ga4b, was added to the structural model on the 8*m* site. The original Ga4 atom, which exists in the parent and analogous phases, has been assigned the label Ga4a for clarity in the La_2CuGa_{12} phase. The Ga4a and Ga4b atoms were observed to have partial occupancies of 0.42(4) and 0.60(4), respectively, which confirms the stoichiometry of La_2CuGa_{12}. The occupancies of the La, Cu, Ga1, Ga2, and Ga3 atoms were allowed to refine freely, but the occupancies remained close to unity, suggesting full occupancy on these particular sites. The atomic displacement parameters were refined anisotropically for all atoms. This sample was also

24

observed to contain $\approx 5\%$ of an unknown impurity phase. This impurity phase was not observed to be consistent with any other known binary, ternary, or oxide combinations of the starting elements.

2.3.3 Physical Properties
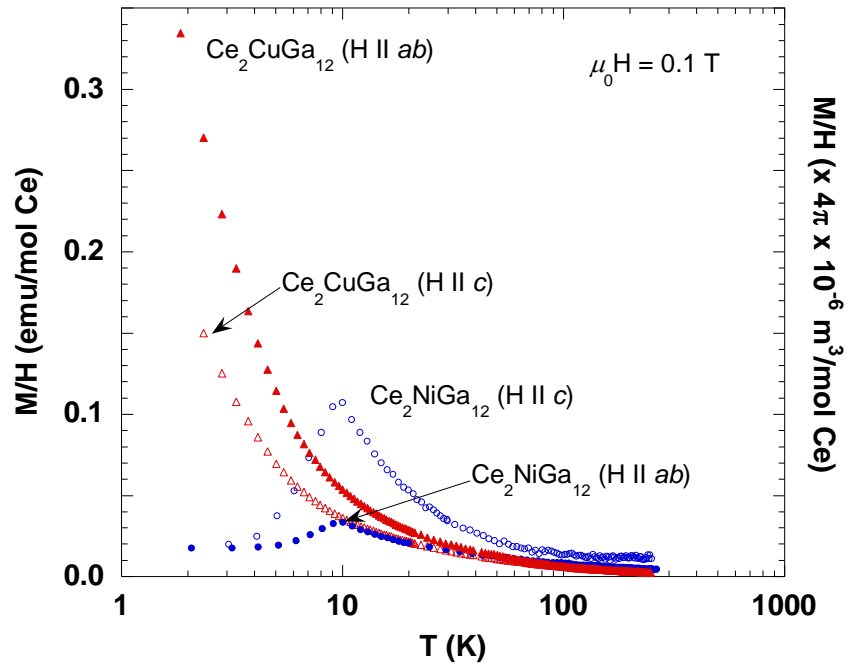
Figure 2.3 Magnetic susceptibility (emu/mol Ce) of Ce_2MGa_{12} (M = Ni, Cu) as a function of temperature is shown. Closed and open markers represent data collected with field parallel and perpendicular to the crystallographic c-axis of Ce_2MGa_{12} (M = Ni, Cu), respectively. Error bars represent ($+/-$) the standard uncertainty of each measurements.

Temperature-dependent magnetic susceptibility of single crystals of Ce_2MGa_{12} (M = Ni, Cu) is shown in Figure 2.3. An external magnetic field (μ_0H) of 0.1 T was applied along both the c-axis and the ab-plane of the crystal. A downturn in the magnetic susceptibility data for both directions of Ce_2NiGa_{12} suggests antiferromagnetic long range order at T_N = 10 K for both directions. In contrast, Ce_2CuGa_{12} does not magnetically order down to 2 K. The inverse magnetic susceptibility was fit from 20 K to 200 K and is not shown here. From this linear fit,

the effective moments, μ_{eff}, of Ce_2NiGa_{12} are 2.23 μ_B (2.07×10^{-23} Am^2/Ce) for H || c-axis and

2.31 μ_B (2.14×10^{-23} Am^2/Ce) for H || ab-plane, which are smaller than but close to the

calculated Ce^{3+} moment, $\mu_{eff} = 2.54$ μ_B (2.36×10^{-23} Am^2), with $\theta = -6.67$ K (H || c-axis) and $-$

16.97 K (H || ab-plane). A modified Curie-Weiss law: $\chi = \chi_0 + C/(T - \theta)$, was used to fit the data,

where χ_0 represents the temperature-independent term, C is the Curie constant, and θ is the Weiss

temperature. This result is consistent with Ce-moment antiferromagnetism for Ce_2NiGa_{12}. Also,

the effective moments of 2.28 μ_B (2.11×10^{-23} Am^2) for H || c-axis and 2.45 μ_B (2.27×10^{-23} Am^2)

for H || ab-plane for Ce_2CuGa_{12} are observed with the Weiss temperatures of $-$ 11.04 K (H || c-

axis) and $-$ 5.88 K (H || ab-plane) by using the same equation. The magnetic properties of

Ce_2MGa_{12} (M = Ni, Cu) are summarized in Table 2.4.

Table 2.4 Magnetic Properties of Ce_2MGa_{12} (M = Ni and Cu)

	C	θ (K)	χ_0 ($\times 10^{-5}$ emu/mol) ($\times 4\pi \times 10^{-6}$ m^3/mol)*	μ_{calc} (μ_B) ($\times 9.27 \times 10^{-24}$ Am^2)*	μ_{eff} (μ_B)	Fit range (K)	Ordering T_N (K)
Ce_2NiGa_{12}	0.62	-6.67	5.60	2.54	2.23	20-200	10 K (H || c)
	0.67	-16.97	0.12	2.54	2.31	20-200	10 K (H || ab)
Ce_2CuGa_{12}	0.65	-11.04	0.06	2.54	2.28	20-200	- (H || c)
	0.75	-5.88	0.38	2.54	2.45	20-200	- (H || ab)

*SI Units

Figure 2.4 shows isothermal magnetization data as a function of an external magnetic field

with the crystal aligned along the c-axis and ab-plane up to the field (μ_0H) of 9 T at 3 K. For

Ce_2NiGa_{12}, the experimental saturation is smaller than the calculated μ_{sat} of 2.14 μ_B (1.98×10^{-23}

Am^2) for Ce^{3+}. The magnetization of Ce_2NiGa_{12} linearly increases at low fields consistent with

antiferromagnetism. However, the data of Ce_2NiGa_{12} above 3 T show a jump indicating a

transition at $\approx$ 3 T. This is likely a spin-flop transition. The magnetization displays

paramagnetic behavior above the spin-flop transition. As the magnetic field increases, the magnetization of Ce_2CuGa_{12} increases, consistent with a paramagnet. However, above 2 T, the magnetization of Ce_2CuGa_{12} begins to saturate at 0.80 μ_B (7.42×10^{-24} Am^2) along the c-axis.
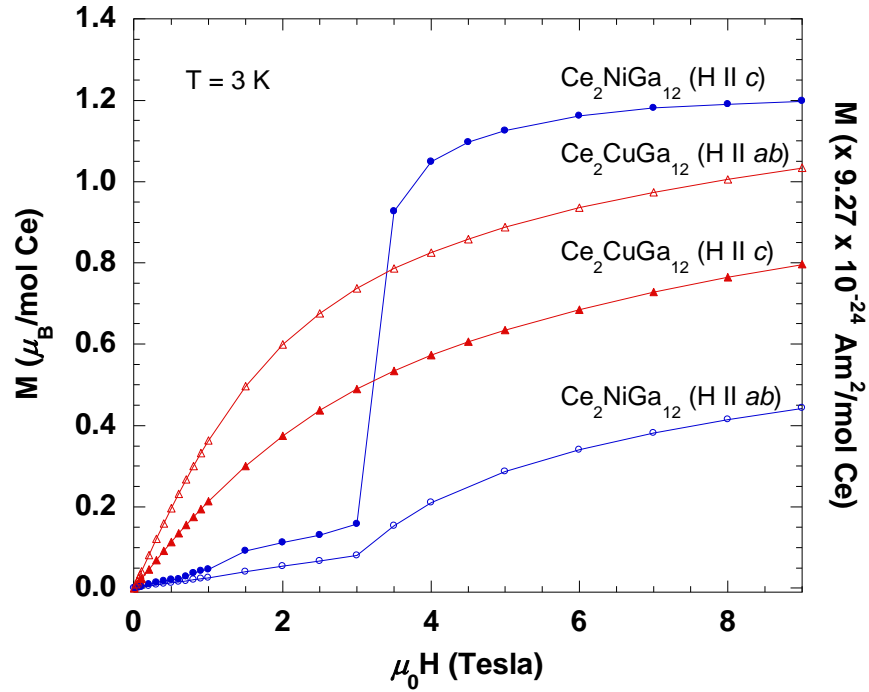
Figure 2.4 Magnetization of Ce_2MGa_{12} (M = Ni, Cu) as a function of magnetic field at 3K is shown. Closed and open markers represent data collected with field parallel and perpendicular to the crystallographic c-axis of Ce_2MGa_{12} (M = Ni, Cu), respectively.

Figure 2.5 shows the electrical resistivity of single crystals of Ln_2MGa_{12} (Ln = La, Ce; M = Ni, Cu) as a function of temperature in the ab-plane, where each compound shows metallic behavior with RRR (residual resistivity ratio) values of 98, 2.6, 4.1, and 4.5 for La_2NiGa_{12}, Ce_2NiGa_{12}, La_2CuGa_{12}, and Ce_2CuGa_{12}, respectively. The onset of a broad shoulder for Ce_2NiGa_{12}, which may be indicative of Kondo coherence, is observed in the resistivity below 100 K. A kink in the resistivity of Ce_2NiGa_{12} is observed at 10 K, which coincides with the magnetic ordering temperature and indicates a decrease in the spin disorder scattering. However,

the resistivity of La_2CuGa_{12} and Ce_2CuGa_{12} are similar and there is no indication of Kondo coherence in the Ce compound.
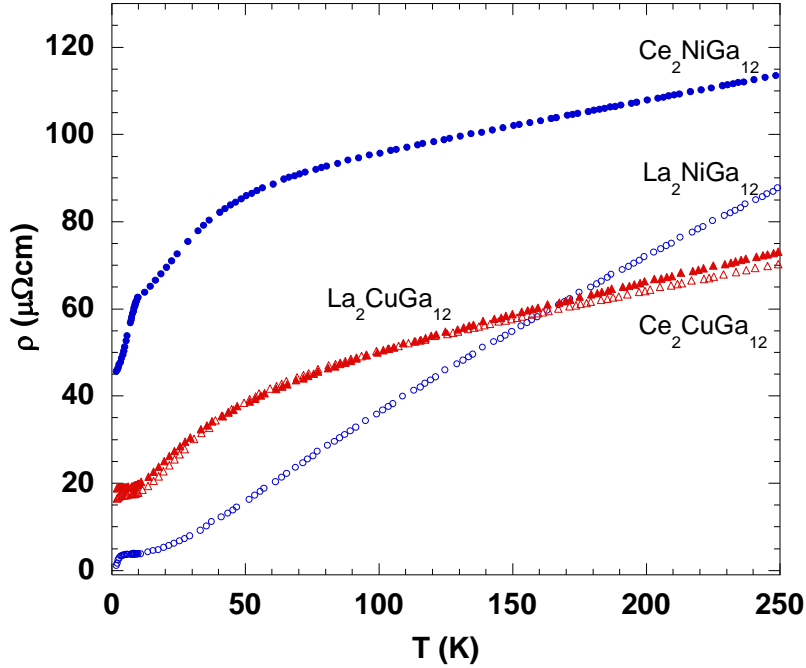
Figure 2.5 Normalized electrical resistivity of Ln_2MGa_{12} (Ln = La, Ce; M = Ni, Cu) as a function of temperature for current parallel to the *ab*-plane is shown.

Figure 2.6 shows the magnetoresistance (MR % = $(\rho_H - \rho_0)/\rho_0 \times 100$) of single crystals of Ln_2MGa_{12} (Ln = La, Ce; M = Ni, Cu) at 3 K as a function of field in the *ab*-plane. The Ln_2MGa_{12} (Ln = La, Ce; M = Ni, Ce) compounds except Ce_2NiGa_{12} show large positive magnetoresistance, with ratios up to 216 %, 86 % and 65 % at the field (μ_0H) of 9 T for La_2NiGa_{12}, La_2CuGa_{12}, and Ce_2CuGa_{12}, respectively. These values are much larger than MR < 10 %, which are typically found for most intermetallic compounds at low temperatures. This large positive magnetoresistance for Ce_2CuGa_{12} may be due to classical magnetoresistance, however it is considerably larger than typical intermetallics. The MR of La_2CuGa_{12} and Ce_2CuGa_{12} are similar. Based on the resistivity and magnetoresistance data, the Ce moments are decoupled from

the conduction electrons in Ce_2CuGa_{12}. The MR of La_2NiGa_{12} is linear and does not show signs of saturation. There have been several recent discoveries of a large non-saturating MR in low carrier density non-magnetic metals and semiconductors.[31-36] This effect is usually attributed to a change in the structural symmetry involving a possible transition to a charge density wave (CDW) state,[37] or due to high-field quantization effects.[31] However, there is no evidence for CDW in the transport. As such, the large linear MR in La_2NiGa_{12} warrants further investigation, and future work will focus on measuring the MR at higher fields. The MR of the Ce_2NiGa_{12} shows a rather sharp maximum ≈ 3 T, coinciding with the metamagnetic transition as shown in the inset of Figure 2.6.
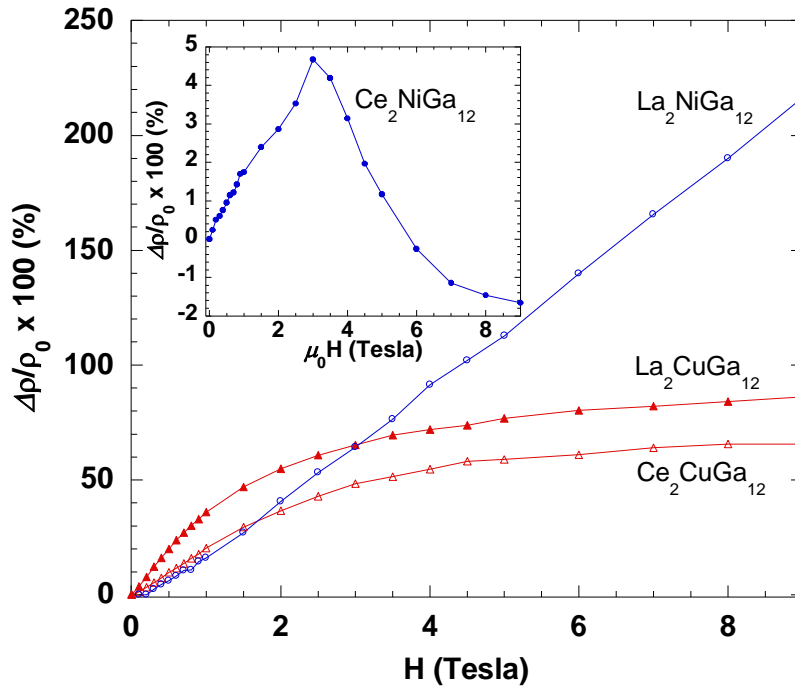
Figure 2.6 MR % of Ln_2MGa_{12} (Ln = La, Ce; M = Ni, Cu) as a function of field at 3 K is shown. The inset shows MR % of Ce_2NiGa_{12} for clarity.

The specific heat of Ln_2NiGa_{12} (Ln = La, Ce) is shown in Figure 2.7. A big jump up to 8 $Jmol^{-1}K^{-1}$ for Ce_2NiGa_{12} is consistent with its ordering temperature ($T_N \approx 10$ K) observed in the magnetic susceptibility data (See Fig. 2.3). As shown in the inset of Figure 2.7, after subtracting the phonon contribution to the heat capacity a $\gamma \approx 191$ $mJmol^{-1}K^{-2}$ is obtained, which indicates that Ce_2NiGa_{12} exhibits heavy-fermion behavior. Below the transition, γ decreases to 2.4 K and then shows an upturn to the lowest temperature. The gamma value remains large ($\gamma \approx 411$ $mJmol^{-1}K^{-2}$) at the lowest temperature. Figure 2.8 shows the specific heat of Ln_2CuGa_{12} (Ln = La, Ce). Although there is no evidence of a magnetic transition for Ce_2CuGa_{12} in the magnetic susceptibility data, the specific heat of Ce_2CuGa_{12} shows a sharp peak of ≈ 3.8 $Jmol^{-1}K^{-1}$ at ≈ 1.8 K, which corresponds to a second order magnetic transition which is not within the range of our susceptibility data. The Weiss temperatures along both crystallographic directions of Ce_2CuGa_{12} are negative, suggesting the transition observed in the specific heat is a bulk antiferromagnetic transition. To estimate the electronic contribution of the total heat capacity, the heat capacity of Ce_2CuGa_{12} as C/T versus T^2 is plotted in inset of Figure 2.8. The value of γ above the transition is 69 $mJmol^{-1}K^{-2}$, which indicates that the compound is a moderate heavy-fermion. Below the transition, at the lowest temperature, T = 0.4 K, gamma remains large ≈ 900 $mJmol^{-1}K^{-2}$. Integrating C/T over T gives the entropy (See Figure 2.9), which increases with temperature and almost saturates above the transition temperatures, reaching the value of 0.87Rln2 and 0.8Rln2 for Ce_2NiGa_{12} and Ce_2CuGa_{12}, respectively. This suggests that the magnetic ground state is a doublet for both compounds. The fact that the entropy does not recover the full Rln2 above the transition temperature might indicate the presence of the Kondo effect or mixed valence among the Ce ions, although the susceptibility data almost recovers the full Hund's rule moment for Ce^{3+}. Below 10 K, the electrical resistivity of Ce_2NiGa_{12} and Ce_2CuGa_{12} is proportional to T^2,
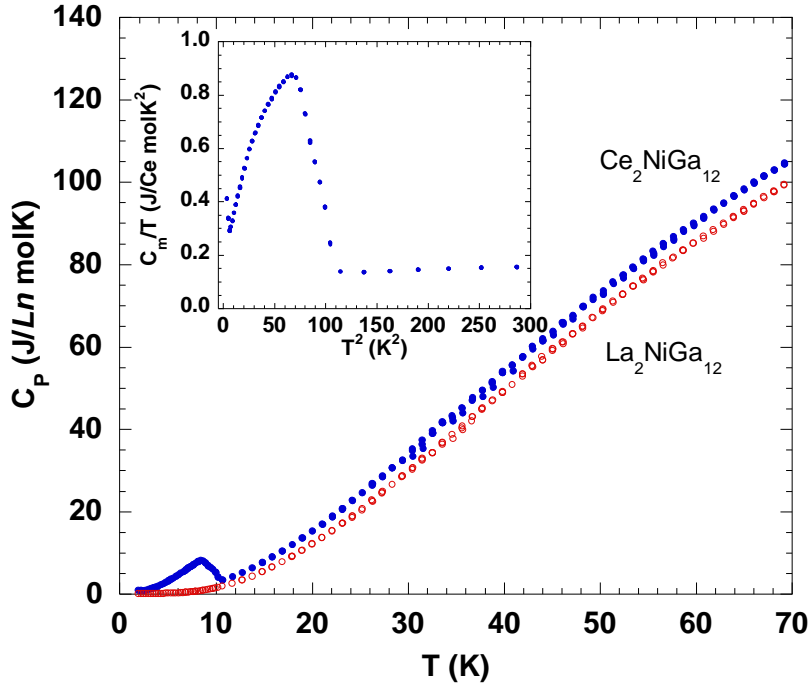
Figure 2.7 Specific heat of Ln_2NiGa_{12} (Ln = La, Ce) as a function of temperature. The inset shows C_m/T versus T^2 for Ce_2NiGa_{12} after subtracting lattice contribution.
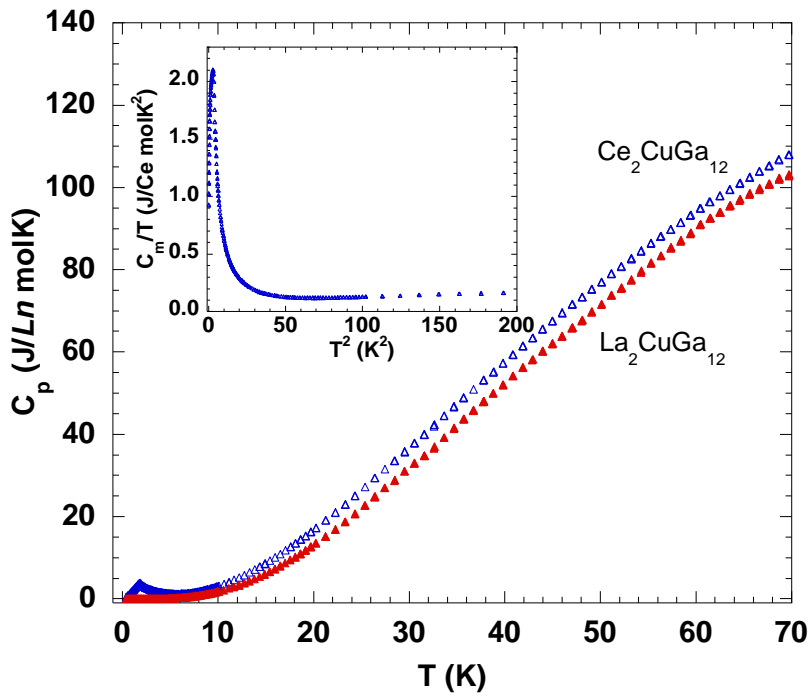
Figure 2.8 Specific heat of Ln_2CuGa_{12} (Ln = La, Ce) as a function of temperature. The inset shows C_m/T versus T^2 for Ce_2CuGa_{12} after subtracting lattice contribution.

indicating Fermi liquid behavior. The Kadowaki-Woods ratio (A/γ^2), where A represents the coefficient of the quadratic term in the temperature dependent resistivity, and γ is the coefficient of the linear term in the temperature dependent specific heat, has the value of $\approx 5.7 \times 10^{-6}$ and $\approx 8.3 \times 10^{-6}$ for Ce_2NiGa_{12} and Ce_2CuGa_{12}, respectively, which are close to what one would expect for heavy-fermion behavior.
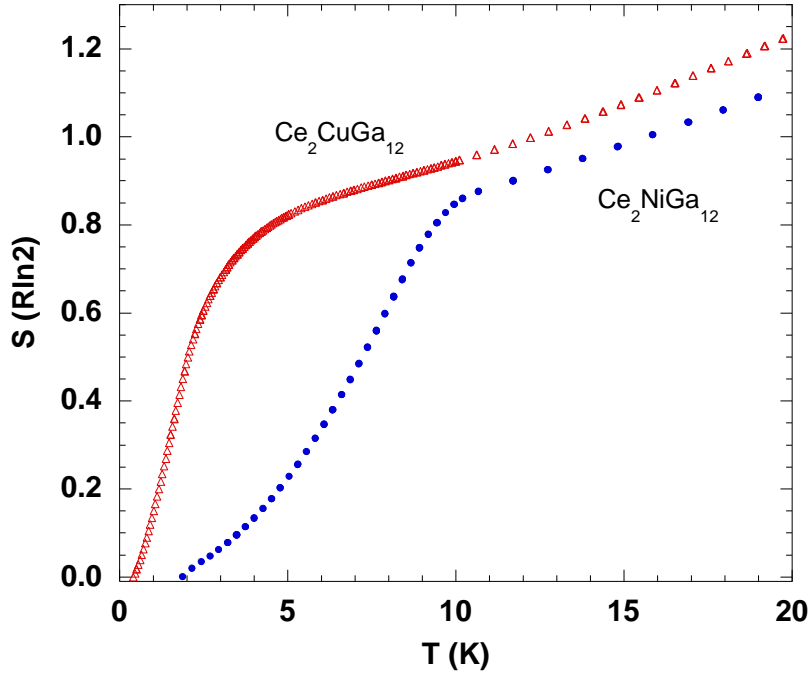
Figure 2.9 The magnetic entropy of Ce_2MGa_{12} (M = Ni, Cu) as a function of temperature.

In our previous work, we have suggested that the higher magnetic ordering temperature (T_N = 11 K) in Ce_2PdGa_{12} compared to $CePdGa_6$ may be attributed to increased hybridization between the Ce $4f$ electrons and conduction electrons (Ga), where the higher Ga contacts can contribute additional carriers to the magnetic Ce^{3+} ion.[5] Another factor involves the number of d electrons, which can be changed by substituting different transition metals M (M = Ni, Pd) to M = Cu in Ce_2MGa_{12}. Substitution of M = Ni, Pd to Cu results in the change in the number of

carriers. The evidence for a Kondo resonance found in the Ce_2NiGa_{12} is not found in the Ce_2CuGa_{12} sample, and this is evident in the transport data where the resistivity of the La_2CuGa_{12} is essentially the same with the Ce_2CuGa_{12} analog. Furthermore, the MR of the La_2CuGa_{12} and Ce_2CuGa_{12} is similar as well. Also, the Ce and La analogs with Ni show a linear MR with fields (μ_0H) up to 3 T before the Ce undergoes a magnetic transition. Our future work will focus on the synthesis of CeMGa$_6$ analogues of Ni and Cu to compare with Ce$_2M$Ga$_{12}$.

2.4 References

(1)   Fisk, Z.; Hess, D. W.; Pethick, C. J.; Pines, D.; Smith, J. L.; Thompson, J. D.; Willis, J. O. *Science* **1988**, *239*, 33-42.

(2)   Stewart, G. R. *Rev. Modern Phys.* **1984**, *56*, 755-787.

(3)   Fisk, Z.; Sarrao, J. L.; Thompson, J. D. *Curr. Opin. Solid State Mater. Sci.* **1996**, *1*, 42-46.

(4)   Fisk, Z.; Sarrao, J. L.; Smith, J. L.; Thompson, J. D. *Proc. Natl. Acad. Sci.USA* **1995**, *92*, 6663-6667.

(5)   Macaluso, R. T.; Millican, J. N.; Nakatsuji, S.; Lee, H.-O.; Carter, B.; Moreno, N. O.; Fisk, Z.; Chan, J. Y. *J. Solid State Chem.* **2005**, *178*, 3547-3553.

(6)   Petrovic, C.; Pagliuso, P. G.; Hundley, M. F.; Movshovich, R.; Sarrao, J. L.; Thompson, J. D.; Fisk, Z.; Monthoux, P. *J. Phys.: Condens. Matter* **2001**, *13*, L337-L342.

(7)   Macaluso, R. T.; Sarrao, J. L.; Moreno, N. O.; Pagliuso, P. G.; Thompson, J. D.; Fronczek, F. R.; Hundley, M. F.; Malinowski, A.; Chan, J. Y. *Chem. Mater.* **2003**, *15*, 1394-1398.

(8)   Nicklas, M.; Sidorov, V. A.; Borges, H. A.; Pagliuso, P. G.; Petrovic, C.; Fisk, Z.; Sarrao, J. L.; Thompson, J. D. *Phys. Rev. B: Condens. Matter* **2003**, *67*, 020506/1-020506/4.

(9)   Hedo, M.; Kurita, N.; Uwatoko, Y.; Chen, G.; Ohara, S.; Sakamoto, I. *J. Magn. Magn. Mater.* **2004**, *272-276*, 146-147.

(10)   Steglich, F.; Aarts, J.; Bredl, C. D.; Lieke, W.; Meschede, D.; Franz, W.; Schaefer, H. *Phys. Rev. Lett.* **1979**, *43*, 1892-1896.

(11)   Chen, X. Z.; Small, P.; Sportouch, S.; Zhuravleva, M.; Brazis, P.; Kannewurf, C. R.; Kanatzidis, M. G. *Chem. Mater.* **2000**, *12*, 2520-2522.

(12) Mathur, N. D.; Grosche, F. M.; Julian, S. R.; Walker, I. R.; Freye, D. M.; Haselwimmer, R. K. W.; Lonzarich, G. G. *Nature* **1998**, *394*, 39-43.

(13) Grier, B. H.; Lawrence, J. M.; Murgai, V.; Parks, R. D. *Phys. Rev. B* **1984**, *29*, 2664.

(14) Steglich, F. *Physica B* **2005**, *359-361*, 326-332.

(15) Bauer, E.; Gignoux, D.; Schmitt, D.; Winzer, K. *J. Magn. Magn. Mater.* **1987**, *69*, 158-162.

(16) Dhar, S. K.; Gschneidner, K. A., Jr. *J. Magn. Magn. Mater.* **1989**, *79*, 151-153.

(17) Bauer, E.; Pillmayr, N.; Gratz, E.; Gignoux, D.; Schmitt, D.; Winzer, K.; Kohlmann, J. *J. Magn. Magn. Mater.* **1988**, *71*, 311-17.

(18) Larson, A. C.; Von Dreele, R. B. *GSAS-Generalized Structure Analysis System*: LANSCE, MS-H805, Los Alamos National Laboratory, Los Alamos, NM 87545 USA, **2000**.

(19) Toby, B. H. *J. Appl. Crystallogr.* **2001**, *34*, 210-213.

(20) Kimmel, G.; Dayan, D.; Grill, A.; Pelleg, J. *J. Less-Common Met.* **1980**, *75*, 133-140.

(21) Yatsenko, S. P.; Semyannikov, A. A.; Semenov, B. G.; Chuntonov, K. A. *J. Less-Common Met.* **1979**, *64*, 185-199.

(22) Dayan, D.; Pelleg, J.; Guisser, R. *J. Less-Common Met.* **1979**, *68*, 199-205.

(23) Dzyana, D. I.; Gladishevs'kii, E. I.; Krip'yakevich, P. I. *Dopov. Akad. Nauk Ukr. RSR, Ser. A* **1968**, *30*, 282-284.

(24) Nicklas, M.; Moreno, N. O.; Borges, H. A.; Bauer, E. D.; Sarrao, J. L.; Thompson, J. D. *J. Magn. Magn. Mater.* **2004**, *272-276*, E111-E112.

(25) Grin, Y. N. *Dopov. Akad. Nauk Ukr. RSR, Ser. A* **1982**, 76-9.

(26) El-Boragy, M.; Schubert, K. *Z. MetaIlkd.* **1972**, *63*, 52-53.

(27) Stokhuyzen, R.; Brandon, J. K.; Chibh, P. C.; Pearson, W. B. *Acta Crystallogr., Sect. B: Struct. Sci* **1974**, *B30*, 2910-2911.

(28) Feschotte, P.; Eggimann, P. *J. Less-Common Met.* **1979**, *63*, 15-30.

(29) Yarmolyuk, Y. P.; Grin, Y. N.; Rozhdestvenskaya, I. V.; Usov, O. A.; Kuz'min, A. M.; Bruskov, V. A.; Gladyshevskii, E. I. *Kristallografiya* **1982**, *27*, 999-1001.

(30) Emsley, J. *The Elements*; 3rd ed.; Oxford University Press: New York, 1998.

(31) Abrikosov, A. A. *Phys. Rev. B: Condens. Matter* **1999**, *60*, 4231-4234.

(32) Lifshits, I. M.; Peshanskii, V. G. *Sov. Phys. JETP* **1959**, *8*, 875.

(33) Falicov, L. M.; Smith, H. *Phys. Rev. Lett.* **1972**, *29*, 124-127.

(34) Soule, D. E. *Phys. Rev.* **1958**, *112*, 698-707.

(35) Butko, V. Y.; DiTusa, J. F.; Adams, P. W. *Phys. Rev. Lett.* **2000**, *85*, 162-165.

(36) Young, D. P.; Goodrich, R. G.; DiTusa, J. F.; Guo, S.; Adams, P. W.; Chan, J. Y.; Hall, D. *Appl. Phys. Lett.* **2003**, *82*, 3713-3715.

(37) Overhauser, A. W. *Phys. Rev. B* **1971**, *3*, 3173-3182.

CHAPTER 3. CRYSTAL GROWTH AND PHYSICAL PROPERTIES OF Ln_2CuGa_{12} (Ln = Pr, Nd, and Sm)

3.1 Introduction

Layered ternary intermetallic compounds, consisting of lanthanide, transition metal, and main group elements have extensively been studied because of their exotic physical properties such as magnetism, heavy-fermion behavior, and large magnetoresistance due to hybrization of the f-electrons of lanthanide atoms and the conduction electrons.[1-5] $SmMn_2Ge_2$[6,7] and $SmPd_2Ga_2$,[8] which are isostrucutral to $ThCr_2Si_2$[9] structure type, show large negative and positive magnetoresistance with 47 % at 9 T and 100 % at 9 T, respectively. $PrMnSi_2$,[10] one of layered intermetallic compounds, also shows large negative magnetoresistance up to 47 % at 9 T. Interestingly, both of these two different type compounds have repeated magnetic layers in their structure. In $SmMn_2Ge_2$ and $SmPd_2Ga_2$ compounds the magnetic atom (Sm and Mn) layers repeat regularly along the c-axis. Similarly, the $PrMnSi_2$ compound has the repeated multilayer of magnetic Pr and Mn atoms along b-axis.

Recently, the layered Ce_2CuGa_{12}[11] compounds adopting Sm_2NiGa_{12}[12] structure type from our own work have been synthesized and show large magnetoresistance up to 65 % at 9 Tesla. This structure can also be viewed as a repeated layered three-dimensional network of [CuGa] with the layers of Ce atoms occupying cavities made of Ga atoms. Besides, Ce_2CuGa_{12} exhibits an enhanced γ value ~ 69 mJ/mol-K^2 which is leading us to exploring other Ln-Cu-Ga system by using Ga flux. We have synthesized Ln_2CuGa_{12} (Ln = Pr, Nd, Sm), which are isostructural to the layered Sm_2NiGa_{12} compound. In this paper we report the structures and physical properties of Ln_2CuGa_{12} (Ln = Pr, Nd, Sm).

3.2 Experimental

3.2.1 Synthesis

Single crystals of Ln_2CuGa_{12} (Ln = Pr, Nd, and Sm) were synthesized by flux growth methods. Pr, Nd, or Sm (3N Alfa Aesar) ingot, Cu powder (5N, Alfa Aesar), and Ga (6N, Alfa Aesar) were placed into an alumina crucible in a 1.5:1:15 stoichiometric ratio. The crucible and its contents were then sealed into an evacuated fused silica tube and heated up to 1423 K for 7 h. After fast cooling to 673 K at a rate of 150 K/h, the tube was then slowly cooled to 573 K at a rate of 8 K/h and immediately inverted and spun with a centrifuge for the removal of excess Ga flux. Silver-color plate-like crystals were found, and typical crystal size ranged from $1 \times 2 \times 2$ to $1 \times 2 \times 5$ mm^3. The crystals were not observed to degrade in air.

3.2.2 Single-Crystal X-ray Diffraction

$0.025 \times 0.025 \times 0.05$ mm^3 silver-colored fragments of Ln_2CuGa_{12} (Ln = Pr, Nd, and Sm) were mounted onto the goniometer of a Nonius KappaCCD diffractometer equipped with MoK$_\alpha$ radiation (λ = 0.71073 Å). Data were collected up to θ = 30.0° at 293 K. Further crystallographic parameters for Ln_2CuGa_{12} (Ln = Pr, Nd, and Sm) are provided in Table 3.1. The space group and atomic positions from Sm_2NiGa_{12} were used as an initial structural model for the structure determination of Ln_2CuGa_{12} (Ln = Pr, Nd, and Sm) compound. The structural model was refined using SHELXL97. Data were also corrected for extinction and refined with anisotropic displacement parameters. Atomic positions and displacement parameters for compounds are provided in Table 3.2, and selected interatomic distances are presented in Table 3.3.

3.2.3 Physical Property Measurements

Magnetization data were obtained using a Quantum Design Physical Property Measurement System. The temperature-dependent magnetization data were obtained first under

37

Table 3.1 Crystallographic Data for Ln_2CuGa_{12} (Ln = Pr, Nd, and Sm)

Crystal data			
Formula	Pr_2CuGa_{12}	Nd_2CuGa_{12}	Sm_2CuGa_{12}
a	6.0780(5)	6.0460(6)	6.0100(3)
c	15.3680(11)	15.3340(12)	15.3180(8)
V	567.73(8)	560.52(9)	553.29(5)
Z	2	2	2
Crystal dimension (mm^3)	0.03×0.05×0.05	0.05×0.05×0.05	0.03×0.05×0.05
Crystal system	Tetragonal	Tetragonal	Tetragonal
Space group	*P4/nbm*	*P4/nbm*	*P4/nbm*
θ range (°)	2.65-30.01	2.66-30.01	2.66-30.03
μ (mm^{-1})	38.110	39.171	40.912
Data collection			
Measured reflections	1418	1198	1438
Independent reflections	477	472	466
Reflections with $I>2\sigma(I)$	414	370	415
R_{int}	0.0370	0.0520	0.0337
h	-8→8	-8→8	-8→8
k	-6→6	-6→6	-5→5
l	-21→16	-21→17	-19→21
Refinement			
[a]$R^1[F^2>2\sigma(F^2)]$	0.0332	0.0456	0.0377
[b]$wR^2(F^2)$	0.0815	0.1249	0.1080
Reflections	477	472	466
Parameters	26	26	26
$\Delta\rho_{max}$ (eÅ^{-3})	2.487	3.334	2.641
$\Delta\rho_{min}$ (eÅ^{-3})	-2.830	-4.008	-5.236

[a] $R_1 = \sum ||F_o|-|F_c||/\sum|F_o|$

[b] $wR_2 = [\sum[w(F_o^2 - F_c^2)]/\sum[w(F_o^2)^2]]^{1/2}$

Table 3.2 Atomic Positions and Thermal Parameters for Ln_2CuGa_{12} (Ln = Pr, Nd, and Sm)

Atom	Wyckoff position	x	y	z	U_{eq} (Å^2)[a]
Pr	4h	3/4	1/4	0.24652(4)	0.0073(2)
Cu	2c	3/4	1/4	0	0.0152(5)
Ga1	4g	3/4	3/4	0.17783(8)	0.0101(3)
Ga2	4g	3/4	3/4	0.33634(9)	0.0117(3)
Ga3	8m	0.50038(12)	0.00038(12)	-0.08518(6)	0.0123(3)
Ga4	8m	0.56338(17)	0.06338(17)	0.42639(7)	0.0241(4)
Nd	4h	3/4	1/4	0.24684(6)	0.0099(4)
Cu	2c	3/4	1/4	0	0.0303(10)
Ga1	4g	3/4	3/4	0.17735(13)	0.0129(5)
Ga2	4g	3/4	3/4	0.33574(14)	0.0147(5)
Ga3	8m	0.5006(2)	0.0006(2)	-0.08455(9)	0.0181(5)
Ga4	8m	0.5645(3)	0.0645(3)	0.42656(11)	0.0251(5)
Sm	4h	3/4	1/4	0.24675(4)	0.0070(3)
Cu	2c	3/4	1/4	0	0.0249(8)
Ga1	4g	3/4	3/4	0.17824(11)	0.0101(4)
Ga2	4g	3/4	3/4	0.33566(12)	0.0112(4)
Ga3	8m	0.50041(17)	0.00041(17)	-0.08516(8)	0.0148(4)
Ga4	8m	0.5673(2)	0.0673(2)	0.42666(9)	0.0200(4)

[a]U_{eq} is defined as one-third of the trace of the orthogonalized U_{ij} tensor.

Table 3.3 Selected Interatomic Distances (Å) for Ln_2CuGa_{12} (Ln = Pr, Nd, and Sm)

Pr_2CuGa_{12}		Nd_2CuGa_{12}		Sm_2CuGa_{12}	
Pr layer		Nd layer		Sm layer	
Pr-Ga1 (×4)	3.2171(5)	Nd-Ga1 (×4)	3.2053(8)	Sm-Ga1 (×4)	3.1830(6)
Pr-Ga4 (×2)	3.1960(12)	Nd-Ga4 (×2)	3.1798(18)	Sm-Ga4 (×2)	3.1632(15)
Pr-Ga3 (×2)	3.2790(11)	Nd-Ga3 (×2)	3.2772(18)	Sm-Ga3 (×2)	3.2600(14)
Pr-Ga3 (×2)	3.2833(11)	Nd-Ga3 (×2)	3.2840(18)	Sm-Ga3 (×2)	3.2645(14)
CuGa$_{8/2}$ segment		CuGa$_{8/2}$ segment		CuGa$_{8/2}$ segment	
Cu-Ga3 (×4)	2.5134(10)	Cu-Ga3 (×4)	2.4956(17)	Cu-Ga3 (×4)	2.4904(14)
Cu-Ga3 (×4)	2.5190(10)	Cu-Ga3 (×4)	2.5044(17)	Cu-Ga3 (×4)	2.4963(14)
Ga1-Ga3 (×4)	2.5778(9)	Ga1-Ga3 (×4)	2.5679(14)	Ga1-Ga3 (×4)	2.5589(11)
Ga-only segment		Ga-only segment		Ga-only segment	
Ga2-Ga4 (×4)	2.6134(10)	Ga2-Ga4 (×4)	2.6101(15)	Ga2-Ga4 (×4)	2.6048(12)
Ga4-Ga4 (×1)	2.511(2)	Ga4-Ga4 (×1)	2.508(3)	Ga4-Ga4 (×1)	2.521(3)

zero-field cooled (ZFC) conditions from 2 K to 300 K with an applied field 0.1 T. Magnetization data were then measured upon heating to obtain field-cooled (FC) data after cooling to 2 K under field. Field-dependent measurements were collected at 3 K with H swept between 0 T and 9 T. In addition, data were also collected for the crystals oriented with respect to the crystallographic axes. The electrical resistivity data were measured by the standard four-probe AC technique.

3.3 Results and Discussion

3.3.1 Synthesis and Structure

We have reported the optimized synthesis route for Ce_2PdGa_{12} and Ce_2CuGa_{12} and realized that this structure type (We call it 2-1-12 for convenience) can be formed at low temperature ranges with Ga rich reaction ratio. As already well known, the $ThCr_2Si_2$[9] structure type in the *Ln-M-X* (*Ln* = lanthanide, *M* = transition metal, *X* = main group elements) ternary system is a robust and thermodynamically favored form. Therefore, several synthetic attempts for growing 2-1-12 phase have shown the $ThCr_2Si_2$ phase as a minor impurity from our work. To avoid forming thermodynamically favored phases such as $ThCr_2Si_2$ structure type and some other binary phases, the reaction mixtures were applied to fast cooling isotherm first at high temperature ranges (from 1423 K to 673 K), and then slow cooled at low temperature ranges as described in synthesis section. From these kinetic control experiments, the slow cooling step is the key and in small temperature ranges for forming 2-1-12 phase. Also, the reaction ratio of elements plays an important role to obtain the right phase and avoid the unwanted phases. To obtain the phase-pure 2-1-12 compounds, the reaction ratio should be close enough to the stoichiometry of mole ratios of the formula. In addition, although we have tried to synthesize the late lanthanide analogues, we are not able to grow the 2-1-12 phase for the late lanthanide

elements from Gd to Yb. Instead of obtaining 2-1-12 phases for the late lanthanide elements, an unknown phase was found from the same synthetic routes to those of Ln_2CuGa_{12} (Ln = Pr, Nd, and Sm) and is still under characterization.
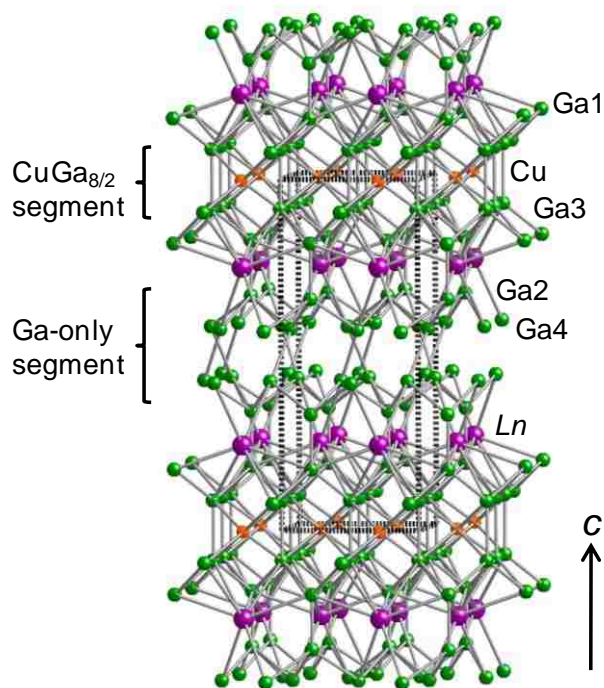
Figure 3.1 The crystal structure of Ln_2CuGa_{12} (Ln = Pr, Nd, Sm) is shown along the c-axis, where the Ln atoms are represented with big spheres; the Cu atoms are denoted as white spheres; and the Ga atoms are denoted with blue spheres. Dashed lines are used to show the unit cell.

Ln_2CuGa_{12} (Ln = Pr, Nd, and Sm) crystallize in tetragonal $P4/nbm$ space group (No. 125, origin choice 2) with the Ln (Ln = Pr, Nd, and Sm), Cu, Ga1, Ga2, Ga3 and Ga4 occupying the $4h$, $2c$, $4g$, $4g$, $8m$, and $8m$ respectively. This structure is composed of the alternating layers, along the crystallographic c-axis, of [CuGa] with Ln (Ln = Pr, Nd, and Sm) atoms occupying in cavities made of Ga atoms as shown in Figure 3.1.

Figure 3.2 shows the linear variation of cell volumes for Ln_2CuGa_{12} (Ln = Ce, Pr, Nd, and Sm) with the rare earth ionic radii due to lanthanide contraction. The interatomic distances in the

41

local *Ln* environment of Ln_2CuGa_{12} (*Ln* = Pr, Nd, and Sm) where *Ln* atoms are connected to 10 Ga atoms. These interatomic distances are listed in Table 3.3. The decrease of *Ln*-Ga distances in the local *Ln* environments from Ce to Sm follows the trend of cell volumes for Ln_2CuGa_{12} (*Ln* = Ce, Pr, Nd, and Sm). Also, they are in good agreement with those found in other binary and ternary systems such as $LnGa_6$,[13] Ln_3Ga,[14,15] and $LnCuGa_3$ (*Ln* = Pr, Nd, Sm).[16,17]
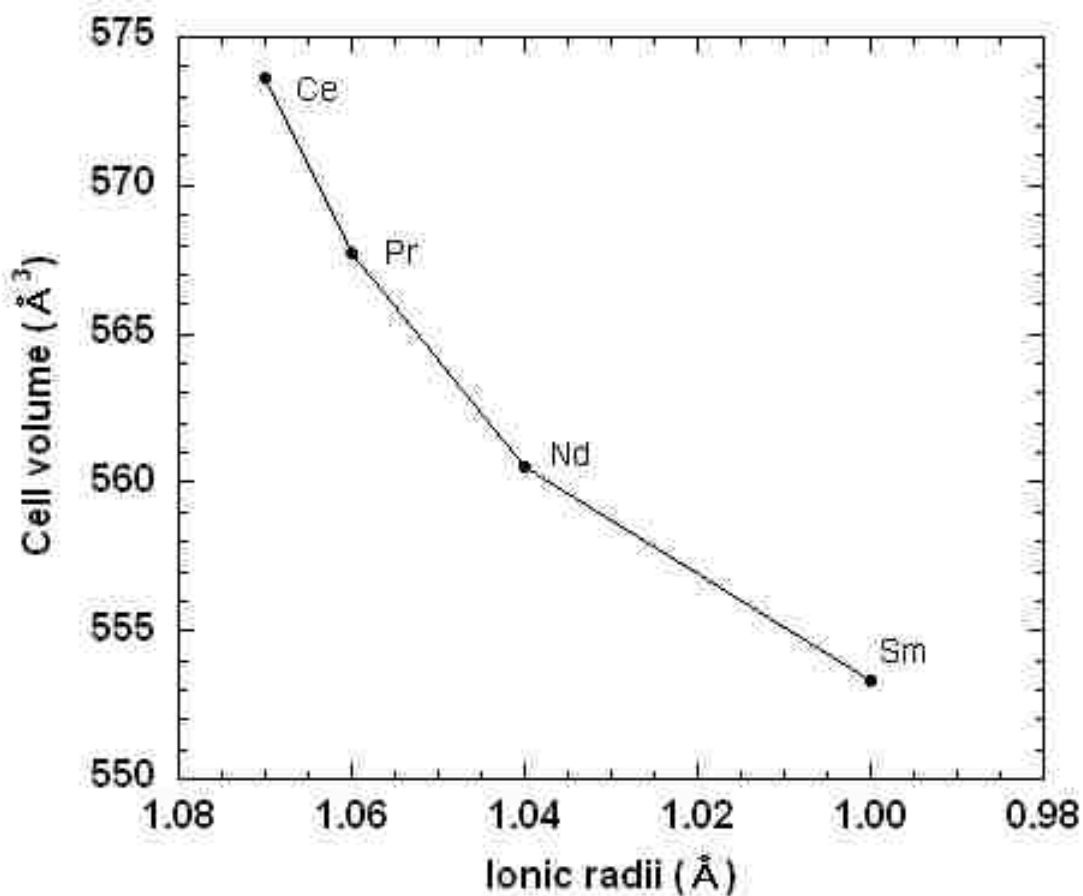
Figure 3.2 Cell volume of Ln_2CuGa_{12} (*Ln* = Pr, Nd, Sm) as a function of ionic radius.

Within $CuGa_{8/2}$ rectangular prisms, which are edged-shared and parts of the [CuGa] subunit layers, Cu-Ga3 (×8) distances ranged from 2.4904(14) ÅÅ to 2.5190(10) Å are in good agreement with the sum of the atomic radii of Cu (1.25 Å) and Ga (1.26 Å).
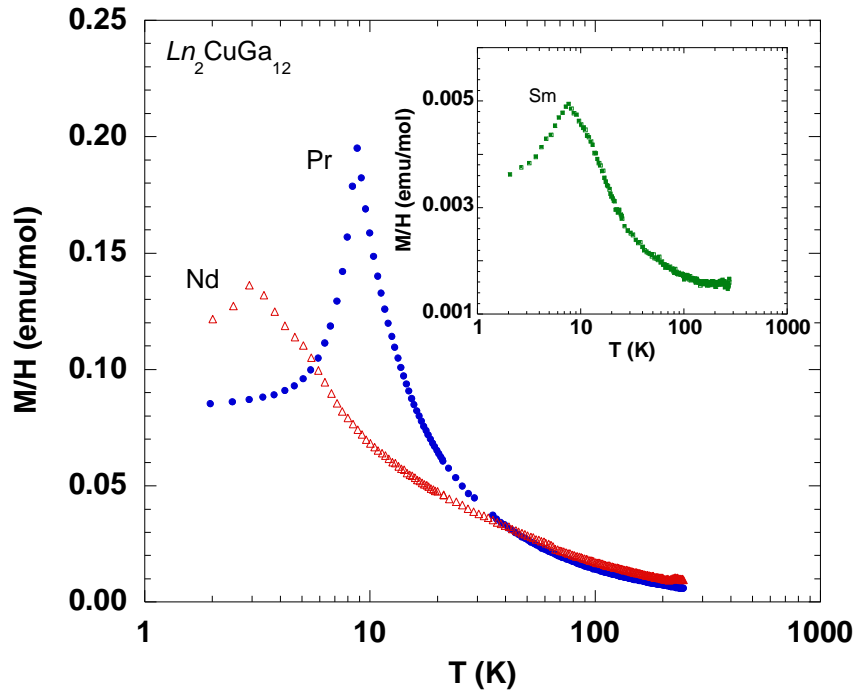
Figure 3.3 Magnetic susceptibility (emu/mol *Ln*) of *Ln*$_2$CuGa$_{12}$ (*Ln* = Pr, Nd, Sm) as a function of temperature is shown. Closed circles, open triangles, and closed rectangles represent data along the *c*-axis for Pr$_2$CuGa$_{12}$, Nd$_2$CuGa$_{12}$, and Sm$_2$CuGa$_{12}$, respectively. The inset shows inverse susceptibility as a function of temperature.

3.3.2 Physical Properties

Magnetic susceptibilities as a function of temperature under an applied field of 0.1 T along the crystallographic *c*-axis of single crystals *Ln*$_2$CuGa$_{12}$ (*Ln* = Pr, Nd, and Sm) are shown in Figure 3.3. *Ln*$_2$CuGa$_{12}$ (*Ln* = Pr, Nd, and Sm) show antiferromagnetic ordering at 8.7 K, 2.9 K, and 7.6 K for Pr$_2$CuGa$_{12}$, Nd$_2$CuGa$_{12}$, and Sm$_2$CuGa$_{12}$, respectively. The inset of Figure 3.3 shows the magnetic susceptibility of Sm$_2$CuGa$_{12}$ for clarity. A modified Curie-Weiss equation; χ (T) = χ_0 + C/(T − θ) was used to obtain the magnetic moments for each lanthanide ion, where χ_0 represents the temperature-independent term, C is the Curie constant, and θ is the Weiss temperature. From fitting the magnetic susceptibility from 20 K to 250 K (from 20 K to 200 K for Sm analogue), the effective moments, μ_{eff}, are 3.25 μ_B (Pr$_2$CuGa$_{12}$), 3.85 μ_B (Nd$_2$CuGa$_{12}$), and

0.52 μ_B (Sm$_2$CuGa$_{12}$), which are close to the calculated Pr^{3+} (3.58 μ_B), Nd^{3+} (3.62 μ_B), and Sm^{3+}

(0.84 μ_B) moment with Weiss constants of -0.71 K, -20.87 K, and 1.43 K for Pr, Nd, and Sm

compound, respectively. In contrast to Pr and Nd analogues, the inverse magnetic susceptibility

of Sm$_2$CuGa$_{12}$ compound shows curvilinear behavior in the paramagnetic region (not shown

here), which is usually found for Sm-based compounds results from an unusual electronic

structure of the Sm^{3+} ion between the $J = 5/2$ ground state and $J = 7/2$ excited multiplet state.[18,19]
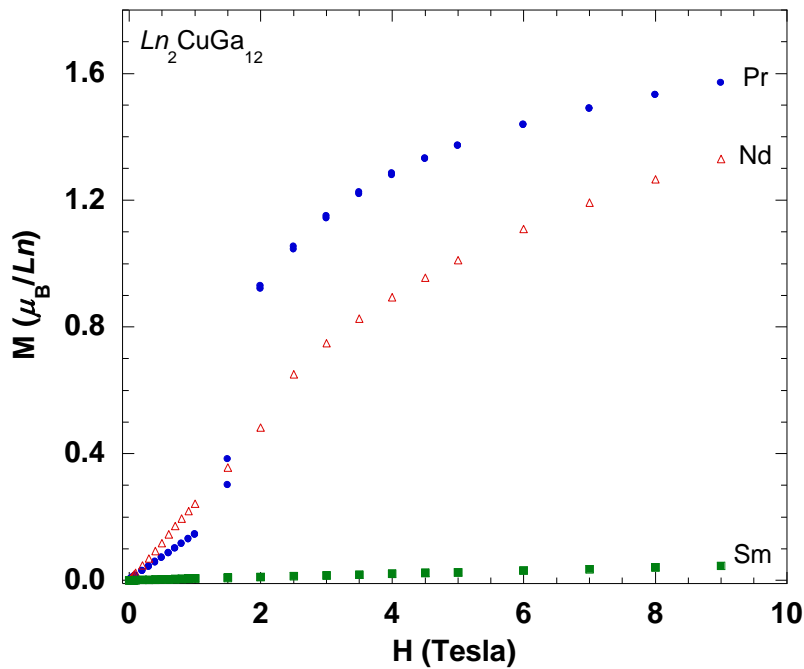
Figure 3.4 Magnetization of Ln_2CuGa$_{12}$ (Ln = Pr, Nd, Sm) as a function of magnetic field at 3K is shown. Closed circles, open triangles, and closed rectangules represent data along the c-axis for Pr$_2$CuGa$_{12}$, Nd$_2$CuGa$_{12}$, and Sm$_2$CuGa$_{12}$, respectively.

Figure 3.4 shows the isothermal magnetization data versus an applied field along the c-axis

at 3 K. The magnetization of Pr$_2$CuGa$_{12}$ linearly increases up to around 1.5 T. However, the

data of Pr$_2$CuGa$_{12}$ at around 1.5 T show a deviation from the linearity and increase sharply up to

2 T, which indicates a meta-magnetic transition. Also, Nd$_2$CuGa$_{12}$ shows similar behavior to

Pr_2CuGa_{12} at around 2 T. However, as an applied magnetic field increases, magnetization of Sm_2CuGa_{12} increases linearly up to 9 T without any deviations.
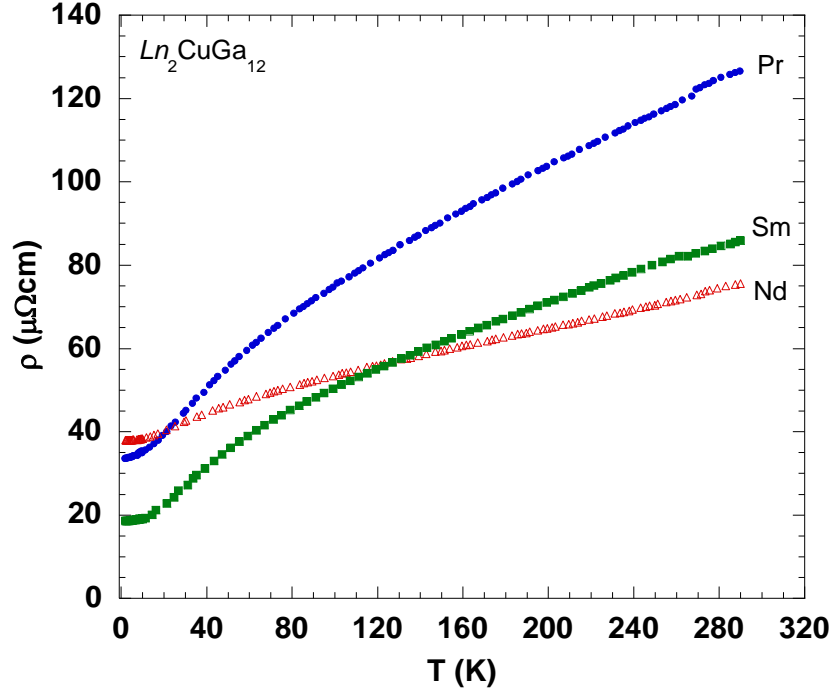
Figure 3.5 Normalized electrical resistivity of Ln_2CuGa_{12} (Ln = Pr, Nd, Sm) as a function of temperature for current parallel to the *ab*-plane is shown.

The temperature-dependent electrical resistivity of single crystals of Ln_2CuGa_{12} (Ln = Pr, Nd, and Sm) along the *ab*-plane is shown in Figure 3.5. All compounds show metallic behavior with RRR (residual resistivity ratio) values of 3.8, 2.0, and 4.6 for Pr_2CuGa_{12}, Nd_2CuGa_{12}, and Sm_2CuGa_{12}, respectively. The Figure 3.6 shows the magnetoresistance (MR % = $(\rho_H - \rho_0)/\rho_0 \times$ 100) of a single crystal of Ln_2CuGa_{12} (Ln = Pr, Nd, and Sm) as a function of field at 3 K along the *ab*-plane. A large positive magnetoresistance, 35 %, 10 % and 130 % at 9 T for Pr_2CuGa_{12}, Nd_2CuGa_{12}, and Sm_2CuGa_{12}, respectively is represented. This large positive magnetoresistance for Ln_2CuGa_{12} (Ln = Pr, Nd, and Sm) may be caused by electron-spin scattering at low
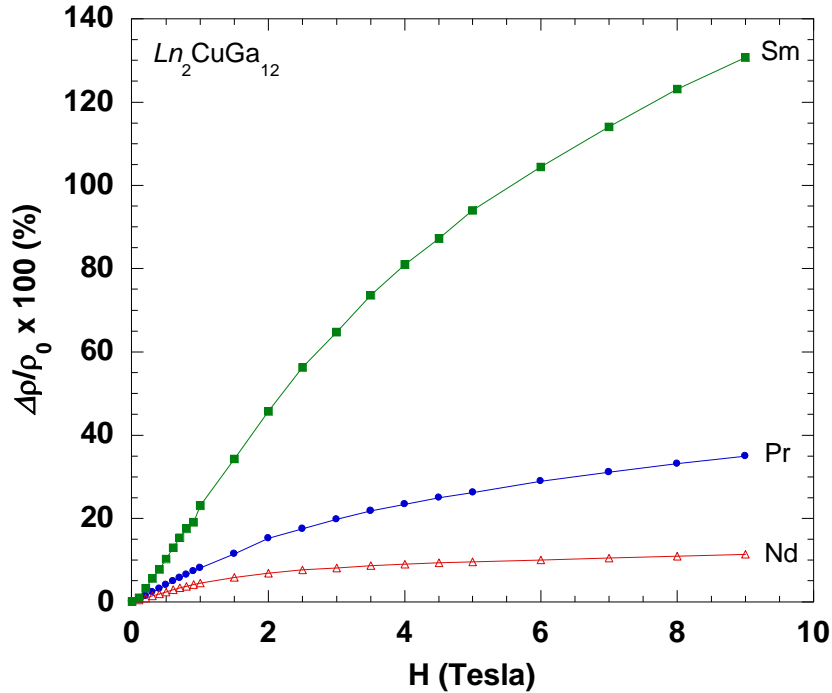
Figure 3.6 MR % of Ln_2CuGa_{12} (Ln = Pr, Nd, Sm) as a function of field at 3 K is shown.

temperatures.   Similar behavior has been reported in $SmPd_2Ga_2$, which has a large positive

magnetoresistance up to around 100 % at 9 T and 2 K.

3.4 References

(1)   Fisk, Z.; Sarrao, J. L.; Smith, J. L.; Thompson, J. D. *Proc. Natl Acad. Sci.USA* **1995**, *92*, 6663-7.

(2)   Fisk, Z.; Sarrao, J. L.; Thompson, J. D. *Curr. Opin. Solid State Mater. Sci.* **1996**, *1*, 42-46.

(3)   Maple, M. B. *J. Phys. Soc. Jpn.* **2005**, *74*, 222-238.

(4)   Yamada, H.; Takada, S. *Prog. Theor. Phys.* **1973**, *49*, 1401-19.

(5)   Sechovsky, V.; Havela, L.; Nakotte, H.; Prokes, K.; Brueck, E.; de Boer, F. R. *Physica B* **1995**, *206 & 207*, 501-4.

(6)   Brabers, J. H. V. J.; Bakker, K.; Nakotte, H.; de Boer, F. R.; Lenczowski, S. K. J.; Buschow, K. H. J. *J. Alloys Compd.* **1993**, *199*, L1-L3.

(7)   Van Dover, R. B.; Gyorgy, E. M.; Cava, R. J.; Krajewski, J. J.; Felder, R. J.; Peck, W. F. *Phys. Rev. B: Condens. Matter* **1993**, *47*, 6134-7.

(8)   Williams, W. M.; Macaluso, R. T.; Moldovan, M.; Young, D. P.; Chan, J. Y. *Inorg. Chem.* **2003**, *42*, 7315-7318.

(9)   Ban, Z.; Sikirica, M. *Acta Cryst.* **1965**, *18*, 594-9.

(10)   Kim, S.-H.; Seo, D.-K.; Kremer, R. K.; Koehler, J.; Villesuzanne, A.; Whangbo, M.-H. *Chem. Mater.* **2005**, *17*, 6338-6341.

(11)   Cho, J.; Millican, J. N.; Capan, C.; Sokolov, D. A.; Moldovan, M.; Karki, A. B.; Young, D. P.; Aronson, M. C.; Chan, J. Y. *Chem. Mater.* **2007**, 20, 6116-6123.

(12)   Chen, X. Z.; Small, P.; Sportouch, S.; Zhuravleva, M.; Brazis, P.; Kannewurf, C. R.; Kanatzidis, M. G. *Chem. Mater.* **2000**, *12*, 2520-2522.

(13)   Pelleg, J.; Kimmel, G.; Dayan, D. *J. Less-Common Met.* **1981**, *81*, 33-44.

(14)   Manory, R.; Pelleg, J.; Grill, A. *J. Less-Common Met.* **1978**, *61*, 293-9.

(15)   Yatsenko, S. P.; Semyannikov, A. A.; Semenov, B. G.; Chuntonov, K. A. *J. Less-Common Met.* **1979**, *64*, 185-99.

(16)   Grin, Y. N.; Hiebl, K.; Rogl, P.; Noel, H. *J. Less-Common Met.* **1990**, *162*, 371-7.

(17)   Hulliger, F. *J. Alloys Compd.* **1995**, *218*, 255-8.

(18)   Hamaker, H. C.; Woolf, L. D.; MacKay, H. B.; Fisk, Z.; Maple, M. B. *Solid State Commun.* **1979**, *32*, 289-94.

(19)   Stewart, A. M. *Phys. Rev. B: Condens. Matter* **1993**, *47*, 11242-6.

CHAPTER 4. CRYSTAL GROWTH, STRUCTURE, AND PHYSICAL PROPERTIES OF *Ln*(Cu,Ga)$_{13}$ (*Ln* = La – Nd, Eu) AND THE DISCOVERY OF HEAVY-FERMION BEHAVIOR OF Pr(Cu,Ga)$_{13}$

4.1 Introduction

Intermetallic compounds adopting NaZn$_{13}$-type have been of great interest due to highly correlated behavior such as an enhanced electronic mass and superconductivity at low temperatures. UBe$_{13}$ has been reported as a heavy-fermion compound with the electronic specific-heat coefficient $\gamma \approx 1100$ mJmol^{-1}K^{-2} and shows an unconventional superconducting state mediated by *f*-electrons below 0.85 K.[1-6] Also, an enhanced $\gamma \approx 100$ mJmol^{-1}K^{-2} has been shown in CeBe$_{13}$.[4,7] Correlated electronic phenomena due to the 4*f*- or 5*f*-moments on the CeBe$_{13}$ and UBe$_{13}$ compounds are primarily due to its simple cubic symmetry.

Heavy-fermion behavior is associated with the valence instability of the 4*f*-electrons in Ce- or Yb-based compounds.[8-10] However, until recently, several Pr-based heavy-fermion compounds have been reported. Heavy-fermion behavior in Pr-based intermetallic compounds is quite exotic because it is well known that the localized 4*f*^{2}-electrons of Pr^{3+} ions are stable. The Heusler-type PrInAg$_2$ ($\gamma \approx 6500$ mJmol^{-1}K^{-2}) has been reported as the first Pr-based heavy-fermion compound and shows positive ln*T* temperature-dependent resistivity possibly related to the non Fermi liquid behavior of the ground state.[11-14] In contrast to PrInAg$_2$, PrFe$_4$P$_{12}$ shows T^2 temperature-dependent resistivity due to the Fermi liquid behavior in the heavy-fermion state with $\gamma \approx 1400$ mJmol^{-1}K^{-2} in the applied field of $\mu_0H = 6$ T, which satisfies the Kadowaki-Woods relation.[14-18] More interestingly, the first Pr-based heavy-fermion superconductor, PrOs$_4$Sb$_{12}$ orders at $T_c = 1.85$ K with $\gamma \approx 350$ mJmol^{-1}K^{-2}.[19-22]

On the exploration of the *Ln*-Cu-Ga system, the Sm$_2$NiGa$_{12}$-type[23] structure can be stabilized for early lanthanides in the Ga rich region with reaction ratios of 1.5:1:15 and 2:1:20.[24]

Ce_2CuGa_{12} is paramagnetic down to 2 K with an enhanced $\gamma \approx 67$ mJmol^{-1}K^{-2}.[24] When Cu concentration is increased, the $Ln(Cu,Ga)_{13}$-type can be synthesized for early lanthanides in Ln-Cu-Ga system. In this manuscript, we report the structure, magnetism, resistivity, and heat capacity of $Ln(Cu,Ga)_{13}$ (Ln = La-Nd, Eu). We also report the observation of heavy-fermion behavior in the compound $Pr(Cu,Ga)_{13}$.

4.2 Experimental

4.2.1 Synthesis

Single crystals of $Ln(Cu,Ga)_{13}$ (Ln = La-Nd, Eu) were successfully grown in excess Ga flux. Ln (Ln = La-Nd, Eu; chunks, 99.9 %, Alfa Aesar), Cu (powder, 99.999 %, Alfa Aesar), and Ga (pellets, 99.9999 %, Alfa Aesar) with a total weight of ca. 2.5 g were mixed in the ratio Ln:Cu:Ga = 1:5:20 and placed into an alumina crucible. The crucible and mixture were then sealed under vacuum in a fused silica tube and heated to 1373 K for 7 h. The tube was slowly cooled to 673 K at a rate of 10 K/h, before removing from the furnace. The excess molten flux was then removed from the silvery cubic crystals (Figure 4.1) by centrifugation, and the crystals were stable in air. A diluted HCl (1 M) solution was used to remove the remaining Ga flux on the surfaces of crystals. After etching crystals for several hours, silvery surfaces of crystals turned into reddish color, which indicates the reduction of Cu and the completion of removal of Ga flux on crystal surfaces. The reduced Cu was successfully removed by using a diluted HNO_3 (30 %) solution.

4.2.2 Single-Crystal X-ray Diffraction and Elemental Analysis

$\approx 0.03 \times 0.03 \times 0.03$ mm^3 fragments of $Ln(Cu,Ga)_{13}$ (Ln = La-Nd, Eu) were mounted onto a glass fiber using epoxy. Intensity data were collected on a Bruker Nonius KappaCCD single-crystal diffractometer equipped with MoK$_\alpha$ radiation ($\lambda = 0.71073$ Å) up to $\theta = 30.0°$ at
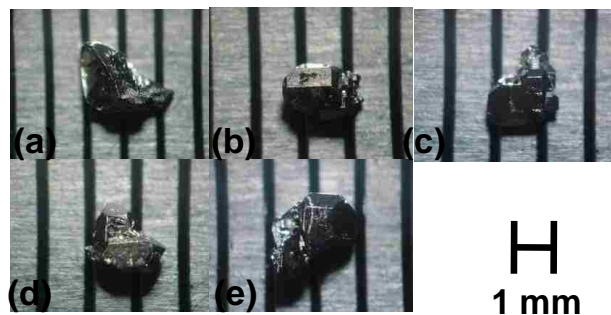
Figure 4.1 Single crystals of Ln(Cu,Ga)$_{13}$ (Ln = La–Nd, Eu) are shown. (a)–(e) correspond to the order for La–Nd, and Eu, respectively.

298 K by using Nonius SuperGUI software. Data reduction and integration were performed with the maXus package. Direct methods were used to solve the structure. SHELXL97 was used to refine the structural model of the Ln(Cu,Ga)$_{13}$ (Ln = La-Nd, Eu) compounds, and data were corrected with extinction coefficients and refined with anisotropic displacement parameters. Refinement with a fully occupied formula was converged with very small final difference residual peaks. Further crystallographic parameters for Ln(Cu,Ga)$_{13}$ (Ln = La-Nd, Eu) are provided in Table 4.1. Atomic positions and displacement parameters for Ln(Cu,Ga)$_{13}$ (Ln = La-Nd, Eu) are provided in Table 4.2, and selected interatomic distances are presented in Table 4.3. Single crystals of Ln(Cu,Ga)$_{13}$ (Ln = La-Nd, Eu) were analyzed with a JEOL JSM-5060 scanning electron microscope equipped with an energy dispersive spectrometer. The accelerating voltage was 15 kV with beam to sample distance of 20 mm. An average 5-7 scans were performed on each single crystal. The compositions normalized per lanthanide are provided in Table 4.4.

4.2.3 Physical Property Measurements

Magnetization data were obtained using a Quantum Design SQUID magnetometer. The temperature-dependent magnetization data were obtained under field cooled conditions from 2 K

Table 4.1 Crystallographic Data for Ln(Cu,Ga)$_{13}$ (Ln = La-Nd, Eu)

	La(Cu,Ga)$_{13}$	Ce(Cu,Ga)$_{13}$	Pr(Cu,Ga)$_{13}$	Nd(Cu,Ga)$_{13}$	Eu(Cu,Ga)$_{13}$
Crystal data					
Formula	La(Cu,Ga)$_{13}$	Ce(Cu,Ga)$_{13}$	Pr(Cu,Ga)$_{13}$	Nd(Cu,Ga)$_{13}$	Eu(Cu,Ga)$_{13}$
a (Å)	11.8490(9)	11.8240(7)	11.8110(10)	11.8030(7)	11.896(6)
V (Å^3)	1663.6(2)	1653.08(17)	1647.6(2)	1644.29(17)	1683.5(15)
Z	8	8	8	8	8
Crystal dimension (mm^3)	0.03×0.03× 0.03	0.05×0.05×0.05	0.03×0.03×0.03	0.03×0.03×0.03	0.05×0.05×0.05
Crystal system	Cubic	Cubic	Cubic	Cubic	Cubic
Space group	*Fm-3c*	*Fm-3c*	*Fm-3c*	*Fm-3c*	*Fm-3c*
θ range (°)	3.44-29.88	3.45-29.95	3.45-29.99	3.45-29.95	3.43-29.99
μ (mm^{-1})	40.870	41.734	41.921	42.906	45.825
Data collection					
Measured reflections	346	322	319	338	286
Independent reflections	123	123	123	120	123
Reflections with $I > 2\sigma(I)$	119	121	118	117	119
R_{int}	0.0231	0.0401	0.0318	0.0204	0.0292
h	-16→16	-16→16	-16→16	-16→16	-16→16
k	-10→10	-10→10	-10→10	-10→10	-10→10
l	-10→10	-10→10	-10→10	-10→10	-10→10
Refinement					
[a]$R_1[F^2 > 2\sigma(F^2)]$	0.0290	0.0299	0.0287	0.0211	0.0346
[b]$wR_2(F^2)$	0.0835	0.0831	0.0733	0.0574	0.1068
Reflections	123	123	123	120	123
Parameters	11	11	11	11	11
$\Delta\rho_{\text{max}}$ (eÅ^{-3})	3.136	2.216	2.295	1.953	4.131
$\Delta\rho_{\text{min}}$ (eÅ^{-3})	-3.989	-4.555	-3.009	-2.482	-4.303

[a]$R_1 = \sum||F_o| - |F_c||/\sum|F_o|$

[b]$wR_2 = [\sum[w(F_o^2 - F_c^2)]/\sum[w(F_o^2)^2]]^{1/2}$

Table 4.2 Atomic Positions and Thermal Parameters for $Ln(Cu,Ga)_{13}$ (Ln = La-Nd, Eu)

Atom	Wyckoff position	x	y	z	U_{eq} (Å^2)^a
La	8a	1/4	1/4	1/4	0.0059(6)
Cu	8b	0	0	0	0.0161(10)
M	96i	0	0.17800(9)	0.12145(9)	0.0112(6)
Ce	8a	1/4	1/4	1/4	0.0021(6)
Cu	8b	0	0	0	0.0112(9)
M	96i	0	0.17802(8)	0.12155(8)	0.0073(7)
Pr	8a	1/4	1/4	1/4	0.0037(6)
Cu	8b	0	0	0	0.0124(10)
M	96i	0	0.17829(9)	0.12168(9)	0.0077(6)
Nd	8a	1/4	1/4	1/4	0.0080(5)
Cu	8b	0	0	0	0.0157(8)
M	96i	0	0.17837(8)	0.12167(8)	0.0123(5)
Eu	8a	1/4	1/4	1/4	0.0083(7)
Cu	8b	0	0	0	0.0200(13)
M	96i	0	0.17811(11)	0.12117(11)	0.0123(8)

$^a U_{eq}$ is defined as one-third of the trace of the orthogonalized U_{ij} tensor.

Table 4.3 Selected Interatomic Distances (Å) for $Ln(Cu,Ga)_{13}$ (Ln = La-Nd, Eu)

Atoms	$La(Cu,Ga)_{13}$	$Ce(Cu,Ga)_{13}$	$Pr(Cu,Ga)_{13}$	$Nd(Cu,Ga)_{13}$	$Eu(Cu,Ga)_{13}$
Ln-M	3.4385(6)	3.4306(5)	3.4254(6)	3.4229(5)	3.4532(19)
Cu-M	2.5533(10)	2.5488(10)	2.5495(11)	2.5485(9)	2.5627(18)
M-M	2.4690(15)	2.4621(14)	2.4553(15)	2.4532(13)	2.482(2)
M-M	2.6397(11)	2.6348(11)	2.6357(12)	2.6349(10)	2.651(2)

Table 4.4 Composition as Obtained from Electron Probe Microanalysis

	$La(Cu,Ga)_{13}$	$Ce(Cu,Ga)_{13}$	$Pr(Cu,Ga)_{13}$	$Nd(Cu,Ga)_{13}$	$Eu(Cu,Ga)_{13}$
(Cu:Ga) composition	6.87(6):6.13(6)	6.90(7):6.10(7)	6.90(11):6.10(11)	6.83(15):6.17(15)	6.41(6):6.59(6)

to 300 K with an applied field 0.1 T. Field-dependent measurements were collected at 3 K for fields between 0 T and 9 T then swept from 9 T back to 0 T. The electrical resistivity data were measured by the standard four-probe AC technique using a Quantum Design Physical Property Measurement System.

4.3 Results and Discussion

4.3.1 Structure

(a)   (b)
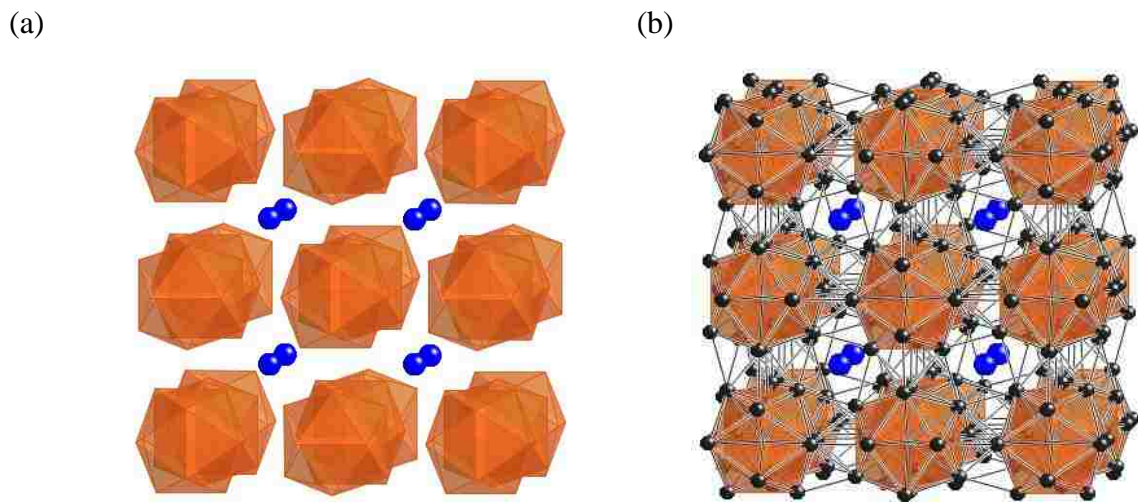
Figure 4.2 (a) The crystal structure of $Ce(Cu,Ga)_{13}$ is shown as Cu atom-centered icosahedral packing diagram, where the Ce atoms are represented with blue spheres. (b) The structural representation in terms of stella quadrangula.

$Ln(Cu,Ga)_{13}$ (Ln = La-Nd, Eu), adopting the $NaZn_{13}$ structure type, crystallize in the cubic $Fm\overline{3}c$ (No. 226) space group with Ln, Cu, M (M = Cu or Ga) occupying $8a$, $8b$, and $96i$, respectively. Figure 4.2a shows the Cu-centered M (M = Cu or Ga) icosahedra and Ce atoms occupying the cavities between icosahedra. However, this description might overlook the existence of interatomic distances between icosahedra. The interatomic distances between icosahedra are 2.463 Å and 2.651 Å, which are close to the ones within the icosahedron. Therefore, this structure can be described as Figure 4.2b including interconnections between

53

icosahedra, which are referred to as a three-dimensional network of stellae quadrangulae (tetracapped tetrahedra). The Ce atoms in the 8*a* Wyckoff site are coordinated by 24 neighbor atoms, which is known as snub cube. Three different representations of polyhedra such as the Ce-centered snub cube, Cu-centered icosahedra, and the stellae quadrangula are shown in Figure 4.3a-c. Although Cu and Ga are not distinguishable by X-ray diffraction, it seems reasonable to be Cu-centered icosahedra in these compounds. A similar case has been reported on $BaCu_5Al_8$ and $EuCu_{6.5}Al_{6.5}$ compounds, which show the three-dimentional $[Cu_xAl_{13-x}]$ network having mostly Cu atoms residing in the 8*b* site.[25]

(a)   (b)

(c)
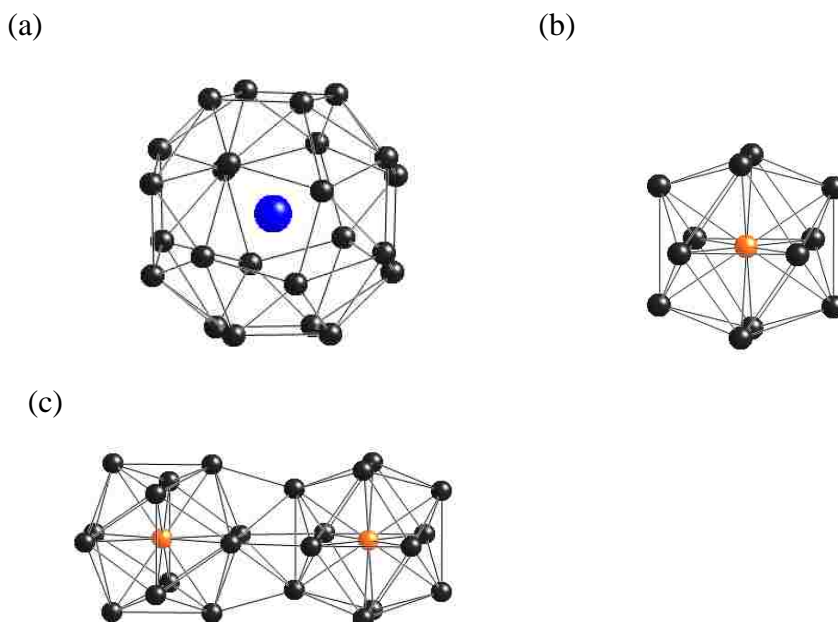
Figure 4.3 (a) Ce atom-centered snub cube, (b) Cu atom-centered icosahedrons, and (c) stella quadrangula.

The systematic study of the compositional variation and theoretical calculations in $BaCu_xAl_{13-x}$ suggest that the $NaZn_{13}$ structure type forms within a narrow range of the *x* between 5 and 6.[25]   Based on rigid-band calculations, Nordell and Miller claim that optimal intraicosahedral bonding on $BaCu_xAl_{13-x}$ has 40.5 electrons per formula unit, which corresponds

54

to simple electron counting by treating the valence s, p, and d electrons of the element at the $8b$ site, while counting only the valence s and p electrons of the elements at the $8a$ and $96i$ sites. Our elemental analyses on the Ln(Cu,Ga)$_{13}$ (Ln = La-Nd, Eu) compounds show a little bit higher Cu concentration than for the former work. It is probably due to the difference of electronegativity between Ga and Al although they have the same number of valence electrons. Although Nordell and Miller's electron counting method is not simply applicable to intermetallic system containing lanthanides, electron counting on our compounds based on their method seems reasonable.
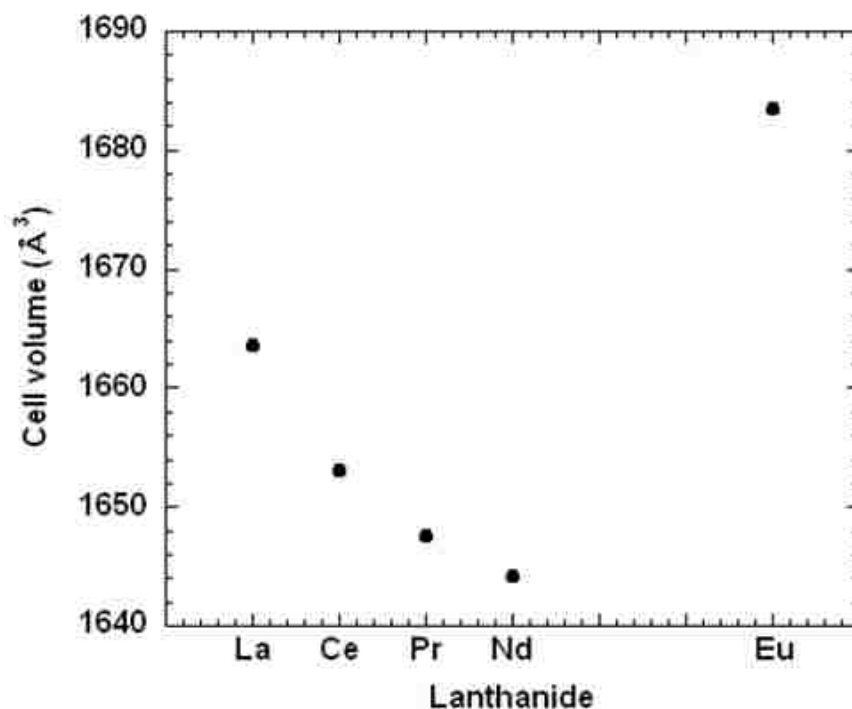
Figure 4.4 The unit cell volumes as a function of lanthanide are shown.

Figure 4.4 shows the unit cell volume of Ln(Cu,Ga)$_{13}$ (Ln = La-Nd, Eu) as a function of lanthanide. A decrease of the unit cell volume follows the lanthanide contraction except Eu(Cu,Ga)$_{13}$. A big increase in the unit cell volume indicates the divalent oxidation state of Eu

55

analogue. From our study of *Ln*-Cu-Ga system, we have observed that early lanthanides adopt to

NaZn$_{13}$ structure type and late lanthanides adopt to ThMn$_{12}$ structure type.

4.3.2 Physical Properties
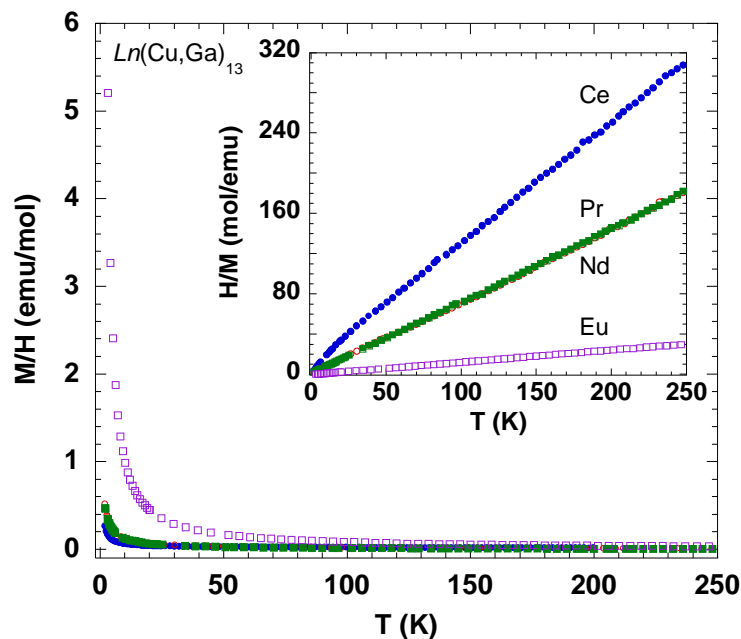
Figure 4.5   Magnetic susceptibility (emu/mol *Ln*) of *Ln*(Cu,Ga)$_{13}$ (*Ln* = Ce–Nd, Eu) as a function of temperature is shown.   The inset shows inverse magnetic susceptibility of *Ln*(Cu,Ga)$_{13}$ (*Ln* = Ce–Nd, Eu).

The temperature-dependent magnetic susceptibility of *Ln*(Cu,Ga)$_{13}$ (*Ln* = Ce-Nd, Eu) is

shown in Figure 4.5.   No long-range magnetic ordering is observed down to 2 K for all

compounds. The magnetic susceptibility data of *Ln*(Cu,Ga)$_{13}$ (*Ln* = Ce-Nd, Eu) were fitted to a

modified Curie-Weiss law in the following form: $\chi(T) = \chi_0 + C/(T - \theta)$, where χ_0 denotes the

temperature-independent term, *C* represents the Curie constant and θ is the Weiss temperature.

The effective moments of 2.36 μ_B/Ce, 3.32 μ_B/Pr and 3.40 μ_B/Nd are close to the calculated

values for Ce^{3+}, Pr^{3+}, and Nd^{3+}, respectively. The negative Weiss temperatures of − 3.83 (Ce–),

− 1.27 (Pr–), and − 1.80 (Nd–) are indicative of antiferromagnetic correlations in these

56

compounds. The effective moment of 8.06 μ_B/Eu with $\theta = 1.85$ in the Eu analogue indicates that Eu ion is in the divalent state. This is consistent with the result of cell volume as a function of lanthanides. The positive sign of the Weiss temperature for Eu analogue is indicative of ferromagnetic coupling in contrast to the three other analogues. The small Weiss temperatures for all compounds suggest that the lanthanide moments are very weakly coupled in this system, which is consistent with the large *Ln-Ln* separation of $\approx$ 5.9 Å. A summary of the magnetic properties of *Ln*(Cu,Ga)$_{13}$ (*Ln* = Ce-Nd, Eu) is shown in Table 4.5.

Table 4.5 Magnetic Properties of *Ln*(Cu,Ga)$_{13}$ (*Ln* = Ce-Nd, Eu)

	C	θ (K)	χ_0 ($\times$ 10^{-4})	μ_{calc} (μ_B)	μ_{eff} (μ_B)	Fit range (K)
Ce(Cu,Ga)$_{13}$	0.70	-3.83	6.49	2.54 (Ce^{3+})	2.36	10-300
Pr(Cu,Ga)$_{13}$	1.38	-1.27	1.92	3.58 (Pr^{3+})	3.32	10-300
Nd(Cu,Ga)$_{13}$	1.45	-1.80	-2.84	3.62 (Nd^{3+})	3.40	10-300
Eu(Cu,Ga)$_{13}$	8.14	1.85	4.27	7.94 (Eu^{2+})	8.06	10-260

Figure 4.6 shows the field-dependent isothermal magnetization of *Ln*(Cu,Ga)$_{13}$ (*Ln* = Ce-Nd, Eu) measured at constant temperature of 3 K. The magnetization at 5 T is only about 0.89 μ_B, 1.42 μ_B, and 1.51 μ_B for Ce, Pr, and Nd analogue, respectively, which is much smaller than the calculated value of 2.14 μ_B, 3.20 μ_B, and 3.27 μ_B for each *Ln*$^{3+}$ ion and is probably due to the crystal field splitting of *Ln*$^{3+}$ in its cubic environment. This result suggests a local moment for these ions is not linear but shows a saturating behavior. However, for Eu compound the magnetization saturates at 5 T with a value of 6.85 μ_B close to the expected value of 7.0 μ_B for Eu^{2+} ion.

The temperature dependence of the electrical resistivity of $Ln(Cu,Ga)_{13}$ (Ln = La-Nd, Eu), where each compound shows metallic behavior with RRR (residual resistivity ratio) values of 2.3, 1.6, 4.1, 2.4, and 1.4 for La, Ce, Pr, Nd, and Eu analogue, respectively, is shown in Figure 4.7. Unlike other analogues, a broad shoulder for $Pr(Cu,Ga)_{13}$, which may indicate Kondo coherence, is observed in the resistivity below 60 K. In the inset of Figure 4.7, ρ–ρ_0 are plotted as a function of T^2 for $Pr(Cu,Ga)_{13}$ at low temperatures, which is suggestive of a Fermi liquid behavior. The T^2 coefficient A of 0.0727 $\mu\Omega$-cm and the residual resistivity of 79.909 $\mu\Omega$-cm/K^2 were obtained
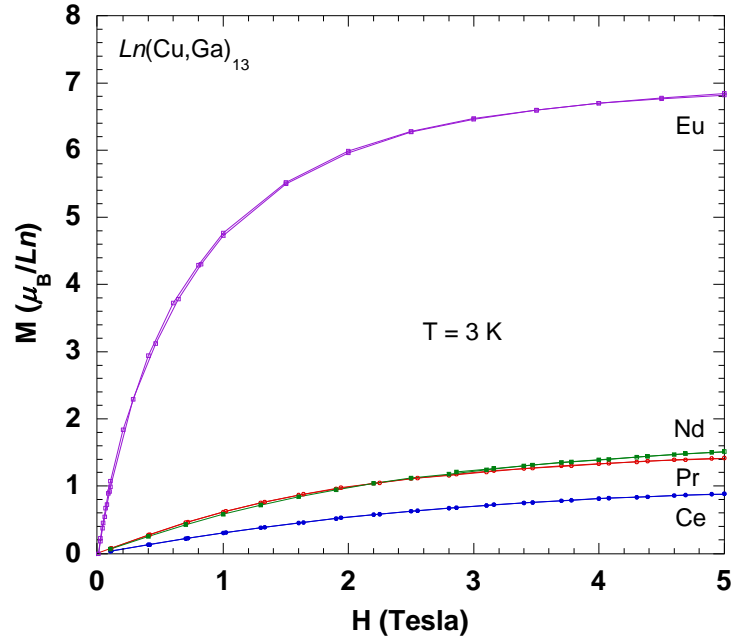
Figure 4.6 Magnetization of $Ln(Cu,Ga)_{13}$ (Ln = Ce-Nd, Eu) as a function of magnetic field at 3K is shown.

by fitting the data at low temperatures ($\leq$ 20 K).

Figure 4.8 shows the magnetoresistance (MR % = $(\rho_H - \rho_0)/\rho_0 \times 100$) of single crystals of $Ln(Cu,Ga)_{13}$ (Ln = La-Nd, Eu) as a function of field at 3 K. The $Ln(Cu,Ga)_{13}$ (Ln = La-Nd)
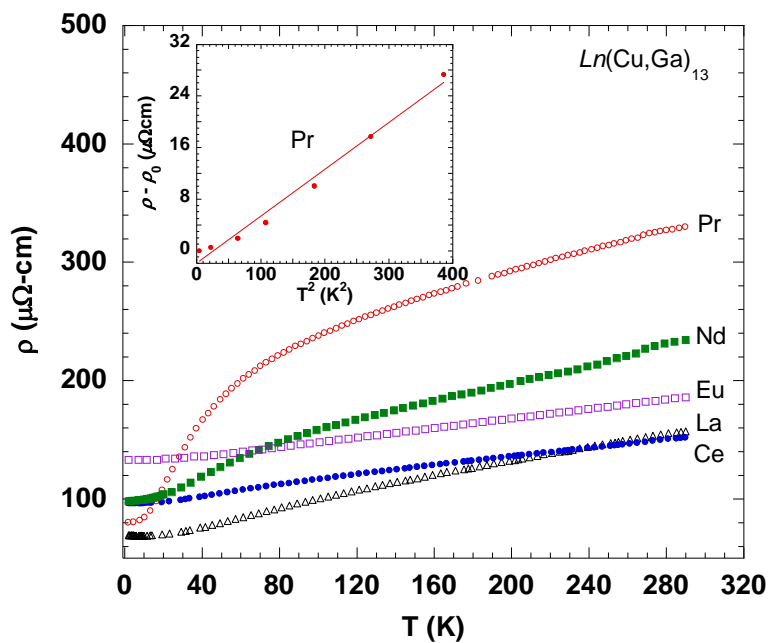
Figure 4.7 Normalized electrical resistivity of Ln(Cu,Ga)$_{13}$ (Ln = La-Nd, Eu) as a function of temperature is shown.
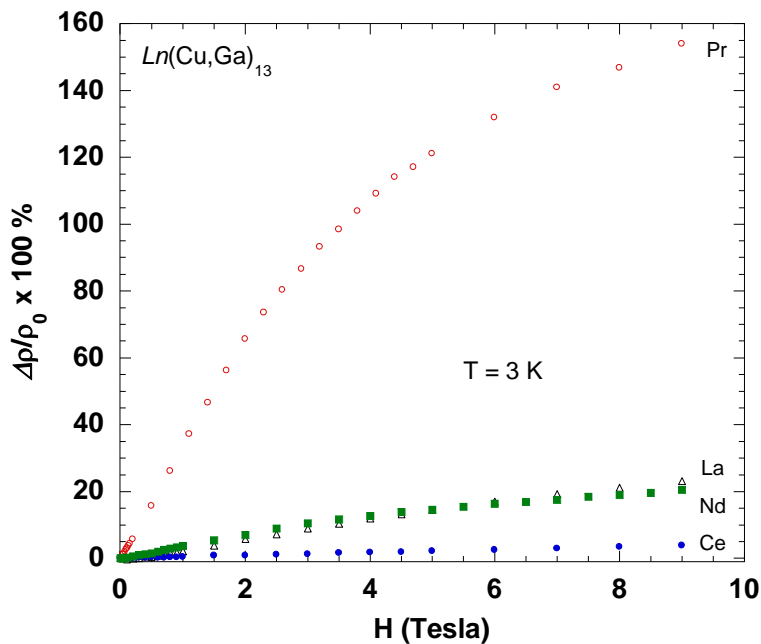
Figure 4.8 MR % of Ln(Cu,Ga)$_{13}$ (Ln = La-Nd) as a function of field at 3 K is shown.

compounds except Eu analogue show positive magnetoresistance, with ratios up to 23 %, 3 %, 154 %, and 20 % at 9 T for La, Ce, Pr, and Nd analogue, respectively. Interestingly, Pr(Cu,Ga)$_{13}$ shows much more field-dependent resistance than other analogues in this series. This is probably related to the resistivity behavior caused by Kondo coherence at low temperatures.
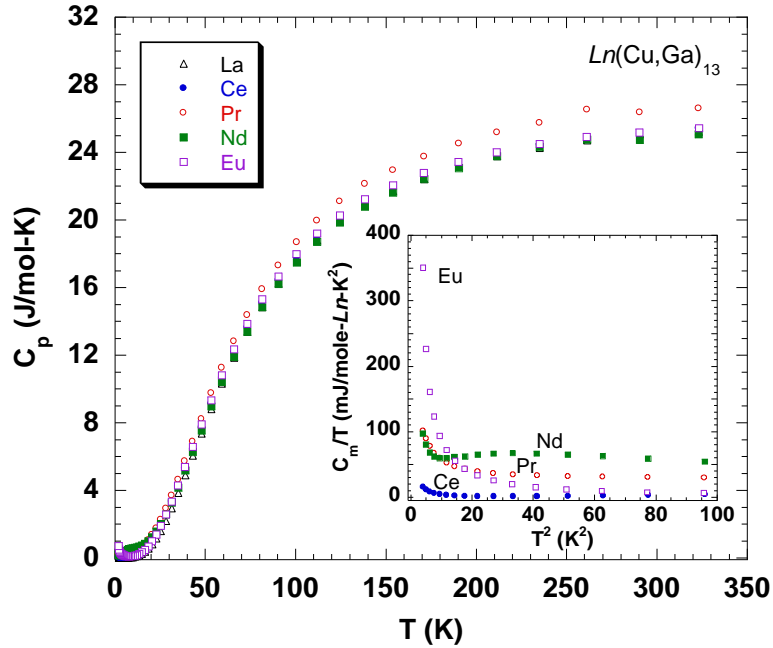
Figure 4.9 Specific heat of Ln(Cu,Ga)$_{13}$ (Ln = La-Nd) as a function of temperature. The inset shows C_m/T versus T^2 for Ln(Cu,Ga)$_{13}$ (Ln = Ce-Nd) after subtracting lattice contribution.

The specific heat of Ln(Cu,Ga)$_{13}$ (Ln = La-Nd) is shown in Figure 4.9. There is no indication of a magnetic ordering down to 2 K for Ln(Cu,Ga)$_{13}$ (Ln = Ce-Nd), consistent with their magnetic susceptibility data. As shown in the inset of Figure 4.9, after subtracting the phonon contribution to heat capacity $\gamma \approx 16$ mJmol^{-1}K^{-2}, 100 mJmol^{-1}K^{-2}, 97 mJmol^{-1}K^{-2}, 350 mJmol^{-1}K^{-2} are obtained for Ce, Pr, Nd, and Eu analogue, respectively, which indicates that Ln(Cu,Ga)$_{13}$ (Ln = Ce-Nd) exhibit an enhanced heavy-fermion behavior except Ce analogue.

Taken into account the resistivity and specific heat data of Pr(Cu,Ga)$_{13}$ together, the Kadowaki-Woods ratio: A/γ^2, where A represents the coefficient of the quadratic term in the temperature dependence of the resistivity and γ is the coefficient of the linear term in the temperature dependence of the specific heat, of $\approx 0.727 \times 10^{-5}$ is obtained and close to what one would expect for heavy-fermion behavior. As mentioned earlier, there have been only rare Pr-based heavy-fermion intermetallic compounds such as PrInAg$_2$ and the filled skutterudites PrM_4X_{12} (M = Fe, Ru, Os; X = P, As, Sb). Our preliminary interpretation on Pr(Cu,Ga)$_{13}$ satisfying the Kadowaki-Woods ratio is similar to the case of PrFe$_4$P$_{12}$ which has been reported as the only $4f^2$-based Fermi liquid heavy-fermion compound.[14-16,26,27] However, further work at low temperatures is needed to establish the origin of heavy-fermion behavior on Pr(Cu,Ga)$_{13}$ compound.

4.4 References

(1)   Ott, H. R.; Rudigier, H.; Fisk, Z.; Smith, J. L. *Phys. Rev. Lett.* **1983**, *50*, 1595-1598.

(2)   Smith, J. L.; Fisk, Z.; Willis, J. O.; Batlogg, B.; Ott, H. R. *J. Appl. Phys.* **1984**, *55*, 1996-2000.

(3)   Maple, M. B.; Chen, J. W.; Lambert, S. E.; Fisk, Z.; Smith, J. L.; Ott, H. R.; Brooks, J. S.; Naughton, M. J. *Phys. Rev. Lett.* **1985**, *54*, 477-480.

(4)   Cox, D. L. *Phys. Rev. B: Condens. Matter* **1987**, *35*, 6504-6516.

(5)   Reinders, P. H. P.; Wand, B.; Steglich, F.; Fraunberger, G.; Stewart, G. R.; Andrian, G. *Europhys. Lett.* **1994**, *25*, 619-624.

(6)   Kim, J. S.; Stewart, G. R. *Phys. Rev. B: Condens. Matter* **1995**, *51*, 16190-16193.

(7)   Wilson, Z. S.; Macaluso, R. T.; Bauer, E. D.; Smith, J. L.; Thompson, J. D.; Fisk, Z.; Stanley, G. G.; Chan, J. Y. *J. Am. Chem. Soc.* **2004**, *126*, 13926-13927.

(8)   Holmes, A. T.; Jaccard, D.; Miyake, K. *J. Phys. Soc. Jpn.* **2007**, *76*, 051002/1-051002/10.

(9)   Steglich, F. *J. Phys. Soc. Jpn.* **2005**, *74*, 167-177.

(10)   Miyake, K.; Narikiyo, O.; Onishi, Y. *Physica B* **1999**, *259-261*, 676-677.

(11)   Yatskar, A.; Beyermann, W. P.; Movshovich, R.; Canfield, P. C. *Phys. Rev. Lett.* **1996**, *77*, 3637-3640.

(12)   Yatskar, A.; Beyermann, W. P.; Movshovich, R.; Canfield, P. C.; Panchula, A.; Bud'ko, S. L. *Physica B* **1997**, *230-232*, 46-48.

(13)   Mitamura, H.; Takeshita, N.; Uwatoko, Y.; Mori, H.; Yamaguchi, A.; Tomita, T.; Wada, H.; Mori, N.; Ishimoto, H.; Goto, T. *Physica B* **2000**, *281&282*, 150-151.

(14)   Matsuda, T. D.; Okada, H.; Sugawara, H.; Aoki, Y.; Sato, H.; Andreev, A. V.; Shiokawa, Y.; Sechovsky, V.; Honma, T.; Yamamoto, E.; Onuki, Y. *Physica B* **2000**, *281&282*, 220-222.

(15)   Sugawara, H.; Matsuda, T. D.; Abe, K.; Aoki, Y.; Sato, H.; Nojiri, S.; Inada, Y.; Settai, R.; Onuki, Y. *J. Magn. Magn. Mater.* **2001**, *226-230*, 48-50.

(16)   Aoki, Y.; Namiki, T.; Matsuda, T. D.; Sugawara, H.; Sato, H. *Physica B* **2002**, *312&313*, 823-824.

(17)   Kadowaki, K.; Woods, S. B. *Solid State Commun.* **1986**, *58*, 507-509.

(18)   Miyake, K.; Matsuura, T.; Varma, C. M. *Solid State Commun.* **1989**, *71*, 1149-1153.

(19)   Bauer, E. D.; Frederick, N. A.; Ho, P. C.; Zapf, V. S.; Maple, M. B. *Phys. Rev. B: Condens. Matter* **2002**, *65*, 100506/1-100506/4.

(20)   Sugawara, H.; Osaki, S.; Saha, S. R.; Aoki, Y.; Sato, H.; Inada, Y.; Shishido, H.; Settai, R.; Onuki, Y.; Harima, H.; Oikawa, K. *Phys. Rev. B: Condens. Matter* **2002**, *66*, 220504/1-220504/4.

(21)   Aoki, Y.; Tsuchiya, A.; Kanayama, T.; Saha, S. R.; Sugawara, H.; Sato, H.; Higemoto, W.; Koda, A.; Ohishi, K.; Nishiyama, K.; Kadono, R. *Phys. Rev. Lett.* **2003**, *91*, 067003/1-067003/4.

(22)   Izawa, K.; Nakajima, Y.; Goryo, J.; Matsuda, Y.; Osaki, S.; Sugawara, H.; Sato, H.; Thalmeier, P.; Maki, K. *Phys. Rev. Lett.* **2003**, *90*, 117001/1-117001/4.

(23)   Chen, X. Z.; Small, P.; Sportouch, S.; Zhuravleva, M.; Brazis, P.; Kannewurf, C. R.; Kanatzidis, M. G. *Chem. Mater.* **2000**, *12*, 2520-2522.

(24)   Cho, J. Y.; Millican, J. N.; Capan, C.; Sokolov, D. A.; Moldovan, M.; Karki, A. B.; Young, D. P.; Aronson, M. C.; Chan, J. Y. *Chem. Mater.* **2008**, 20, 6116-6123.

(25)   Nordell, K. J.; Miller, G. J. *Inorg. Chem.* **1999**, *38*, 579-590.

(26)   Aoki, Y.; Namiki, T.; Matsuda, T. D.; Abe, K.; Sugawara, H.; Sato, H. *Phys. Rev. B: Condens. Matter* **2002**, *65*, 064446/1-064446/7.

(27)   Aoki, Y.; Sugawara, H.; Sato, H. *J. Alloys Compd.* **2006**, *408-412*, 21-26.

CHAPTER 5. CRYSTAL GROWTH, STRUCTURE, AND PHYSICAL PROPERTIES OF SmCu$_4$Ga$_8$[*]

5.1 Introduction

Sm-containing intermetallic compounds have attracted much attention because of the valence fluctuation between the trivalent and divalent Sm ion[1-4] and the Van Vleck paramagnetism, due to a relatively closely spaced crystal field ground state $^6H_{5/2}$ and 1st excited state $^6H_{7/2}$.[5,6] As a result, a modified Curie-Weiss law is observed in several Sm-based compounds: SmPdIn$_2$ with the HfNiGa$_2$ structure type has an antiferromagnetic transition and a spin reorientation at 9.0 K and 5.5 K, respectively. The inverse molar magnetic susceptibility is non-linear.[7] This has also been reported for Sm$_3$Co$_6$Sn$_5$,[8] SmPtIn,[9] SmCuGa$_3$,[10] and Sm$_3$InSe$_6$.[11] Layered ThCr$_2$Si$_2$[12] structure type compounds, SmPd$_2$Ga$_2$[13] and SmMn$_2$Ge$_2$[14,15] show large magnetoresistance up to 49 % and 100 % at 9 T, respectively, which is also an unusual behavior for most intermetallic compounds.

Ternary compounds of the Sm-Cu-Ga system adopting NaZn$_{13}$, ThZn$_{12}$, BaCd$_{11}$, BaAl$_4$, SmZn$_{11}$, and Th$_2$Zn$_{17}$ have been explored by V. Ya. Markiv *et al*. at 500 °C isotherm.[16] SmCu$_{4.1}$Ga$_{6.9}$,[16] which is isostructural to SmZn$_{11}$,[17] shows disorder in its structure. Our ongoing exploration of the Sm-Cu-Ga ternary system using Ga flux has led us to grow single crystals of SmCu$_4$Ga$_8$, which is isostructural to EuAg$_4$In$_8$.[18] Here, we report the single crystal structure of SmCu$_4$Ga$_8$ and compare to the disordered structure, SmCu$_{4.1}$Ga$_{6.9}$. We present magnetism, resistivity, and magnetoresistance of SmCu$_4$Ga$_8$.

5.2 Experimental

5.2.1 Synthesis

Single crystals of $SmCu_4Ga_8$ were grown in excess Ga flux. Sm (3N, Alfa Aesar) chunk, Cu powder (5N, Alfa Aesar), and Ga (6N, Alfa Aesar) were placed into an alumina crucible in a 1:5:20 stoichiometric ratio. The crucible and its contents were then sealed in an evacuated fused silica tube and heated up to 1373 K for 7 h. After fast cooling to 773 K at a rate of 150 K/h, the tube was then slowly cooled to 673 K at a rate of 8 K/h and immediately inverted and spun with a centrifuge for the removal of excess Ga flux. Silver-colored hexagon-like crystals (Figure 5.1)

1 mm
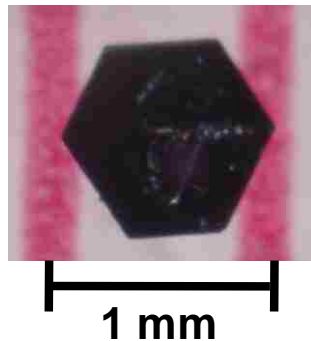
Figure 5.1 A single crystal of $SmCu_4Ga_8$.

were found and not observed to degrade in air. To ensure the complete removal of Ga on surfaces, crystals were etched using a diluted HCl (1 M) solution.

5.2.2 Single-Crystal X-ray Diffraction and Elemental Analysis

A $0.025 \times 0.025 \times 0.025$ mm^3 silver-colored fragment of $SmCu_4Ga_8$ was mounted onto the goniometer of a Nonius KappaCCD diffractometer equipped with MoK$_\alpha$ radiation ($\lambda = 0.71073$ Å). Data collection was carried out up to $\theta = 30.0°$ at 298 K. Further crystallographic parameters for $SmCu_4Ga_8$ are provided in Table 5.1. Direct methods were used to solve the structure. SHELXL97 was used to refine the structural model of the $SmCu_4Ga_8$ compound, and

data were corrected with extinction coefficients and refined with anisotropic displacement parameters. The obtained structural model was compared to the crystallographic data of $SmZn_{11}$.[17]

Table 5.1 Crystallographic Parameters for $SmCu_4Ga_8$

Crystal data	
Formula	$SmCu_4Ga_8$
a (Å)	8.865(2)
c (Å)	8.607(2)
V (Å^3)	585.8(2)
Z	3
Crystal dimension (mm^3)	0.03×0.03×0.03
Crystal system	Hexagonal
Space group	*P6/mmm*
θ range (°)	2.65-29.98
μ (mm^{-1})	45.027
Data collection	
Measured reflections	2187
Independent reflections	393
Reflections with $I>2\sigma(I)$	369
R_{int}	0.0546
h	-12→12
k	-10→10
l	-12→12
Refinement	
[a]$R_1[F^2>2\sigma(F^2)]$	0.0275
[b]$wR_2(F^2)$	0.0606
Reflections	393
Parameters	30
$\Delta\rho_{max}$ (e Å^{-3})	2.520
$\Delta\rho_{min}$ (e Å^{-3})	-1.944
Extinction coefficient	0.0126(5)

[a]$R_1 = \sum ||F_o|-|F_c||/\sum |F_o|$
[b]$wR_2 = [\sum[w(F_o^2 - F_c^2)]/\sum[w(F_o^2)^2]]^{1/2}$ $w = 1/[\sigma^2(F_o^2) + (0.0095\,P)^2 + 5.2687\,P]$
,

Table 5.2 Atomic Positions and Thermal Parameters for $SmCu_4Ga_8$

Wyckoff Positions	$SmCu_4Ga_8$ Atom	x	y	z	Occ.	U_{eq} (Å²)[a]	$SmZn_{11}$* Atom	x	y	z	Occ.
1*a*	Sm1	0	0	0	1	0.0037(2)	Sm1	0	0	0	1
2*d*	Sm2	1/3	2/3	1/2	1	0.0044(2)	Sm2	1/3	2/3	1/2	1
2*c*	-	-	-	-	-	-	Sm3	1/3	2/3	0	0.15
1*b*	-	-	-	-	-	-	Sm4	0.04	0	0	0.04
12*o*	Cu	0.16742(4)	2*x*	0.24233(7)	1	0.0077(2)	Zn1	0.1671(2)	2*x*	0.2415(3)	1
6*j*	Ga4	0.34835(11)	0	0	1	0.0097(3)	Zn2	0.3552(6)	0	0	1
6*k*	Ga5	0.29790(4)	0	1/2	1	0.0124(3)	Zn3	0.2944(5)	0	1/2	1
6*i*	Ga3	1/2	0	0.27241(12)	1	0.0123(3)	Zn4	1/2	0	0.2742(5)	1
2*e*	Ga1	0	0	0.34559(18)	1	0.0076(3)	Zn5	0	0	0.3544(8)	0.96
4*h*	Ga2	1/3	2/3	0.14734(13)	1	0.0099(3)	Zn6	1/3	2/3	0.1457(7)	0.85

[a]U_{eq} is defined as one-third of the trace of the orthogonalized U_{ij} tensor.

Occ.- Occupancy

* obtained from Reference 17. Model refined from powder X-ray diffraction data.

Table 5.3 Selected Interatomic Distances (Å) for $SmCu_4Ga_8$

	$SmCu_4Ga_8$
Sm1 environment	
Sm1-Cu(×12)	3.3104(9)
Sm1-Ga1(×2)	2.9745(17)
Sm1-Ga4(×6)	3.0881(12)
Sm2 environment	
Sm2-Cu(×6)	3.416
Sm2-Ga2(×2)	3.0353(13)
Sm2-Ga3(×6)	3.2228(8)
Sm2-Ga5(×6)	3.1239(10)
Ga1-Cu1(×6)	2.7199(10)
Ga1-Ga1(×1)	2.658(3)
Ga1-Ga2(×6)	2.9564(14)
Ga2-Cu1(×4)	2.5966(7)
Ga2-Ga2(×2)	2.6409(14)
Ga2-Ga5(×2)	2.6546(12)
Ga3-Cu1(×3)	2.6755(9)
Ga3-Ga3(×1)	2.536(2)
Ga3-Ga5(×3)	2.7763(8)
Ga4-Cu1(×4)	2.5971(7)
Ga4-Ga4(×1)	2.689(2)
Ga4-Ga5(×2)	2.7027(11)
Ga5-Cu1(×4)	2.5664(7)

Atomic positions and displacement parameters for $SmCu_4Ga_8$ are provided in Table 5.2, and selected interatomic distances are presented in Table 5.3. To confirm the stoichiometry of $SmCu_4Ga_8$, ICP-OES experiment was performed with a Perkin Elmer Optima Model 5300V at Galbraith Laboratories, Inc. and yielded an elemental ratio of 1:5.4:6.6 for Sm:Cu:Ga. This result suggests that it is possible for Cu to occupy some other crystallographic sites with Ga atoms. After considering of elemental analysis result, the structure of $SmCu_4Ga_8$ was carefully checked for a mixed occupancy on all of Cu and Ga sites. Cu atoms could be positioned in 6*i*, 6*k*, and 12*o* sites with statistical occupation of 2.69Cu + 3.31Ga, 2.22Cu + 3.78Ga, and 10.66Cu + 1.34Ga, respectively. This structural model gave the stoichiometry of 1:5.19:6.81 for Sm:Cu:Ga, which is close to the result of elemental analysis. However, Cu and Ga could not be distinguishable by X-ray diffraction and therefore, for simplicity, we report the stoichiometry of this compound as $SmCu_4Ga_8$ from final structural model without mixed occupancy.

5.2.3 Physical Property Measurements

Magnetization data were obtained using a Quantum Design SQUID magnetometer. The temperature-dependent magnetization data were obtained under field cooled conditions from 2 K to 300 K with an applied field 0.1 T. Field-dependent measurements were collected at 3 K for fields between 0 T and 9 T. The electrical resistivity data were measured by the standard four-probe AC technique using a Quantum Design Physical Property Measurement System.

5.3 Results and Discussion

5.3.1 Structure

The structure of $SmCu_4Ga_8$ is shown in Figure 5.2. $SmCu_4Ga_8$ is related to the disordered phase of $SmZn_{11}$[17] and isostructural to $EuAg_4In_8$.[18] $SmCu_4Ga_8$ crystallizes in the hexagonal *P*6/*mmm* space group (No. 191) with Sm1, Sm2, Ga1, Ga2, Ga3, Ga4, Ga5, and Cu

occupying the 1*a*, 2*d*, 2*e*,4*h*, 6*i*, 6*j*, 6*k*, and 12*o* Wyckoff sites, respectively. The crystal structure

consists of two crystallographic Sm environments which are corner-sharing to each other.
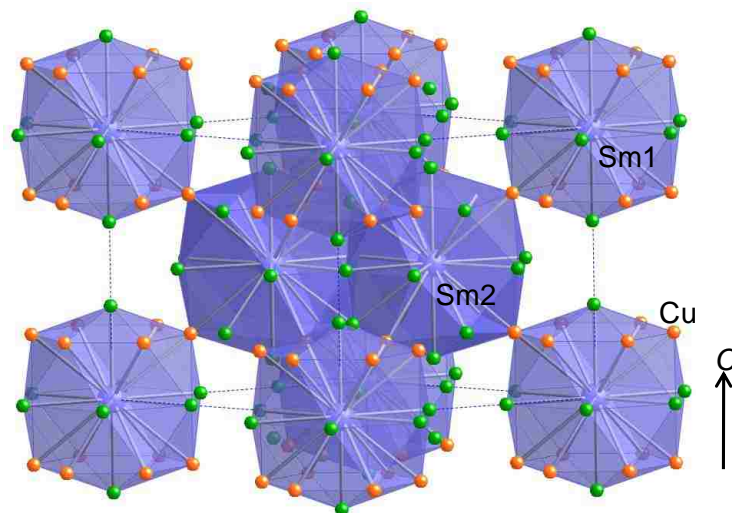
Figure 5.2 The crystal structure of $SmCu_4Ga_8$ is shown, where the Sm atoms are represented with blue spheres; the Cu atoms are denoted as orange spheres; and the Ga atoms are denoted with green spheres. Dashed lines are used to show the unit cell.

Sm1 is surrounded by 12 Cu, 2 Ga1, and 6 Ga4 atoms using a cutoff of 3.42 Å as shown

in Figure 5.3 (a). The Sm1 atom surrounded by six Ga4 atoms in the basal plane has a six-

membered Cu ring above and below the basal plane and the Cu rings are capped by two Ga1

atoms. The interatomic distances for Sm1-Cu, Sm1-Ga1, and Sm1-Ga4 are listed in Table 6.3,

with interatomic distances ranging from 2.9745(15) Å to 3.3104(7) Å and agree with those in

Sm1 environment for $SmCu_{4.1}Ga_{6.9}$. The Sm2 atom also has 20 neighbors consisting of 6 Cu, 6

Ga2, 2 Ga3, and 6 Ga5 atoms (Figure 5.3 (b)). Similar to the Sm1 environment, the Sm2 atom

capped by two Ga3 atoms along the *c*-axis has a six-membered basal ring of Ga2 and two

puckered six-membered rings composed of Cu and Ga5 above and below the basal plane. The

interatomic distances of 3.0353(11) Å from to 3.416 Å for Sm2-Cu, Sm2-Ga2, Sm2-Ga3, and

Sm2-Ga5 are also in good agreement with those in Sm2 polyhedra of $SmCu_{4.1}Ga_{6.9}$.[16]

69

A disorder was found for the $SmZn_{11}$ structure type[17] based on the observation of electron density in the difference Fourier synthesis of $SmZn_{11}$. Both $1b$ and $2c$ sites are positioned halfway along the c-axis between the $2e$ and $4h$ sites. Similar to the $SmZn_{11}$ disordered structure, $SmCu_{4.1}Ga_{6.9}$[16] has also been reported as a disordered phase. However, there was no indication
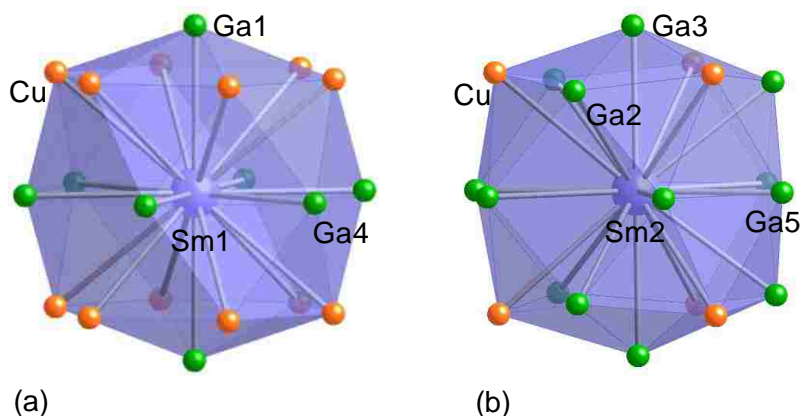
Figure 5.3 The local (a) Sm1 and (b) Sm2 environments are shown.

of a disordered phase from our observation of the difference Fourier synthesis in our compound. During refinement, all Wyckoff positions were treated anisotropically and fully occupied. The reliable factor (R_1) and maximum residual density of 0.0275 and 2.520, respectively, confirm that this structure does not have a disorder.

$SmCu_4Ga_8$ is related to $SmCu_5$,[19,20] which belongs to the hexagonal $CaCu_5$ type,[21,22] by these factors: $aSmCu_4Ga_8 \approx \sqrt{3}aSmCu_5$; $cSmCu_4Ga_8 \approx 2cSmCu_5$. When Sm atoms are replaced by pairs of Cu atoms in specific Wyckoff sites in the parental $SmCu_5$ structure type, various structure types such as $ThMn_{12}$, Th_2Fe_{17}, Th_2Ni_{17}, Th_2Zn_{17}, and U_2Zn_{17} are formed.[23] This structural relationship can be described easily through the ab projection and atomic arrangement of the $SmCu_4Ga_8$ structure as shown in Figure 5.4 (a)-(c). The $SmCu_5$ structure has two different layers which are alternating along the c-axis. One is a six-membered ring layer bearing the Sm

atoms in the center of hexagons. Another layer can be described as a Kagomé layer composed of Cu atoms. Within the $SmCu_4Ga_8$ structure unlike $SmCu_5$, the Kagomé layer-like hexagons are puckered by incorporation of Ga3 atoms between two different layers accompanying the systematic loss of Sm atoms.
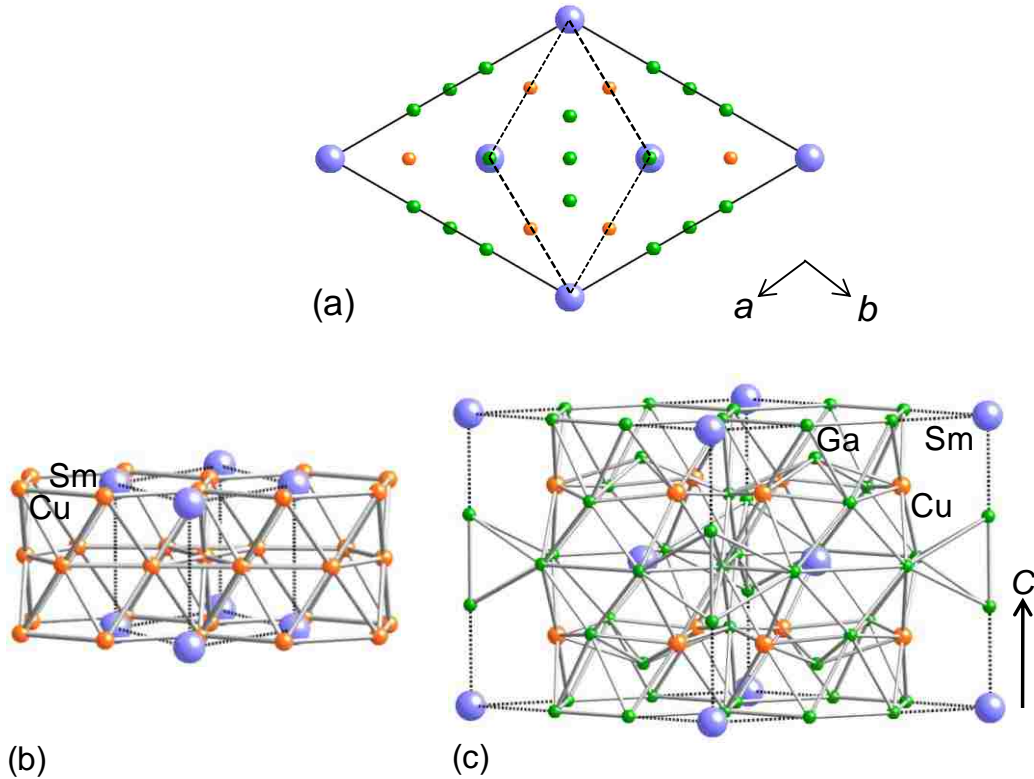
Figure 5.4 The (a) *ab* projection and atomic arrangement of (b) $SmCu_5$ and (c) $SmCu_4Ga_8$ are shown, where the Sm, Cu, and Ga atoms are represented with blue, orange, and green spheres, respectively. The dashed and solid lines represent the unit cell of $SmCu_5$ and $SmCu_4Ga_8$, respectively.

5.3.2 Physical Properties

Magnetic susceptibility of $SmCu_4Ga_8$ as a function of temperature at an external field of 1 Tesla is shown in Figure 5.5. The data of $SmCu_4Ga_8$ show a clear drop at 3.3 K which is indicative of an antiferromagnetic transition. From the inverse magnetic susceptibility plots of

71

SmCu$_4$Ga$_8$, a curvilinear behavior in the paramagnetic region is observed (not shown), which is usually found for Sm-intermetallics, resulting from an unusual electronic structure of the Sm^{3+} ion between the $J = 5/2$ ground state and $J = 7/2$ excited multiplet state.[4,5,8,9,24-27] A modified Curie-Weiss equation; $\chi (T) = \chi_0 + C/(T - \theta)$ was used to obtain the magnetic moment for the Sm^{3+} ion, where χ_0 represents the temperature-independent Van Vleck term, C is the Curie constant, and θ is the Weiss temperature. The inverse modified magnetic susceptibility is fitted from 10 K to 300 K and is shown in the inset of Figure 6.5. From this fit, the effective moment of 1.75 μ_B/Sm ion is obtained. The large negative Weiss value of -31.9 suggests strong antiferromagnetic correlations.
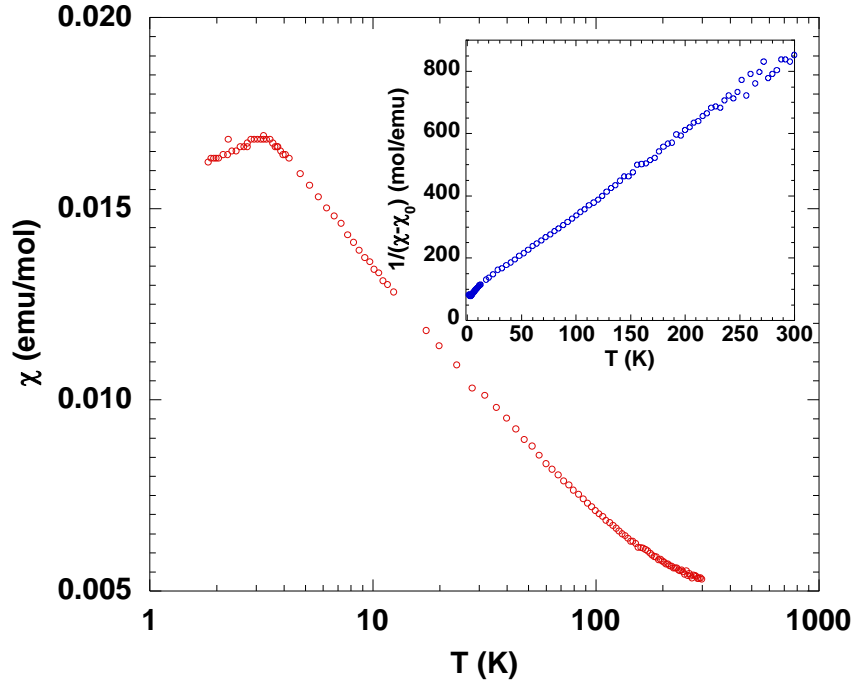
Figure 5.5 Magnetic susceptibility (emu/mol Sm) of SmCu$_4$Ga$_8$ as a function of temperature is shown. The inset shows the inverse magnetic susceptibility from the modified Curie-Weiss law.
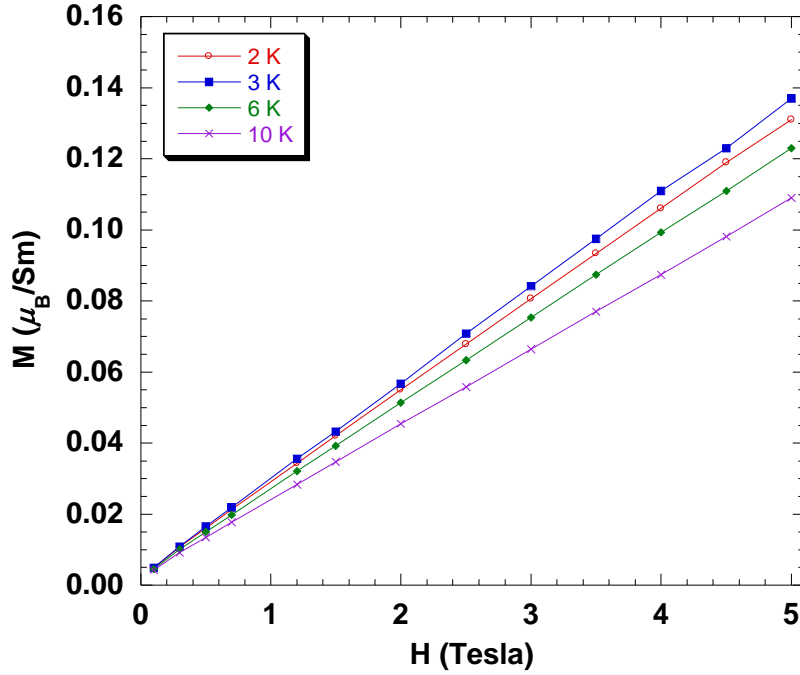
Figure 5.6 Magnetization of $SmCu_4Ga_8$ as a function of magnetic field at various temperatures is shown.

Figure 5.6 shows the isothermal magnetization data as a function of an applied field at various temperatures. The magnetization of $SmCu_4Ga_8$ increases without saturation up to 5 T which is typical behavior of antiferromagnetic materials. As shown in Figure 5.6, the isothermal magnetization versus magnetic field of $SmCu_4Ga_8$ decreases with increasing temperature in the paramagnetic state. The fact that the magnetization for the 2 K isotherm is below the 3 K is a direct consequence of the anti-alignment of the spins below T_N in the ordered state. No metamagnetic-like anomaly was observed up to 5T at 2K. The magnetization at 5 T is only about 0.14 μ_B, which is much smaller than the expected value of 0.71 μ_B for Sm.

The normalized temperature-dependent electrical resistance of a single crystal of $SmCu_4Ga_8$ is shown in Figure 5.7 and there is no indication of a kink or any anomaly at the magnetic transition as shown in the inset of Figure 5.7, which is quite unusual. Typically, one
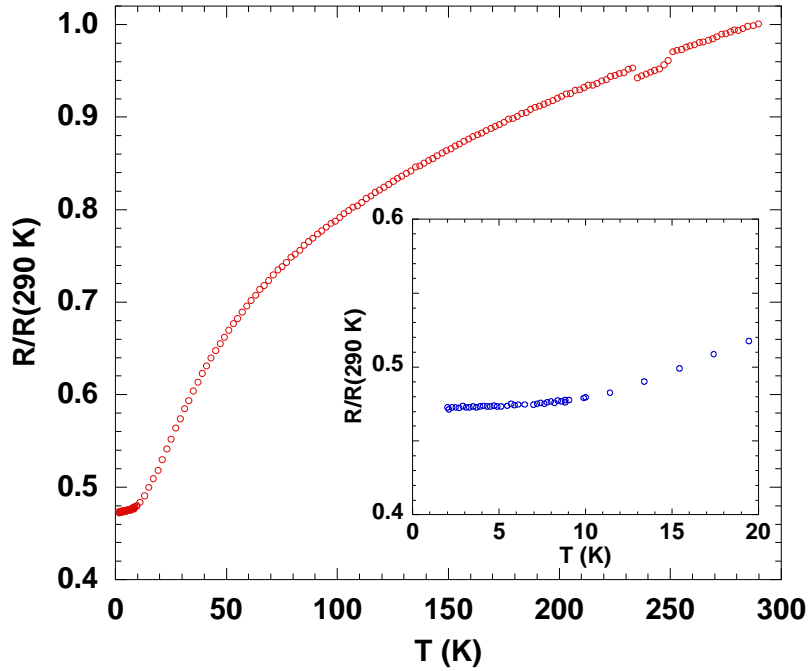
Figure 5.7 Normalized electrical resistance of $SmCu_4Ga_8$ as a function of temperature is shown. The inset shows the blow-up of the normalized electrical resistance between 2 K and 20 K.

would expect a kink in the resistivity at the magnetic transition, indicating the reduction of spin disorder scattering. Figure 5.8 shows the magnetoresistance (MR = $(\rho_H - \rho_0)/\rho_0 \times 100$ %) of a single crystal of $SmCu_4Ga_8$ as a function of field at 3 K. A large positive magnetoresistance, 40 % at 9 T is observed. Typically, close to a magnetic transition, one observes a negative MR due to the field-suppression of the spin fluctuations.[28] We, however, observe a large positive MR close to the magnetic transition. On the other hand, this result is consistent with the absence of a kink in resistance data at T_N, suggesting that the spin-disorder scattering does not play an important role in the transport property of $SmCu_4Ga_8$. The positive sign and the saturating behavior of the MR are compatible with classical (orbital) magnetoresistance. Further work is needed to

74
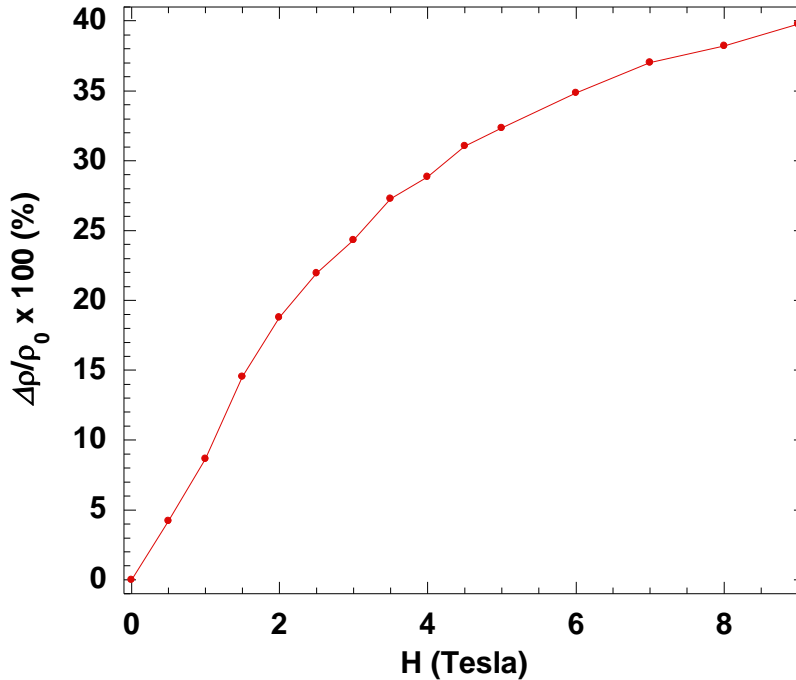
Figure 5.8 MR % of $SmCu_4Ga_8$ as a function of field at 3 K is shown.

establish the origin of the positive MR. Similar behavior has been reported in $SmPd_2Ga_2$,[13] which has a large positive magnetoresistance up to 100 % at 9 T and 2 K.

5.4 References

(1)   Suga, S.; Imada, S.; Jo, T.; Taniguchi, M.; Fujimori, A.; Oh, S.-J.; Kakizaki, A.; Ishii, T.; Miyahara, T.; et al. *Phys. Rev. B: Condens. Matter* **1995**, *51*, 2061-2067.

(2)   Chinchure, A. D.; Mazumdar, C.; Marathe, V. R.; Nagarajan, R.; Gupta, L. C.; Shah, S. S. *Phys. Rev. B: Condens. Matter* **1994**, *50*, 609-611.

(3)   Cohen, R. L.; Eibschuetz, M.; West, K. W. *Phys. Rev. Lett.* **1970**, *24*, 383-386.

(4)   Fukuhara, T.; Sakamoto, I.; Sato, H. *J. Phys.: Condens. Matter* **1991**, *3*, 8917-8929.

(5)   Stewart, A. M. *Phys. Rev. B: Condens. Matter* **1993**, *47*, 11242-11246.

(6)   Adachi, H.; Ino, H.; Miwa, H. *Phys. Rev. B: Condens. Matter* **1999**, *59*, 11445-11449.

(7)   Zaremba, V. I.; Kaczorowski, D.; Rodewald, U. C.; Hoffmann, R.-D.; Poettgen, R. *Chem. Mater.* **2004**, *16*, 466-476.

(8)   Kaczorowski, D.; Mudryk, Y.; Rogl, P.; Romaka, L.; Gorelenko, Y. *J. Phys.: Condens. Matter* **2003**, *15*, 2515-2522.

(9)   Zaremba, V. I.; Galadzhun, Y. V.; Belan, B. D.; Pikul, A.; Stepien-Damm, J.; Kaczorowski, D. *J. Alloys Compd.* **2001**, *316*, 64-69.

(10)   Grin, Y. N.; Hiebl, K.; Rogl, P.; Noel, H. *J. Less-Common Met.* **1990**, *162*, 371-377.

(11)   Tougait, O.; Ibers, J. A. *Inorg. Chem.* **2000**, *39*, 1790-1794.

(12)   Ban, Z.; Sikirica, M. *Acta Cryst.* **1965**, *18*, 594-599.

(13)   Williams, W. M.; Macaluso, R. T.; Moldovan, M.; Young, D. P.; Chan, J. Y. *Inorg. Chem.* **2003**, *42*, 7315-7318.

(14)   Van Dover, R. B.; Gyorgy, E. M.; Cava, R. J.; Krajewski, J. J.; Felder, R. J.; Peck, W. F. *Phys. Rev. B: Condens. Matter* **1993**, *47*, 6134-6137.

(15)   Brabers, J. H. V. J.; Bakker, K.; Nakotte, H.; de Boer, F. R.; Lenczowski, S. K. J.; Buschow, K. H. J. *J. Alloys Compd.* **1993**, *199*, L1-L3.

(16)   Markiv, V. Y.; Shevchenko, I. P.; Belyavina, N. N.; Kuzmenko, P. P. *Dopov Akad Nauk A* **1986**, 78-81.

(17)   Mason, J. T.; Harsha, K. S.; Chiotti, P. *Acta Crystallogr., Sect. B: Struct. Sci* **1970**, *26*, 356-361.

(18)   Sysa, L. V.; Kalychak, Y. M.; Ctets, I. N.; Galadzhun, Y. V. *Kristallografiya* **1994**, *39*, 821-824.

(19)   Svoboda, P.; Divis, M.; Bischof, J.; Smetana, Z.; Cerny, R.; Burianek, J. *Phys. Status Solidi A* **1990**, *119*, K67-K70.

(20)   Svoboda, P.; Divis, M.; Gratz, E.; Cerny, R.; Dobiasova, L. *Phys. Status Solidi A* **1991**, *123*, K149-K152.

(21)   Schubert, K. *Kristallstrukturen zweikomponentiger Phasen*; Springer-Verlag: Berlin, **1964**.

(22)   Haucke, W. *Z. Anorg. Allg. Chem.* **1940**, *244*, 17-22.

(23)   Wells, A. F. *Structural Inorganic Chemistry*; 3 ed.; Oxford University Press: London, **1967**.

(24)   Gulay, L. D.; Hiebl, K. *J. Alloys Compd.* **2003**, *351*, 35-39.

(25)   Kaczorowski, D.; Gulay, L. D. *J. Alloys Compd.* **2007**, *442*, 169-171.

(26)   Kaczorowski, D.; Gofryk, K.; Romaka, L.; Mudryk, Y.; Konyk, M.; Rogl, P. *Intermetallics* **2005**, *13*, 484-489.

(27)   Pagliuso, P. G.; Thompson, J. D.; Hundley, M. F.; Sarrao, J. L.; Fisk, Z. *Phys. Rev. B: Condens. Matter* **2001**, *63*, 054426/1-054426/4.

(28)   Usami, K. *J. Phys. Soc. Jpn.* **1978**, *45*, 466-75.

6.1 Introduction

Ternary lanthanide intermetallic compounds (*Ln-M-X*: *Ln* = lanthanide; *M* = transition metal; *X* = main group element) adopting the ThMn$_{12}$ structure type,[1,2] have been extensively studied and show a variety of interesting physical properties.[3-11] The ThMn$_{12}$ structure consists of four crystallographic sites: 2*a*, 8*f*, 8*i*, and 8*j*. The 2*a* site is occupied by the *f*-element, and transition metal and main group element are distributed amongst the 8f, 8i, and 8j and strongly depend on constituent elements. The magnetic properties of these types of compounds are due to lanthanide and transition metal. The magnetic ordering at low temperatures due to long-range lanthanide interactions has been reported in several compounds with transition metals such as Cr and Cu.[12-17] The ordered intemetallic *Ln*Cr$_4$Al$_8$ (*Ln* = La, Ce, Pr, Gd, Er) compounds have been studied.[12] CeCr$_4$Al$_8$ exhibits an enhanced Sommerfeld coefficient of specific heat, $\gamma \approx 62$ mJmol^{-1}K^{-2} and does not show a magnetic ordering down to 1.5 K. GdCr$_4$Al$_8$ and ErCr$_4$Al$_8$ show the antiferromagnetic ordering around 8 K and 14 K, respectively due to the lanthanide sublattice.[18] Similarly, CeCu$_4$Al$_8$ compound shows heavy-fermion behavior with $\gamma \approx 200$ mJmol^{-1}K^{-2} and an antiferromagnetic ordering at 5.8 K.[16] HoCu$_4$Al$_8$ and ErCu$_4$Al$_8$ compounds order antiferromagnetically at 5.5 K and 6 K, respectively, which is due to the lanthanide sublattice.[13,14] In the case where magnetic transition metal like Fe is present, the high and low temperature magnetic ordering, which are due to transition metal interactions and long-range lanthanide interactions, are observed. For example, ErFe$_4$Al$_8$ compound shows two magnetic transitions at 25 K and 111 K corresponding to the Er sublattice and the Fe sublattice ordering, respectively.[19] The ThMn$_{12}$-type intermetallic compounds of high concentration of Fe have been

widely studied because of their potential application to permanent magnetic materials having a high Curie point and a high magnetization.[7,20-22]

Compounds of RM_4Al_8 (R = Sc, Y, Ce, Yb, Lu; M = Cr, Mn, Fe)[5] have been reported to show negative magnetoresistance down to −20.1 % for $ScFe_4Al_8$. The negative magnetoresistance have been attributed the Kondo-like interaction and spin-glass state resulting from crystallographic disorder. However, the Cu and Ag analogues do not show negative magnetoresistance.[23] We have synthesized $Ln(Cu,Ga)_{12}$ (Ln = Y, Gd-Er, Yb) using Ga flux. In this chapter, we present magnetism, resistivity, and positive magnetoresistance of these compounds.

6.2 Experimental

6.2.1 Synthesis

Single crystals of $Ln(Cu,Ga)_{12}$ (Ln = Y, Gd-Er, Yb) were successfully grown in excess Ga flux. Ln (Ln = Y, Gd-Er, Yb; chunks, 99.9%, Alfa Aesar), Cu (powder, 99.999%, Alfa Aesar), and Ga (pellets, 99.9999%, Alfa Aesar) were weighed in a 1:5:20 molar ratio and placed into an alumina crucible. The crucible and its contents were then sealed in an evacuated fused silica tube and heated to 1373 K for 7 h. The tube was then slowly cooled to 673 K at a rate of 10 K/h and immediately inverted and spun with a centrifuge for the removal of excess Ga flux. Silver-colored block-like crystals (Figure 6.1) were found and not observed to degrade in air. To ensure the complete removal of Ga on surfaces, crystals were etched using a diluted HCl (1 M) solution. After etching crystals for several hours, reddish color on crystal surfaces were observed, which indicate the reduction of excess Cu as well as the completion of removal of Ga on crystal surfaces. The reduced Cu was successfully removed by using a diluted HNO_3 (30 %) solution.

79
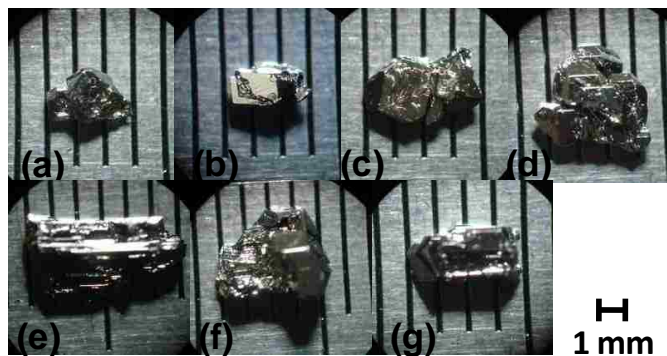
Figure 6.1 Single crystals of $Ln(Cu,Ga)_{12}$ (Ln = Y, Gd–Er, Yb) are shown. (a)–(g) correspond to the order for Y, Gd–Er, and Yb, respectively.

To investigate how heat treatment affects synthesis, reactions were also performed in the same reaction ratio of 1:5:20 with a different temperature profile. The crucible containing its contents was sealed in an evacuated fused silica tube and heated up to 1373 K for 7 h. After fast cooling to 773 K at a rate of 150 K/h, the tube was then slowly cooled to 673 K at a rate of 8 K/h and immediately inverted and spun with a centrifuge for the removal of excess Ga flux.

To investigate the stability of the ThMn$_{12}$ structure-type in Ln-Cu-Ga, systematic experiments varying Cu concentration were performed using Gd-Cu-Ga system as a model. These model experiments on Gd-Cu-Ga were performed with the first temperature profile. The variation of nominal concentration was increased from 1:3:20 to 1:11:20.

6.2.2 Single-Crystal X-ray Diffraction and Elemental Analysis

The crystals of $Ln(Cu,Ga)_{12}$ (Ln = Y, Gd-Er, Yb) were cut to suitable sizes for data collection (~ 0.05 mm^3) and mounted onto a glass fiber using epoxy. They were then positioned onto the goniometer of a Nonius KappaCCD diffractometer equipped with MoK$_\alpha$ radiation (λ = 0.71073 Å). Data collection was carried out up to θ = 30.0° at 298 K. Further crystallographic parameters for $Ln(Cu,Ga)_{12}$ (Ln = Y, Gd-Er, Yb) are provided in Table 6.1. Direct methods were used to solve the structure. SHELXL97 was used to refine the structural model of the

$Ln(Cu,Ga)_{12}$ (Ln = Y, Gd-Er, Yb) compounds, and data were corrected with extinction coefficients and refined with anisotropic displacement parameters. Refinement assuming a fully occupied formula led to convergence with very small final difference residual peaks. Atomic positions and displacement parameters for $Ln(Cu,Ga)_{12}$ (Ln = Y, Gd-Er, Yb) are provided in Table 6.2, and selected interatomic distances are presented in Table 6.3. To determine the composition of Cu and Ga concentration of $Ln(Cu,Ga)_{12}$ (Ln = Y, Gd-Er, Yb), electron probe microanalysis was performed using a JEOL JSM-5060 scanning electron microscope equipped with an energy dispersive spectrometer. The accelerating voltage was 15 kV with beam to sample distance of 20 mm. An average of 5-7 scans was performed on each single crystal. The results are provided in Table 6.4 and 6.8. After taking account of elemental analysis results, the structures of $Ln(Cu,Ga)_{12}$ (Ln = Y, Gd-Er, Yb) were carefully checked for a mixed occupancy on all of Cu and Ga sites, and refinements of single crystal X-ray diffraction data of Ln(Cu,Ga)12 (Ln = Y, Gd-Er, Yb) suggest that $8f$ and $8j$ sites are occupied statistically by Cu and Ga. The structural models showed the similar stoichiometry for Ln:Cu:Ga (Ln = Y, Gd-Er, Yb) to the result of elemental analysis. For simplicity, we report the compounds as $Ln(Cu,Ga)_{12}$ (Ln = Y, Gd-Er, Yb).

6.2.3 Physical Property Measurements

Magnetic data were obtained using a Quantum Design Physical Property Measurement System (PPMS). The temperature-dependent susceptibility data were obtained under zero-field cooled (ZFC) conditions from 2 K to 300 K with an applied field 0.1 T, and then measured upon heating to obtain field-cooled (FC) data after cooling to 2 K under field. Field-dependent magnetization data were measured at 3 K with field up to 9 T. The electrical resistivity and magnetoresistance (MR) were measured by the standard four-probe AC technique.

Table 6.1 Crystallographic Parameters for $Ln(Cu,Ga)_{12}$ (Ln = Y, Gd-Er, Yb)

Crystal data

	$Y(Cu,Ga)_{12}$	$Gd(Cu,Ga)_{12}$	$Tb(Cu,Ga)_{12}$	$Dy(Cu,Ga)_{12}$
Formula	$Y(Cu,Ga)_{12}$	$Gd(Cu,Ga)_{12}$	$Tb(Cu,Ga)_{12}$	$Dy(Cu,Ga)_{12}$
a (Å)	8.610(4)	8.637(3)	8.622(3)	8.612(3)
c (Å)	5.172(2)	5.175(2)	5.175(2)	5.171(2)
V (Å)	383.4(3)	386.0(2)	384.7(2)	383.5(2)
Z	2	2	2	2
Crystal dimension (mm^3)	0.05×0.05×0.05	0.03×0.03×0.03	0.03×0.03×0.03	0.03×0.03×0.03
Crystal system	Tetragonal	Tetragonal	Tetragonal	Tetragonal
Space group	$I4/mmm$	$I4/mmm$	$I4/mmm$	$I4/mmm$
θ range (°)	3.35-30.04	3.34-30.01	3.34-29.99	3.35-30.03
μ (mm^{-1})	45.810	46.534	47.268	47.936

Data collection

Measured reflections	442	482	450	475
Independent reflections	188	190	188	188
Reflections with $I>2\sigma(I)$	184	182	183	180
R_{int}	0.0467	0.0469	0.0422	0.0488
h	-11→12	-12→12	-11→12	-11→12
k	-8→8	-8→8	-8→8	-8→8
l	-7→5	-7→5	-7→5	-7→5

Refinement

[a]$R_1[F^2>2\sigma(F^2)]$	0.0265	0.0277	0.0339	0.0244
[b]$wR_2(F^2)$	0.0580	0.0651	0.0788	0.0599
Reflections	188	190	188	188
Parameters	16	16	16	16
$\Delta\rho_{max}$ (eÅ^{-3})	1.611	2.992	1.752	1.975
$\Delta\rho_{min}$ (eÅ^{-3})	-1.179	-1.869	-2.329	-1.060

$$^{a}R_1 = \sum ||F_o| - |F_c|| / \sum |F_o|$$

$$^{b}wR_2 = [\sum[w(F_o^2 - F_c^2)]/\sum[w(F_o^2)^2]]^{1/2}$$

Table 6.1 Continued

Crystal data			
Formula	Ho(Cu,Ga)$_{12}$	Er(Cu,Ga)$_{12}$	Yb(Cu,Ga)$_{12}$
a (Å)	8.600(3)	8.591(4)	8.650(3)
c (Å)	5.166(2)	5.163(3)	5.151(2)
V (Å)	382.1(2)	381.1(3)	385.4(2)
Z	2	2	2
Crystal dimension (mm^3)	0.03×0.03×0.03	0.05×0.05×0.03	0.05×0.05×0.05
Crystal system	Tetragonal	Tetragonal	Tetragonal
Space group	*I4*/*mmm*	I4/*mmm*	*I4*/*mmm*
θ range (°)	3.35-29.95	3.35-29.99	3.33-29.99
μ (mm^{-1})	48.692	49.452	50.139
Data collection			
Measured reflections	467	466	458
Independent reflections	185	187	190
Reflections with $I>2\sigma(I)$	180	179	183
R_{int}	0.0363	0.0402	0.0557
h	-11→12	-11→12	-12→12
k	-8→8	-8→8	-8→8
l	-7→5	-6→7	-7→5
Refinement			
[a]$R_1[F^2>2\sigma(F^2)]$	0.0344	0.0279	0.0231
[b]$wR_2(F^2)$	0.0916	0.0638	0.0574
Reflections	185	187	190
Parameters	16	16	16
$\Delta\rho_{max}$ (eÅ^{-3})	2.706	1.532	1.107
$\Delta\rho_{min}$ (eÅ^{-3})	-2.978	-1.591	-1.847

$$^a R_1 = \sum || F_o | - | F_c || / \sum | F_o |$$
$$^b wR_2 = [\sum [w(F_o^2 - F_c^2)] / \sum [w(F_o^2)^2]]^{1/2}$$

Table 6.2 Atomic Positions and Thermal Parameters for $Ln(Cu,Ga)_{12}$ (Ln = Y, Gd-Er, Yb)

Atom	Wyckoff position	x	y	z	U_{eq} (Å^2)[a]
Y	2a	0	0	0	0.0042(4)
Cu	8f	1/4	1/4	1/4	0.0078(3)
Ga1	8i	0.34746(9)	0	0	0.0097(3)
Ga2	8j	0.28574(12)	1/2	0	0.0140(3)
Gd	2a	0	0	0	0.0065(3)
Cu	8f	1/4	1/4	1/4	0.0096(4)
Ga1	8i	0.34776(12)	0	0	0.0121(4)
Ga2	8j	0.28486(16)	1/2	0	0.0161(4)
Tb	2a	0	0	0	0.0058(4)
Cu	8f	1/4	1/4	1/4	0.0089(5)
Ga1	8i	0.34734(17)	0	0	0.0113(4)
Ga2	8j	0.2853(2)	1/2	0	0.0161(5)
Dy	2a	0	0	0	0.0054(3)
Cu	8f	1/4	1/4	1/4	0.0089(4)
Ga1	8i	0.34707(13)	0	0	0.0108(4)
Ga2	8j	0.28590(17)	1/2	0	0.0158(4)
Ho	2a	0	0	0	0.0026(5)
Cu	8f	1/4	1/4	1/4	0.0060(5)
Ga1	8i	0.34684(19)	0	0	0.0079(5)
Ga2	8j	0.2861(2)	1/2	0	0.0132(5)
Er	2a	0	0	0	0.0028(4)
Cu	8f	1/4	1/4	1/4	0.0061(4)
Ga1	8i	0.34664(17)	0	0	0.0076(4)
Ga2	8j	0.2866(2)	1/2	0	0.0139(5)
Yb	2a	0	0	0	0.0048(3)
Cu	8f	1/4	1/4	1/4	0.0076(3)
Ga1	8i	0.34638(12)	0	0	0.0089(3)
Ga2	8j	0.28502(16)	1/2	0	0.0157(4)

[a]U_{eq} is defined as one-third of the trace of the orthogonalized U_{ij} tensor.

Table 6.3 Selected Interatomic Distances (Å) for Ln(Cu,Ga)$_{12}$ (Ln = Y, Gd-Er, Yb)

	Y(Cu,Ga)$_{12}$	Gd(Cu,Ga)$_{12}$	Tb(Cu,Ga)$_{12}$	Dy(Cu,Ga)$_{12}$	Ho(Cu,Ga)$_{12}$	Er(Cu,Ga)$_{12}$	Yb(Cu,Ga)$_{12}$
Ln environment							
Ln-Ga1(×8)	2.9916(16)	3.0036(15)	2.9947(18)	2.9890(15)	2.983(2)	2.978(2)	2.9961(15)
Ln-Ga2(×8)	3.1766(11)	3.1856(12)	3.1814(14)	3.1756(12)	3.1712(15)	3.1661(17)	3.1767(12)
Ln-Cu(×4)	3.3073(13)	3.3164(10)	3.3115(10)	3.3079(10)	3.3035(10)	3.3003(13)	3.3183(10)
Cu environment							
Cu-Cu(×2)	2.5860(10)	2.5875(10)	2.5875(10)	2.5855(10)	2.5830(10)	2.5815(15)	2.5755(10)
Cu-Ga1(×4)	2.6475(10)	2.6550(8)	2.6503(9)	2.6468(8)	2.6428(9)	2.6397(11)	2.6514(8)
Cu-Ga2(×4)	2.5298(9)	2.5351(7)	2.5323(7)	2.5303(7)	2.5272(7)	2.5255(10)	2.5350(7)
Ga1-Ga1(×1)	2.627(2)	2.630(2)	2.633(3)	2.634(2)	2.634(3)	2.635(3)	2.658(2)
Ga1-Ga2(×2)	2.7888(16)	2.7897(16)	2.790(2)	2.7923(17)	2.791(2)	2.793(2)	2.8007(16)
Ga1-Ga2(×2)	2.8289(11)	2.8297(12)	2.8290(13)	2.8277(12)	2.8247(15)	2.8240(17)	2.8151(12)
Ga2-Ga2(×2)	2.6089(19)	2.628(2)	2.618(3)	2.608(2)	2.602(3)	2.592(3)	2.630(2)

Table 6.4 Composition as obtained from Electron Probe Microanalysis

	(Cu:Ga) composition[a]
Y(Cu,Ga)$_{12}$	5.63(11):6.37(11)
Gd(Cu,Ga)$_{12}$	5.58(4):6.42(4)
Tb(Cu,Ga)$_{12}$	5.53(11):6.47(11)
Dy(Cu,Ga)$_{12}$	5.60(8):6.40(8)
Ho(Cu,Ga)$_{12}$	5.67(13):6.33(13)
Er(Cu,Ga)$_{12}$	5.66(10):6.34(10)
Yb(Cu,Ga)$_{12}$	5.36(10):6.64(10)

[a]Composition is normalized to lanthanide.

Table 6.5 Crystallographic Parameters for Gd(Cu,Ga)$_{12}$

Crystal data				
Formula	Gd(Cu,Ga)$_{12}$ (1:3:20)	Gd(Cu,Ga)$_{12}$ (1:7:20)	Gd(Cu,Ga)$_{12}$ (1:9:20)	Gd(Cu,Ga)$_{12}$ (1:11:20)
a (Å)	8.637(3)	8.635(3)	8.631(3)	8.629(2)
c (Å)	5.176(2)	5.172(2)	5.169(2)	5.1630(10)
V (Å)	386.1(2)	385.6(2)	385.1(2)	384.44(15)
Z	2	2	2	2
Crystal dimension (mm^3)	0.05×0.08×0.08	0.05×0.05×0.05	0.05×0.05×0.05	0.05×0.05×0.05
Crystal system	Tetragonal	Tetragonal	Tetragonal	Tetragonal
Space group	*I*4/*mmm*	*I*4/*mmm*	*I*4/*mmm*	*I*4/*mmm*

Table 6.5 Continued

θ range (°)	3.34-30.01	3.34-30.02	3.34-30.06	3.34-29.97
μ (mm^{-1})	46.525	46.582	46.652	46.728
Data collection				
Measured reflections	474	448	470	458
Independent reflections	189	190	191	188
Reflections with $I>2\sigma(I)$	184	185	186	185
R_{int}	0.0458	0.0428	0.0513	0.0371
h	-12→12	-12→12	-12→12	-11→12
k	-8→8	-8→8	-8→8	-8→8
l	-7→5	-7→5	-7→4	-5→7
Refinement				
[a]$R_1[F^2>2\sigma(F^2)]$	0.0339	0.0325	0.0305	0.0280
[b]$wR_2(F^2)$	0.0807	0.0726	0.0738	0.0654
Reflections	189	190	191	188
Parameters	16	16	16	16
$\Delta\rho_{max}$ (eÅ^{-3})	4.941	4.447	1.505	2.674
$\Delta\rho_{min}$ (eÅ^{-3})	-2.127	-1.939	-1.635	-1.898

[a] $R_1 = \sum ||F_o| - |F_c|| / \sum |F_o|$

[b] $wR_2 = [\sum [w(F_o^2 - F_c^2)] / \sum [w(F_o^2)^2]]^{1/2}$

Table 6.6 Atomic Positions and Thermal Parameters for Gd(Cu,Ga)$_{12}$

Atom		Wyckoff position	x	y	z	U_{eq} (Å^2)[a]
Gd	(1:3:20)	2a	0	0	0	0.0018(4)
Cu		8f	1/4	1/4	1/4	0.0053(5)
Ga1		8i	0.34799(16)	0	0	0.0077(5)
Ga2		8j	0.2845(2)	1/2	0	0.0109(5)
Gd	(1:7:20)	2a	0	0	0	0.0046(4)
Cu		8f	1/4	1/4	1/4	0.0082(4)
Ga1		8i	0.34797(16)	0	0	0.0104(4)
Ga2		8j	0.28502(19)	1/2	0	0.0139(5)
Gd	(1:9:20)	2a	0	0	0	0.0027(4)
Cu		8f	1/4	1/4	1/4	0.0061(4)
Ga1		8i	0.34789(16)	0	0	0.0089(4)
Ga2		8j	0.2852(2)	1/2	0	0.0128(5)

Table 6.6 Continued

Gd	(1:11:20)	2a	0	0	0	0.0015(4)
Cu		8f	1/4	1/4	1/4	0.0048(4)
Ga1		8i	0.34790(15)	0	0	0.0074(4)
Ga2		8j	0.28544(18)	1/2	0	0.0109(4)

[a]U_{eq} is defined as one-third of the trace of the orthogonalized U_{ij} tensor.

Table 6.7 Selected Interatomic Distances (Å) for $Gd(Cu,Ga)_{12}$

	$Gd(Cu,Ga)_{12}$ (1:3:20)	$Gd(Cu,Ga)_{12}$ (1:7:20)	$Gd(Cu,Ga)_{12}$ (1:9:20)	$Gd(Cu,Ga)_{12}$ (1:11:20)
Ln environment				
Ln-Ga1(×8)	3.0056(17)	3.0047(17)	3.0026(17)	3.0020(15)
Ln-Ga2(×8)	3.1876(13)	3.1833(13)	3.1807(13)	3.1768(10)
Ln-Cu(×4)	3.3165(10)	3.3155(10)	3.3139(10)	3.3126(7)
Cu environment				
Cu-Cu(×2)	2.5880(10)	2.5860(10)	2.5845(10)	2.5815(5)
Cu-Ga1(×4)	2.6558(9)	2.6548(9)	2.6532(9)	2.6521(7)
Cu-Ga2(×4)	2.5349(7)	2.5345(7)	2.5334(7)	2.5325(5)
Ga1-Ga1(×1)	2.626(3)	2.626(3)	2.626(3)	2.625(3)
Ga1-Ga2(×2)	2.7862(19)	2.7894(19)	2.7897(19)	2.7909(17)
Ga1-Ga2(×2)	2.8298(13)	2.8295(13)	2.8282(13)	2.8263(10)
Ga2-Ga2(×2)	2.632(3)	2.622(3)	2.618(3)	2.618(2)

Table 6.8 Composition as obtained from Electron Probe Microanalysis

	Nominal ratio	(Cu:Ga) composition[a]
$Gd(Cu,Ga)_{12}$	1:3:20	5.53(9):6.47(9)
$Gd(Cu,Ga)_{12}$	1:5:20	5.58(4):6.42(4)
$Gd(Cu,Ga)_{12}$	1:7:20	5.59(12):6.41(12)
$Gd(Cu,Ga)_{12}$	1:9:20	5.71(6):6.29(6)
$Gd(Cu,Ga)_{12}$	1:11:20	5.63(7):6.37(7)

[a]Composition is normalized to lanthanide.

6.3 Results and Discussion

6.3.1 Synthesis and Structure

Our exploration of Ln-Cu-Ga ternary system led to the study of two structure types; Ln(Cu,Ga)$_4$ (Ln = La and Ce) of the BaAl$_4$ type and Ln_2CuGa$_{12}$[24] which can be stabilized simultaneously in the Ga rich region of the ternary phase space depending on heat treatment using a reaction ratio of 1.5:1:15 or 2:1:20. After several synthetic attempts, Ln_2CuGa$_{12}$ phase can only be grown from by fast cooling. Ln(Cu,Ga)$_4$ phase has shown as a minor impurity in the trials to synthesize a pure Ln_2CuGa$_{12}$ because of the thermodynamic stability of Ln(Cu,Ga)$_4$ phase. To avoid forming the thermodynamically favored Ln(Cu,Ga)$_4$ phase, the reaction mixtures were fast cooled at a rate of 150 K/hr from the dwell temperature of 1323 K to 773 K, and then slow cooled to 673 K as described in synthesis section. From this reaction, we obtained phase-pure Ln_2CuGa$_{12}$ and realize that the slow cooling step is the key for forming Ln_2CuGa$_{12}$ phase.[24] These observations led us to explore the Ln-Cu-Ga system with a different reaction ratio of 1:5:20 by increasing Cu composition. Regardless of different heat treatment, the Ln-Cu-Ga with the reaction ratio of 1:5:20 yielded single phase of compounds of the NaZn$_{13}$ structure type[25] for Ln = La-Nd, Eu, and SmZn$_{11}$ structure type[26] for Ln = Sm. The latter lanthanides Ln = Y, Gd-Er, Yb form compounds of the ThMn$_{12}$ type. Futhermore, larger crystals are obtained when slower cooled. Herein, the late lanthanide compounds belonging to ThMn$_{12}$ structure type will be focused.

The structure of Y(Cu,Ga)$_{12}$ is shown in Figure 6.2a. Ln(Cu,Ga)$_{12}$ (Ln = Y, Gd-Er, Yb) crystallize in the tetragonal $I4/mmm$ (No. 139) space group with the Ln, Cu, Ga1, and Ga2 occupying 2a, 8f, 8i, and 8j, respectively. Ln atoms occupy the 2a sites (4/mmm) at the corners and the center of the unit cell. Ln atoms are surrounded by 8 Cu, 4 Ga1, and 8 Ga2 atoms, which
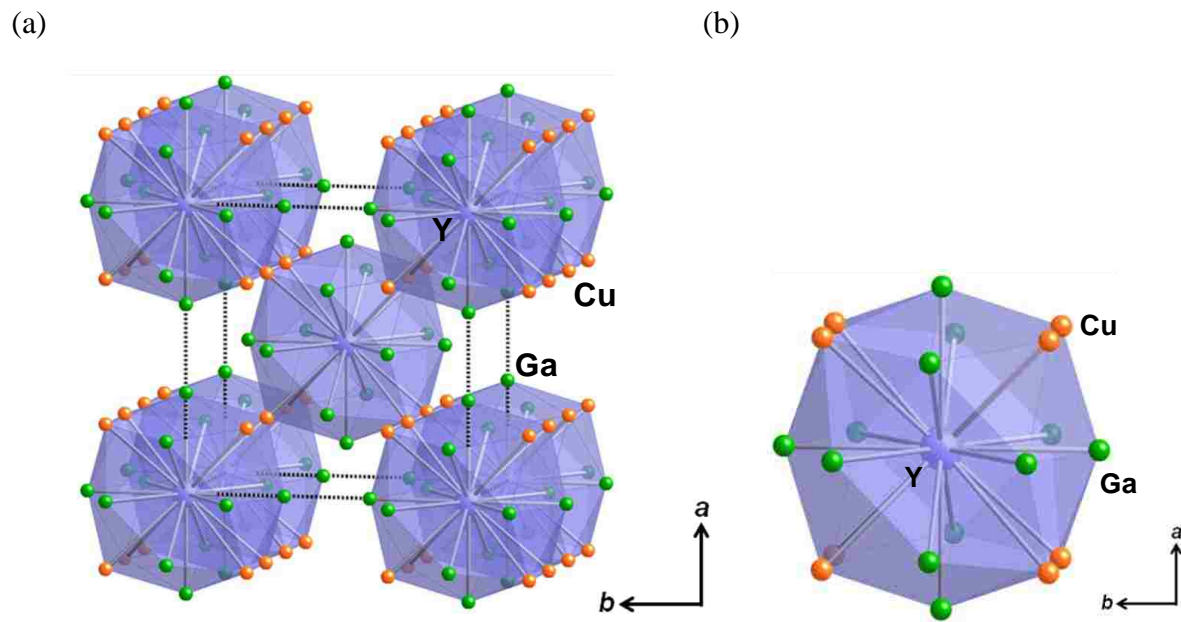
Figure 6.2 The crystal structure of $Y(Cu,Ga)_{12}$ is shown in (a), where the Y atoms are represented with blue spheres; Cu atoms are denoted as orange spheres; and the Ga atoms are denoted with green spheres. Dashed lines are used to show the unit cell. The local (b) Y environment is shown.

are positioned at $8f$, $8i$, and $8j$ sites, respectively. Y environment of $Y(Cu,Ga)_{12}$ is similar to the one of $SmCu_4Ga_8$, which belongs to a family of $CaCu_5$ structure type. Y atoms coordinated by 2 Ga1 and 4 Ga2 atoms in the basal plane has a six-membered ring composed of 4 Cu and 2 Ga2 atoms above and below the basal plane and the rings are capped by Ga1 atom as shown in the Figure 2b. The interatomic distances for Ln-Cu, Ln-Ga1, and Ln-Ga2 range from 2.978(2) Å to 3.3183(10) Å and are listed in Table 6.3.

Figure 6.3a and 6.3b show the structural relationship between $ThMn_{12}$ and $CaCu_5$ structure-type[27] (Hereafter, $ThMn_{12}$ and $CaCu_5$ are represented as RT_{12} and RT_5, respectively for clarity). The relationship can also be described as the following equations: $aRT_{12} \approx \sqrt{3}aRT_5 \approx 2cRT_5$; $cRT_{12} \approx aRT_5 \approx aRT_{12}/\sqrt{3}$.[26,28] The transformation from RT_5 to RT_{12} structure is caused by systematic substitution of a pair of T atoms for R atom along the c-axis from the parental RT_5

(a)

(b)   (c)

Figure 6.3 (a) The relationship between RT_{12} and RT_5. The unit cell of (b) RT_{12}, in which the RT_5 unit cell is marked by solid lines. The original (c) unit cell of RT_5 is shown for comparison.

structure. This can be described as equation; $2(RT_5) - R + 2T$ (a pair of Ts) $\rightarrow RT_{12}$.[29,30] The relationship of the crystallographic sites between the hexagonal *P6/mmm* RT_5 and tetragonal *I4/mmm* RT_{12} can be explained as shown in Figure 6.3*a-c*.

The variation of the unit cell volume as a function of rare earth is shown in Figure 6.4. As the lanthanide radius becomes smaller, the unit cell volume decreases due to lanthanide contraction except ytterbium. The *c/a* ratio of *Ln*(Cu,Ga)$_{12}$ (*Ln* = Y, Gd-Er, Yb) compounds is ~ 0.6 which is larger than ~ 0.58 of the other transition metal analogues such as *Ln*Cr$_4$Al$_8$, *Ln*Mn$_4$Al$_8$, *Ln*Fe$_6$Al$_6$, *Ln*Mn$_6$Al$_6$, and *Ln*Cr$_6$Al$_6$ adopting ThMn$_{12}$ structure type.[31]
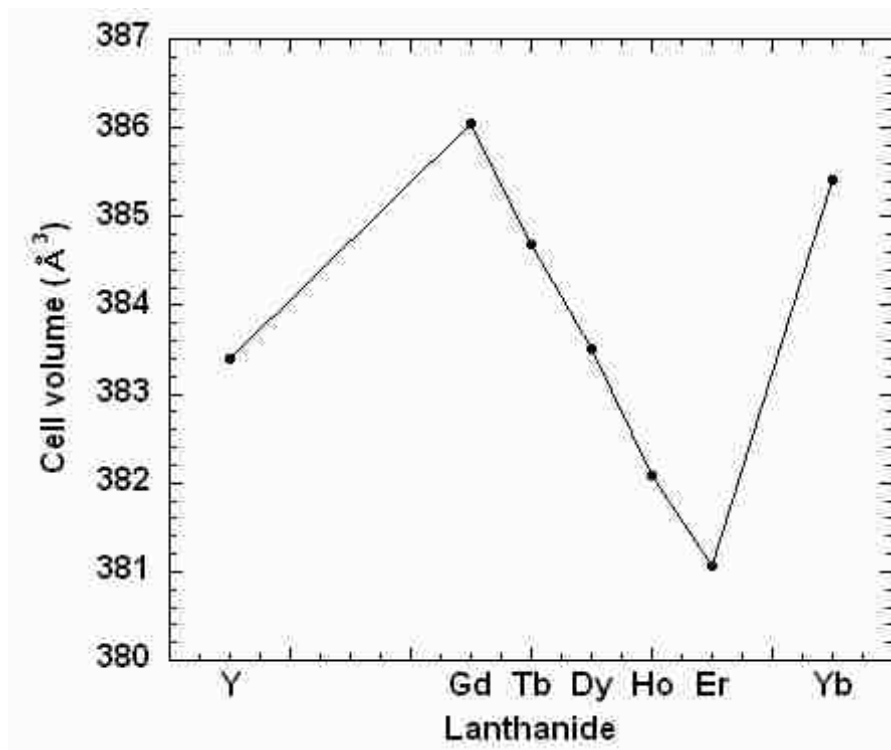
Figure 6.4 The unit cell volumes of $Ln(Cu,Ga)_{12}$ (Ln = Y, Gd-Er, Yb) are shown.

In the refined models, 8f and 8j sites can be occupied by both of Cu and Ga. It is well known that ThMn$_{12}$ structure is stabilized by the third component and is reported for Cr, Mn, Fe, Co, Ni and Cu compounds. Ga atom serves as a stabilizer to form ThMn$_{12}$ structure in Ln-Cu-Ga system. To investigate the limit of solid solution in Ln-Cu-Ga ternary system, systematic experiments with the variation of Cu concentration were performed with Gd-Cu-Ga as a model and the results are presented in Tables 6.5-6.8. As the concentration of Cu increases, the unit cell volume of Gd(Cu,Ga)$_{12}$ decreases. Interestingly, the c/a ratio of the series remains ~ 0.6 although the unit cell volume of Gd(Cu,Ga)$_{12}$ decreases. However, it should be noted that there is only small range of change from 5.53(9) to 5.71(6) for Cu composition by flux-growth as the nominal Cu concentration increases.

6.3.2 Physical Properties

Figures 6.5-6.9 shows the temperature-dependent magnetic susceptibility of single crystal of Ln(Cu,Ga)$_{12}$ (Ln = Gd-Er) measured at an applied field of 0.1 Tesla along the crystallographic c-axis and ab-plane. The magnetic susceptibility of the compounds was fitted to a Curie-Weiss equation of the following form: $\chi(T) = C/(T - \theta)$, where C represents the Curie constant and θ is the Weiss temperature at paramagnetic temperature ranges ($T > 50$ K). The effective moments were obtained from $\mu_{eff} = g_J(J(J+1))^{1/2}$ and summarized in Table 9.

For Y(Cu,Ga)$_{12}$ and Yb(Cu,Ga)$_{12}$ the magnetic susceptibility is positive, but negligible without temperature dependence which is not shown here. This result indicates that the ytterbium ion in Yb(Cu,Ga)$_{12}$ may be divalent state. Another evidence for the divalent state of ytterbium is pointed out in the unit cell volume of Yb(Cu,Ga)$_{12}$ as shown in Figure 6.4.

The temperature-dependent magnetization along the two crystallographic directions of Gd(Cu,Ga)$_{12}$ is shown in Figure 6.5a and is isotropic in whole temperature ranges. Gd(Cu,Ga)$_{12}$ shows magnetic ordering at 12.5 K for both directions. The effective moments of 8.35 μ_B/Gd (H ∥ c) and 7.85 μ_B/Gd (H ∥ ab) which are close to the calculated value of 7.94 μ_B for Gd^{3+} were obtained and large negative Weiss constants, $\theta = -36.32$ K and -28.42 K for the c-axis and ab-plane, respectively, indicate strong antiferromagnetic correlations in this compound. The field-dependent magnetization for Gd(Cu,Ga)$_{12}$ at 3 K is also isotropic with a metamagnetic transition at ~1.5 T for both directions as shown in Figure 6.5b. As explained in the structure section, one would expect a decreased ordering temperature due to a systematic substitution of a pair of T (T = Cu or Ga in this case) atoms for magnetic Gd atoms in Gd(Cu,Ga)$_{12}$. For example, GdCu$_5$ and GdCu$_4$Ga, which are isostructural to RT_5 structure type, show antiferromagnetic transition at 26 K with $\theta = 7$ K and 36 K with $\theta = -7.4$ K for former and latter compound, respectively.[32,33]

(a)
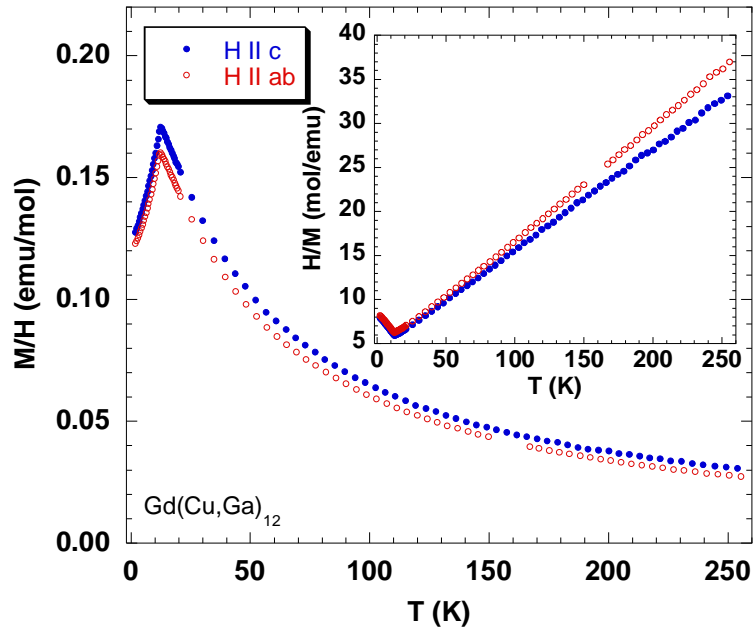
(b)
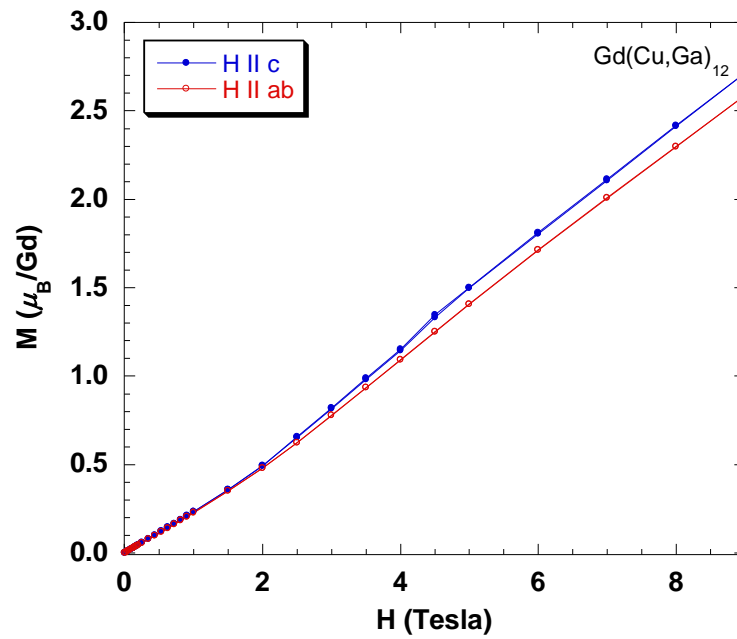
Figure 6.5 (a) Magnetic susceptibility (emu/mol Gd) of Gd(Cu,Ga)$_{12}$ as a function of temperature is shown. The inset shows the inverse magnetic susceptibility. (b) Magnetization of Gd(Cu,Ga)$_{12}$ as a function of field.

Figure 6.6a shows the temperature-dependent magnetization for Tb(Cu,Ga)$_{12}$. A down turn at 13.5 K, which indicates antiferromagnetic ordering, is observed for both directions. Unlike Gd analogue, a clear anisotropic behavior at low temperatures is shown in the temperature-dependent magnetization of Tb(Cu,Ga)$_{12}$. The magnetic susceptibility data of Tb(Cu,Ga)$_{12}$ can be fitted to a modified Curie-Weiss law in the following form: $\chi(T) = \chi_0 + C/(T - \theta)$, where χ_0 denotes the temperature-independent term, C represents the Curie constant and θ is the Weiss temperature giving effective moments of 10.74 μ_B/Tb (H ∥ c) and 10.96 μ_B/Tb (H ∥ ab) which are close to the calculated value of 9.72 μ_B for Tb^{3+} and large negative Weiss constants, θ = −23.45 K and −83.18 K for the c-axis and ab-plane, respectively, indicating strong antiferromagnetic correlations. The field-dependent magnetization for Tb(Cu,Ga)$_{12}$ at 3 K is also anisotropic and does not saturate up to 9 T for both directions (Figure 6.6b).

Antiferromagnetic transition at 6.7 K in Dy(Cu,Ga)$_{12}$ is observed for both crystallographic directions (Figure 6.7a). The temperature-dependent magnetization of Dy(Cu,Ga)$_{12}$ shows anisotropic behavior. The data fit above 50 K yields effective moments of 10.85 μ_B/Dy (H ∥ c) and 10.76 μ_B/Dy (H ∥ ab) which are close to the expected value of 10.65 μ_B for Dy^{3+} and negative Weiss constants, θ = −1.16 K and −53.97 K for the c-axis and ab-plane, respectively, consistent with antiferromagnetic ordering. Figure 6.7b shows the field-dependent isothermal magnetization of Dy(Cu,Ga)$_{12}$ at 3 K. The data show anisotropic behavior and saturation along the c-axis.

(a)

(b)
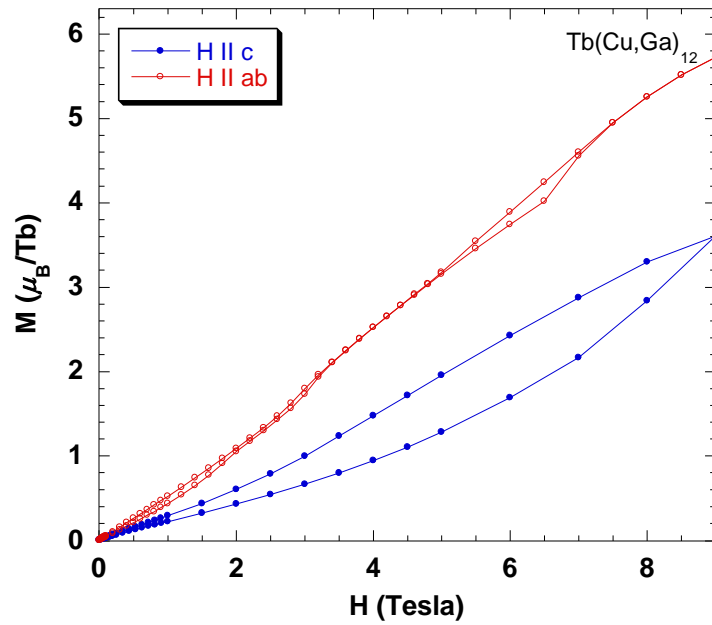
Figure 6.6 (a) Magnetic susceptibility (emu/mol Tb) of $Tb(Cu,Ga)_{12}$ as a function of temperature is shown. The inset shows the inverse magnetic susceptibility. (b) Magnetization of $Tb(Cu,Ga)_{12}$ as a function of field.

(a)
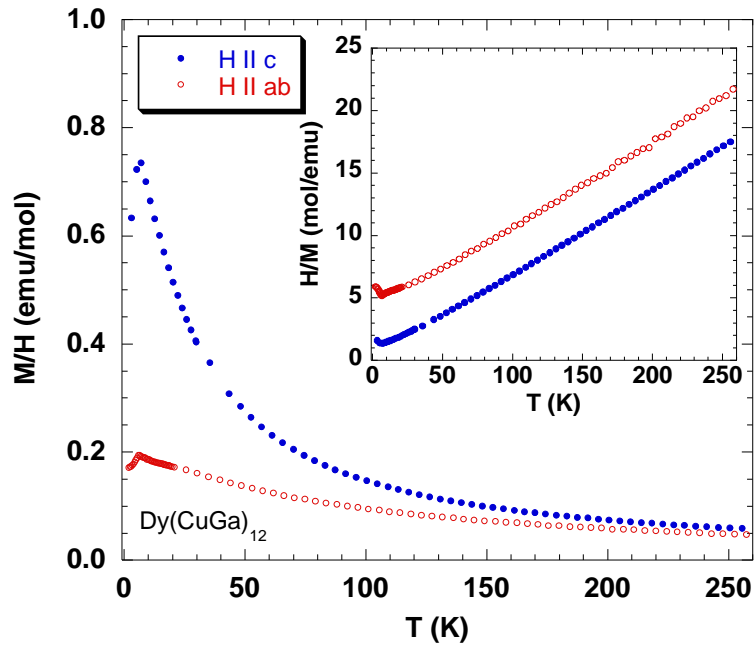
(b)
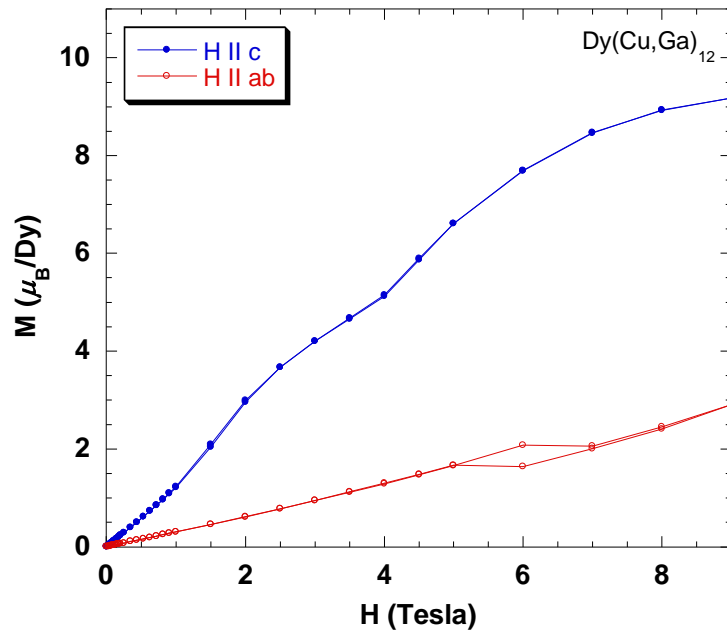
Figure 6.7 (a) Magnetic susceptibility (emu/mol Dy) of Dy(Cu,Ga)$_{12}$ as a function of temperature is shown. The inset shows the inverse magnetic susceptibility. (b) Magnetization of Dy(Cu,Ga)$_{12}$ as a function of field.

Figure 6.8a shows the temperature-dependent magnetic susceptibility of Ho(Cu,Ga)$_{12}$ and no magnetic ordering is observed down to 2 K for both crystallographic directions. The data fit above 50 K gives effective moments of 10.51 μ_B/Ho (H ∥ c) and 10.71 μ_B/Ho (H ∥ ab) with large negative Weiss constant, $\theta = -28.17$ K along the ab-plane indicating strong antiferromagnetic correlations. The field-dependent isothermal magnetization for Ho(Cu,Ga)$_{12}$ at 3 K is anisotropic and reaches up to the moment of 7.63 μ_B/Ho (H ∥ c) and 4.88 μ_B/Ho (H ∥ ab), respectively (Figure 6.8b).

Highly anisotropic behavior of the magnetic susceptibility on Er(Cu,Ga)$_{12}$ crystal is shown in Figure 6.9a. Er(Cu,Ga)$_{12}$ shows antiferromagnetic transition at 3.4 K along the c-axis, however no magnetic ordering along the ab-plane is observed down to 2 K. Effective moments of 9.59 μ_B/Er (H ∥ c) and 9.60 μ_B/Er (H ∥ ab) and Weiss constants, $\theta = 13.48$ K and -15.16 K for the c-axis and ab-plane, respectively, are obtained by using a modified Curie-Weiss fit at paramagnetic temperature range (> 50 K). The field-dependent magnetization for Er(Cu,Ga)$_{12}$ at 3 K also show anisotropic behavior consistent with magnetic susceptibility data. The magnetization of Er(Cu,Ga)$_{12}$ along the c-axis, which is an easy axis, saturates at 3 K since the easy axis is easily polarized (f electrons) under magnetic field (Figure 6.9b).

The electrical resistivities as a function of temperature of single crystals of Ln(Cu,Ga)$_{12}$ (Ln = Y, Gd-Er, Yb) are shown in Figure 6.10. These compounds show metallic behavior with residual resistivity ratio (RRR) values of 4.1, 5.2, 2.3, 4.9, 3.1, 2.5, and 1.9 for Y, Gd, Tb, Dy, Ho, Er, and Yb analogues, respectively. The inset of Figure 6.10 shows a blow-up of the low temperature resistivity data. There is no indication of a kink or any anomaly at their magnetic transition corresponding to the reduction of spin disorder scattering. Figure 6.11 shows the magnetoresistance (MR = $(\rho_H - \rho_0)/\rho_0 \times 100$ %) of single crystals of Ln(Cu,Ga)$_{12}$ (Ln = Y, Gd-Er)
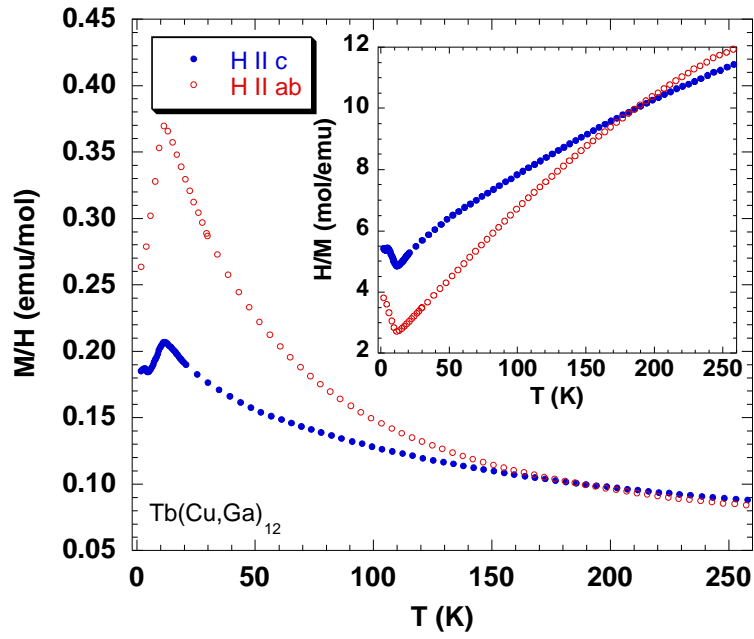
(a)
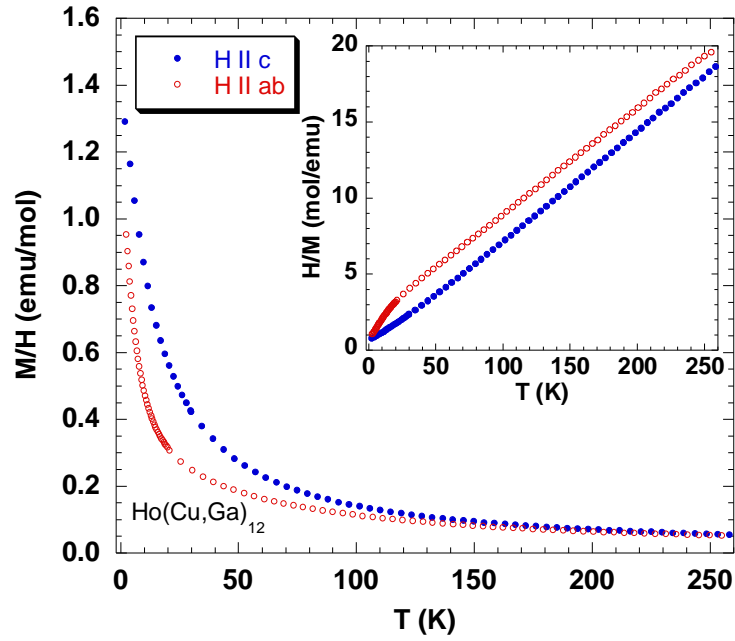
(b)
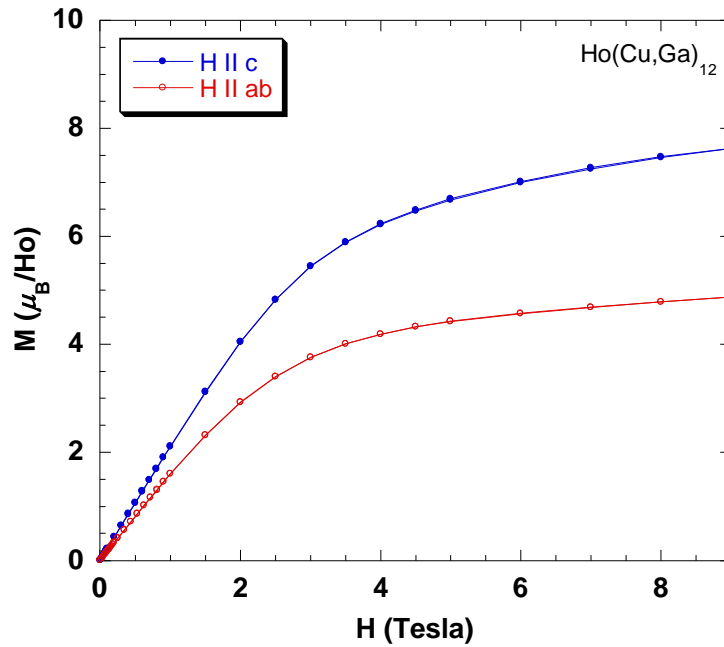
Figure 6.8 (a) Magnetic susceptibility (emu/mol Ho) of Ho(Cu,Ga)$_{12}$ as a function of temperature is shown. The inset shows the inverse magnetic susceptibility. (b) Magnetization of Ho(Cu,Ga)$_{12}$ as a function of field.

(a)
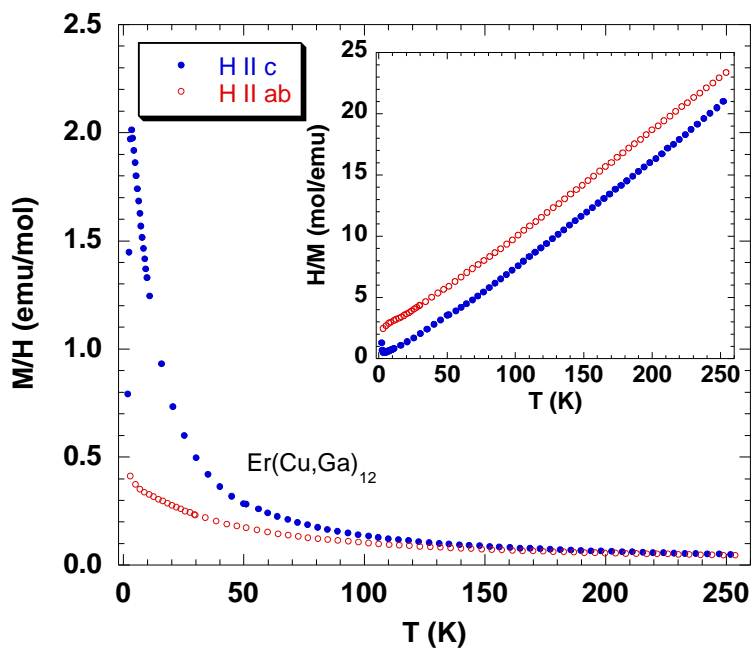
(b)
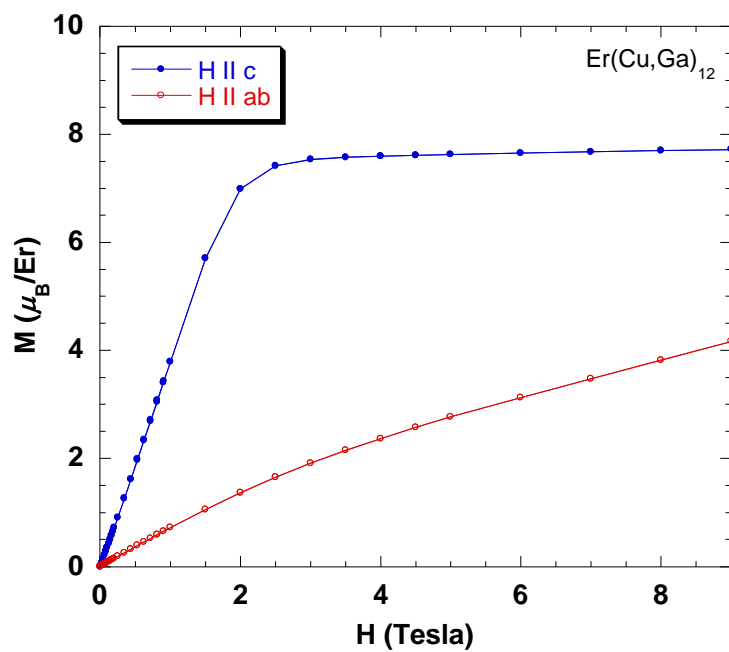
Figure 6.9 (a) Magnetic susceptibility (emu/mol Er) of Er(Cu,Ga)$_{12}$ as a function of temperature is shown. The inset shows the inverse magnetic susceptibility. (b) Magnetization of Er(Cu,Ga)$_{12}$ as a function of field.
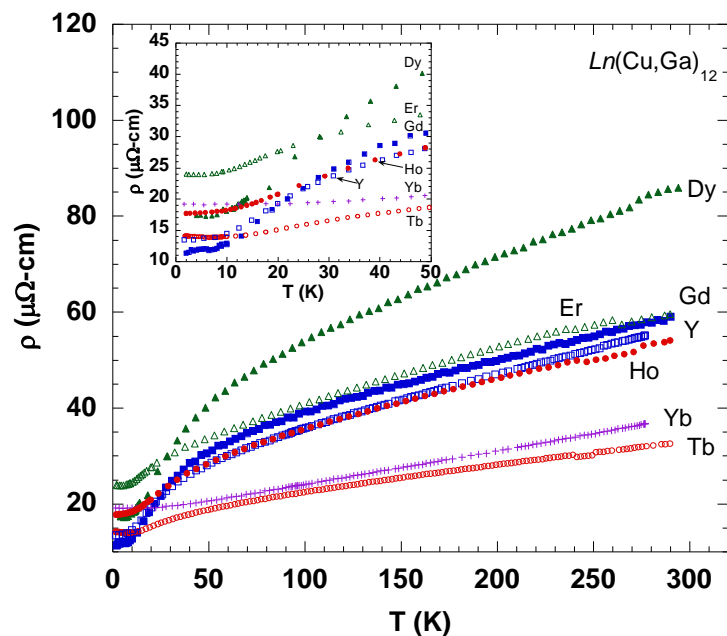
Figure 6.10 Normalized electrical resistivity of $Ln(Cu,Ga)_{12}$ (Ln = Y, Gd-Er, Yb) as a function of temperature is shown.
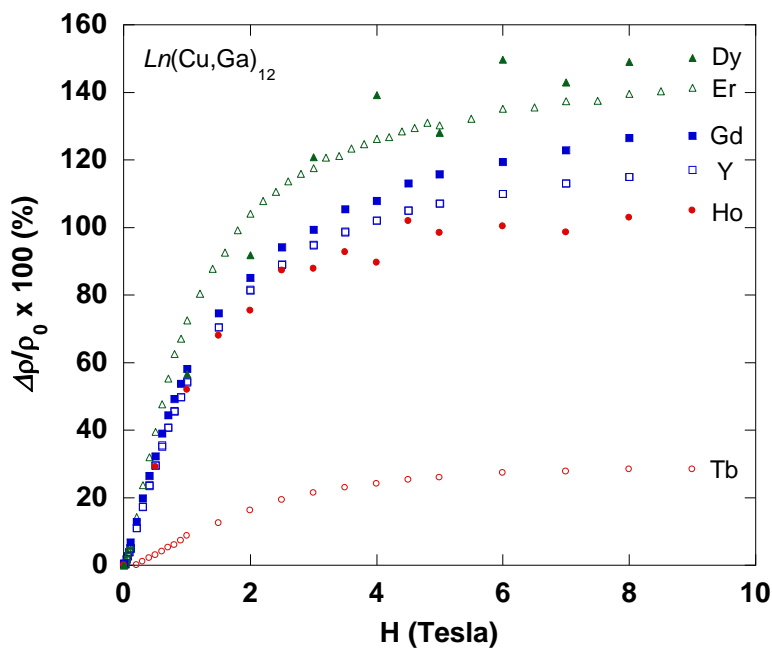
Figure 6.11 MR % of $Ln(Cu,Ga)_{12}$ (Ln = Y, Gd-Er) as a function of field at 3 K is shown.

as a function of field at 3 K. Interestingly, large positive magnetoresistance with 117%, 127%, 28%, 150%, 105%, and 141% are observed for Y, Gd, Tb, Dy, Ho, and Er analogues unlike in the case of the RM_4Al_8 (R = Sc, Y, Ce, Yb, Lu; M = Cr, Mn, Fe) compounds which show negative magnetoresistance due to the Kondo-like interaction and spin-glass state resulting from crystallographic disorder. Most interestingly, $Y(Cu,Ga)_{12}$ compound behaves like other magnetic analogues in magnetoresistance. Although this phenomenon is unexpected on a non-magnetic analogue, similar behavior has reported in $LaSb_2$ compound.[34]

Table 6.9 Magnetic Properties of $Ln(Cu,Ga)_{12}$ (Ln = Y, Gd-Er, Yb)

|	C	θ	μ_{calc} (μ_B)	μ_{eff} (μ_B)	Fit range (K)	Ordering T_N (K)
$Y(Cu,Ga)_{12}$	-	-	-	-	-	PPM[a]
$Gd(Cu,Ga)_{12}$	8.728	-36.32	7.94	8.35	50-260	AFM[b] 12.5 (H ∥ c)
	7.704	-28.42	7.94	7.85	50-260	AFM 12.5 (H ∥ ab)
$Tb(Cu,Ga)_{12}$	14.435	-23.45	9.72	10.74	50-260	AFM 13.5 (H ∥ c)
	15.023	-83.18	9.72	10.96	50-260	AFM 13.5 (H ∥ ab)
$Dy(Cu,Ga)_{12}$	14.740	-1.16	10.65	10.85	50-260	AFM 6.7 (H ∥ c)
	14.502	-53.97	10.65	10.76	50-260	AFM 6.7 (H ∥ ab)
$Ho(Cu,Ga)_{12}$	13.821	1.03	10.61	10.51	50-260	PM[c] (H ∥ c)
	14.352	-28.17	10.61	10.71	50-260	PM (H ∥ ab)
$Er(Cu,Ga)_{12}$	11.517	13.48	9.58	9.59	50-260	AFM 3.4 (H ∥ c)
	11.535	-15.16	9.58	9.60	50-260	PM (H ∥ ab)
$Yb(Cu,Ga)_{12}$	-	-	-	-	-	PPM

[a] Pauli Paramagnetic. [b] Antiferromagnetic. [c] Paramagnetic.

Figure 6.12 shows the unit cell volume and Weiss temperature (θ) as a function of nominal Cu concentration. As Cu concentration increases, the unit cell volume and Weiss temperature decrease. The temperature-dependent magnetization of $Gd(Cu,Ga)_{12}$ in different nominal Cu concentration is shown in Figure 6.13a. An increase of magnetic ordering from 12.0 K to 13.0 K is shown as the nominal Cu concentration increases (as the unit cell volume

decreases). The field-dependent magnetization for Gd(Cu,Ga)$_{12}$ series at 3 K is shown in Figure

6.13b. Magnetic properties for Gd(Cu,Ga)$_{12}$ series are summarized in Table 6.10.

Table 6.10 Magnetic Properties of Gd(Cu,Ga)$_{12}$

	C	θ	μ_{calc} (μ_B)	μ_{eff} (μ_B)	Fit range (K)	Ordering T_N (K)
Gd(CuGa)$_{12}$ 1:3:20	7.895	-29.90	7.94	7.94	50-260	AFM [a]12.0 (H ∥ ab)
Gd(CuGa)$_{12}$ 1:5:20	7.704	-28.42	7.94	7.85	50-260	AFM 12.5 (H ∥ ab)
Gd(CuGa)$_{12}$ 1:7:20	7.895	-30.55	7.94	7.94	50-260	AFM 13.0 (H ∥ ab)
Gd(CuGa)$_{12}$ 1:9:20	7.324	-33.48	7.94	7.65	50-260	AFM 13.0 (H ∥ ab)
Gd(CuGa)$_{12}$ 1:11:20	7.957	-34.69	7.94	7.97	50-260	AFM 13.0 (H ∥ ab)

[a]Antiferromagnetic.
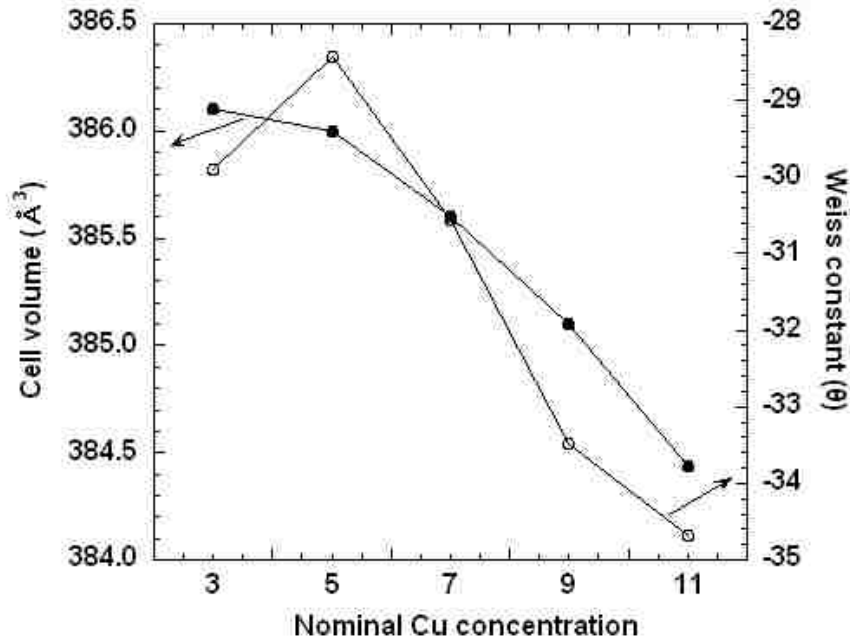
Figure 6.12 The unit cell volumes and Weiss-constant of Gd(Cu,Ga)$_{12}$ series are shown.

(a)
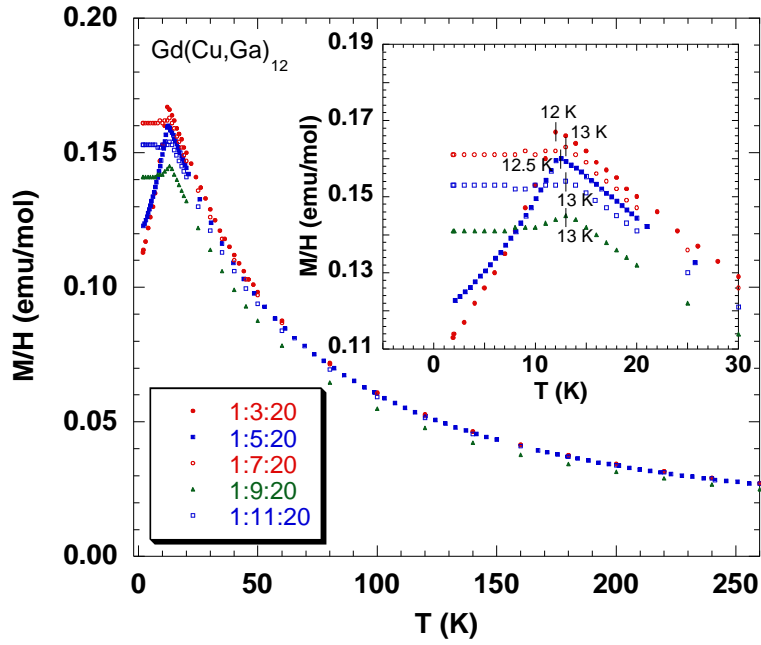
(b)
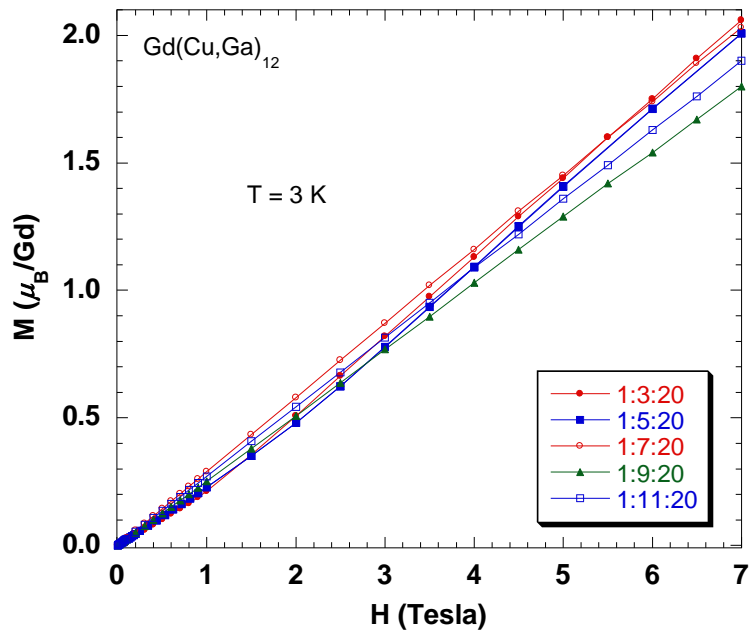
Figure 6.13 (a) Magnetic susceptibility (emu/mol Gd) of Gd(Cu,Ga)$_{12}$ in different nominal Cu concentration as a function of temperature is shown. The inset shows the blow-up of magnetic susceptibility at low temperatures. (b) Magnetization of Gd(Cu,Ga)$_{12}$ in different nominal Cu concentration as a function of field.

6.4 References

(1) Florio, J. V.; Rundle, R. E.; Snow, A. I. *Acta Cryst.* **1952**, *5*, 449-457.

(2) Gladishevskii, E. I.; Kripyakevich, P. I.; Teslvuk, M. Y.; Zarechnyuk, O. S.; Kuz'ma, Y. B. *Kristallografiya* **1961**, *6*, 267-268.

(3) Dmitriev, V. M.; Stepien-Damm, J.; Suski, W.; Talik, E.; Prentslau, N. N. *Phys. Status Solidi C* **2004**, *1*, 1824-1827.

(4) Christides, C.; Kostikas, A.; Zouganelis, G.; Psyharis, V.; Kou, X. C.; Grossinger, R. *Phys. Rev. B* **1993**, *47*, 11220-11229.

(5) Dmitriev, V. M.; Terekhov, A. V.; Suski, W.; Ishchenko, L. A.; Cwik, J.; Palewski, T.; Kotur, B. Y.; Talik, E. *J. Alloys Compd.* **2008**, *452*, 217-224.

(6) Coldea, M.; Neumann, M.; Lutkehoff, S.; Mahl, S.; Coldea, R. *J. Alloys Compd.* **1998**, *278*, 72-79.

(7) Moze, O.; Caciuffo, R.; Li, H. S.; Hu, B. P.; Coey, J. M. D.; Osborn, R.; Taylor, A. D. *Phys. Rev. B: Condens. Matter* **1990**, *42*, 1940-1943.

(8) Gottwick, U.; Held, R.; Sparn, G.; Steglich, F.; Vey, K.; Assmus, W.; Rietschel, H.; Stewart, G. R.; Giorgi, A. L. *J. Magn. Magn. Mater.* **1987**, *63-64*, 341-3.

(9) Kotur, B. Y.; Palasyuk, A. M.; Bauer, E.; Michor, H.; Hilscher, G. *J. Phys.: Condens. Matter* **2001**, *13*, 9421-9431.

(10) Yamasaki, T.; Matsui, K.; Nakamura, H.; Shiga, M. *Solid State Commun.* **2001**, *119*, 415-418.

(11) Leavey, C. J.; Rainford, B. D.; Stewart, J. R.; Adroja, D. T. *J. Magn. Magn. Mater.* **2007**, *310*, 1041-1043.

(12) Hagmusa, I. H.; Klaasse, J. C. P.; Bruck, E.; de Boer, F. R.; Buschow, K. H. J. *J. Alloys Compd.* **2001**, *314*, 37-41.

(13) Hagmusa, I. H.; Kayzel, F. E.; Bruck, E.; Buschow, K. H. J. *J. Appl. Phys.* **1998**, *83*, 7136-7138.

(14) Lue, C. S.; Su, T. H.; Lai, W. J. *J. Magn. Magn. Mater.* **2006**, *304*, e445-e447.

(15) Paci, B.; Caciuffo, R.; Amoretti, G.; Moze, O.; Buschow, K. H. J.; Murani, A. P. *Solid State Commun.* **1995**, *94*, 489-493.

(16) Ido, H.; Nishioka, T.; Kontani, M. *J. Magn. Magn. Mater.* **1998**, *177-181*, 385-386.

(17)   Baio, G.; Moze, O.; Amoretti, G.; Sonntag, R.; Stusser, N.; Buschow, K. H. J. *Z. Phys. B: Condens. Matter* **1997**, *102*, 449-453.

(18)   Felner, I.; Nowik, I. *J. Phys. Chem. Solids* **1979**, *40*, 1035-1044.

(19)   Caciuffo, R.; Amoretti, G.; Buschow, K. H. J.; Moze, O.; Murani, A. P.; Paci, B. *J. Phys.: Condens. Matter* **1995**, *7*, 7981-9.

(20)   De Boer, F. R.; Ying-Kai, H.; De Mooij, D. B.; Buschow, K. H. J. *J. Less-Common Met.* **1987**, *135*, 199-204.

(21)   De Mooij, D. B.; Buschow, K. H. J. *J. Less-Common Met.* **1988**, *136*, 207-215.

(22)   Buschow, K. H. J. *J. Magn. Magn. Mater.* **1991**, *100*, 79-89.

(23)   Gurevich, A. M.; Dmitriev, V. M.; Eropkin, V. N.; Kotur, B. Y.; Prentslau, N. N.; Suski, V.; Terekhov, A. V.; Shlyk, L. V. *Low Temp. Phys.* **2001**, *27*, 967-973.

(24)   Cho, J.; Millican, J. N.; Capan, C.; Sokolov, D. A.; Moldovan, M.; Karki, A. B.; Young, D. P.; Aronson, M. C.; Chan, J. Y. *Chem. Mater.* **2008**, *Submitted.*

(25)   Shoemaker, D. P.; Marsh, R. E.; Ewing, F. J.; Pauling, L. *Acta Cryst.* **1952**, *5*, 637-644.

(26)   Mason, J. T.; Harsha, K. S.; Chiotti, P. *Acta Crystallogr., Sect. B: Struct. Sci* **1970**, *26*, 356-361.

(27)   Haucke, W. *Z. Anorg. Allg. Chem.* **1940**, *244*, 17-22.

(28)   Hu, B. P.; Li, H. S.; Coey, J. M. D. *J. Appl. Phys.* **1990**, *67*, 4838-4840.

(29)   Yang, Y.; Sun, H.; Kong, L.; Yang, J.; Ding, Y.; Zhang, B.; Ye, C.; Jin, L.; Zhou, H. *J. Appl. Phys.* **1988**, *64*, 5968-5970.

(30)   Bessais, L.; Djega-Mariadassou, C. *Phys. Rev. B* **2001**, *63*, 054412/1-054412/13.

(31)   Felner, I. *J. Less-Common Met.* **1980**, *72*, 241-249.

(32)   Barandiaran, J. M.; Gignoux, D.; Rodriguez-Fernandez, J.; Schmitt, D. *Physica B* **1989**, *154*, 293-299.

(33)   Bobev, S.; Fritsch, V.; Thompson, J. D.; Sarrao, J. L. *J. Solid State Chem.* **2006**, *179*, 1035-1040.

(34)   Young, D. P.; Goodrich, R. G.; DiTusa, J. F.; Guo, S.; Adams, P. W.; Chan, J. Y.; Hall, D. *Appl. Phys. Lett.* **2003**, *82*, 3713-3715.

CHAPTER 7. CRYSTAL GROWTH AND MAGNETIC PROPERTIES OF Ln_4MGa_{12} (Ln = Dy – Er; M = Pd, Pt)[*]

7.1 Introduction

Ternary intermetallic compounds consisting of RE-M-Ga (RE = Rare earth; M = transition metal) are interesting to study due to the wide range of structural features and physical properties they exhibit.[1-7] Our interest lies in finding new rare earth-based ternary intermetallic compounds, which exhibit exotic physical properties such as heavy fermion behavior[8,9] and large magnetoresistance.

Recently, An_4PdGa_{12} (An = U, Np, Pu) have been reported as new heavy fermion compounds.[10] Each compound exhibits a Sommerfeld coefficient γ = 330, 450, and 900 mJmol^{-1}K^{-2} for the U, Np, and Pu compounds, respectively. U_4PdGa_{12} also shows an antiferromagnetic transition at T_N ~ 43 K. The Np and Pu-analogues, however, do not order magnetically down to 2 K. The compounds having the stoichiometry of 4:1:12 crystallize in the cubic $Im\overline{3}m$ (No.229) space group and has been described as a redistributed homolog of the $U_4Re_7Si_6$ structure type[11] or a superstructure of the $AuCu_3$ type. Polycrystalline Ln_4MGa_{12} (Ln = Ho, Tm; M = Ni, Pd) show metallic behavior.[12] Single crystals of $Ln_4FeGa_6Ge_6$ (Ln = Sm, Tb), grown using molten gallium as a flux are isostructural to Y_4PdGa_{12}.[13] Transport measurements for the isostructural $Ln_4FeGa_6Ge_6$ (Ln = Sm, Tb) also show metallic behavior.[13] $Sm_4FeGa_6Ge_6$ does not magnetically order down to 2 K, while the Tb-analog orders antiferromagnetically at T_N = 13 K.[13] In our study with the Ln-M-Ga (Ln = lanthanide; M = Pd, Pt) system, we have been able to synthesize Tb_4MGa_{12} (M = Pd, Pt) which order antiferromagnetically at 16 K and 12 K, respectively.[2] With early lanthanides, however, we were not able to synthesize the 4-1-12 analogues with our

conditions.

Large positive magnetoresistance has also been found in other *Ln*-Pd-Ga compounds. The transport and magnetic properties in these materials are strongly coupled, and large positive magnetoresistance is often observed. $SmPd_2Ga_2$ ($ThCr_2Si_2$-type), which is composed of layers of isolated Sm atoms and layers of $PdGa_4$ edge-sharing tetrahedra alternating along the *c*-axis, orders ferromagnetically at 5 K. The low temperature (2 K) field dependent resistivity shows large positive magnetoresistance over 100 % at 9 T.[14] The low temperature (2 K) magnetoresistance of $Ce_2PdGa_{10,}$ a layered structure consisting of alternating Ce-Ga bilayers and Ga-Pd layers, increases by over 200 % at 9 T.[6] In this manuscript, we discuss the crystal growth, transport, magnetoresistance, and magnetic properties of Ln_4MGa_{12} (*Ln* = Dy, Ho, Er; *M* = Pd, Pt).

7.2 Experimental

7.2.1 Synthesis

The samples were synthesized from lanthanide (Dy, Ho, Er) pieces, palladium or platinum powder, and gallium shot, which were obtained from Alfa Aesar, all with purities greater than 99.9 %. The lanthanide (Dy, Ho, Er) pieces were combined with palladium or platinum powder and gallium pellets in a molar ratio of 1: 1: 20. The samples were then placed in alumina crucibles, sealed in a fused silica tube, and gradually heated (200 °C/hr) to 1150 °C for 7 hrs, and slow cooled (15 °C/hr) to 530 °C at which point the excess flux was removed via centrifugation. The synthesis yielded metallic single crystals which ranged in size from 0.2 to 0.5 cm^3. The crystals were stable in air.

7.2.2 Single Crystal X-ray Diffraction

Single crystal fragments of an average size of ~ 0.08 mm $\times$ 0.08 mm $\times$ 0.08 mm were

mechanically extracted, placed on a glass fiber and mounted on the goniometer of a Nonius

Kappa CCD diffractometer equipped with Mo K_α radiation ($\lambda = 0.71073$ Å). The data were then

corrected, reduced, and scaled using the SHELXL[15] software package. The structures were

solved using Tb_4PtGa_{12} as a structural model. The structure consists of four atomic positions in

which the lanthanide (*Ln*) occupies the 8*c* (1/4, 1/4, 1/4) site, the transition metal (Pd, Pt)

occupies the 2*a* (0, 0, 0) site, Ga1 the 12*d* (1/4, 0, 1/2) site, and Ga2 the 12*e* (*y*, 0, 0; where *y* = ~

0.2900) site. Additional data collection and crystallographic parameters are presented in Table

7.1. Atomic positions and thermal displacement parameters are given in Table 7.2. Selected

interatomic distances are listed in Table 7.3.

7.2.3 Physical Property Measurements

Transport and magnetic measurements were performed on single crystals of Ln_4MGa_{12}

(*Ln* = Dy, Ho, Er; *M* = Pd, Pt). The electrical resistance was measured by the standard 4-probe

AC technique at 27 Hz with a current of 1 mA. 1-mil (0.001 in) diameter Pt wires were attached

to the sample with silver epoxy. The magnetic susceptibility measurements were performed

using a Quantum Design Physical Property Measurement System. The samples were zero-field-

cooled (ZFC) to 2 K and then warmed to room temperature in a constant DC field of 1000 Gauss

(0.1 T).

7.3 Results and Discussion

7.3.1 Synthesis and Structure

Single crystals of Ln_4MGa_{12} (*Ln* = Dy, Ho, Er; *M* = Pd, Pt) were synthesized using

molten gallium as a flux. Similar to Zhuravleva *et al.*,[13] we find that a shorter isothermal ($\leq$ 3

days) step for the growth of these phases leads to the formation of the cubic phase. In addition,

upon the substitution of early rare earths such as cerium and praseodymium in the synthesis at 500 °C, we find that Ln_2PdGa_{10} (Ln = Ce, Pr) is formed.[6]

Table 7.1 Crystallographic Parameters for Ln_4MGa_{12} (Ln = Dy, Ho, Er; M = Pd, Pt)

Crystal data						
Formula	Dy_4PdGa_{12}	Dy_4PtGa_{12}	Ho_4PdGa_{12}	Ho_4PtGa_{12}	Er_4PdGa_{12}	Er_4PtGa_{12}
a (Å)	8.5700(5)	8.5630(7)	8.5490(7)	8.5400(6)	8.5300(7)	8.5350(9)
V (Å^3)	629.42(6)	627.88(9)	624.81(9)	622.84(8)	620.65(9)	621.74(11)
Z	2	2	2	2	2	2
Crystal system	Cubic	Cubic	Cubic	Cubic	Cubic	Cubic
Space group	$Im\bar{3}m$	$Im\bar{3}m$	$Im\bar{3}m$	$Im\bar{3}m$	$Im\bar{3}m$	$Im\bar{3}m$
Mosaicity (°)	0.445(6)	0.462(7)	0.445(2)	0.485(7)	0.494(9)	0.623(2)
θ range (°)	3.36-29.84	3.36-29.87	3.37-29.92	3.37-29.96	3.38-30.00	3.38-29.98
μ (mm^{-1})	49.938	59.756	51.715	61.653	53.608	63.306
Data collection						
Measured reflections	305	297	301	288	276	252
Independent reflections	113	110	114	112	114	108
Reflections with $I>2\sigma(I)$	111	108	107	109	108	104
R_{int}	0.0452	0.0566	0.0410	0.0348	0.0507	0.0430
h	-11→12	-11→11	-11→12	-11→12	-11→12	-11→11
k	-8→8	-8→8	-8→8	-8→8	-8→8	-8→8
l	-7→7	-7→7	-7→7	-7→7	-7→7	-7→7
Refinement						
$^aR_1[F^2>2\sigma(F^2)]$	0.0277	0.0338	0.0305	0.0414	0.0284	0.0268
$^bwR^2(F^2)$	0.0639	0.0720	0.0582	0.0952	0.0715	0.0642
Reflections	113	110	114	112	114	108
Parameters	10	10	10	10	10	10
$\Delta\rho_{max}$ (eÅ^{-3})	2.082	3.404	2.383	4.808	2.499	2.102
$\Delta\rho_{min}$ (eÅ^{-3})	-2.172	-1.764	-2.229	-4.797	-1.889	-1.641

$^a R_1 = \sum ||F_o| - |F_c|| / \sum |F_o|$ $^b wR_2 = [\sum [w(F_o^2 - F_c^2)]/\sum [w(F_o^2)^2]]^{1/2}$

Table 7.2 Atomic Positions and Thermal Parameters for Ln_4MGa$_{12}$ (Ln = Dy, Ho, Er; M = Pd, Pt)

Atom	Wyckoff position	x	y	z	U_{eq} (Å^2)[a]
Dy$_4$PdGa$_{12}$					
Dy	8c	1/4	1/4	1/4	0.0032(4)
Pd	2a	0	0	0	0.0055(6)
Ga1	12d	1/4	0	1/2	0.0047(5)
Ga2	12e	0.2952(2)	0	0	0.0050(5)
Dy$_4$PtGa$_{12}$					
Dy	8c	1/4	1/4	1/4	0.0059(4)
Pt	2a	0	0	0	0.0069(5)
Ga1	12d	1/4	0	1/2	0.0075(6)
Ga2	12e	0.2962(3)	0	0	0.0075(6)
Ho$_4$PdGa$_{12}$					
Ho	8c	1/4	1/4	1/4	0.0037(4)
Pd	2a	0	0	0	0.0064(6)
Ga1	12d	1/4	0	1/2	0.0049(5)
Ga2	12e	0.2952(2)	0	0	0.0057(4)
Ho$_4$PtGa$_{12}$					
Ho	8c	1/4	1/4	1/4	0.0021(6)
Pt	2a	0	0	0	0.0039(6)
Ga1	12d	1/4	0	1/2	0.0027(7)
Ga2	12e	0.2958(3)	0	0	0.0036(6)
Er$_4$PdGa$_{12}$					
Er	8c	1/4	1/4	1/4	0.0038(4)
Pd	2a	0	0	0	0.0061(7)
Ga1	12d	1/4	0	1/2	0.0047(5)
Ga2	12e	0.2953(3)	0	0	0.0054(5)
Er$_4$PtGa$_{12}$					
Er	8c	1/4	1/4	1/4	0.0092(4)
Pt	2a	0	0	0	0.0104(5)
Ga1	12d	1/4	0	1/2	0.0095(5)
Ga2	12e	0.2959(3)	0	0	0.0106(5)

[a]U_{eq} is defined as one-third of the trace of the orthogonalized U_{ij} tensor.

Table 7.3 Selected Interatomic Distances (Å) for Ln_4MGa_{12} (Ln = Dy, Ho, Er; M = Pd, Pt)

	M = Pd	M = Pt
Dy_4MGa_{12}		
Dy-Ga1 (×6)	3.02995(18)	3.0275(2)
Dy-Ga2 (×6)	3.0547(3)	3.0533(4)
M-Ga2 (×6)	2.530(2)	2.537(3)
Ho_4MGa_{12}		
Ho-Ga1 (×6)	3.0225(2)	3.0193(2)
Ho-Ga2 (×6)	3.0471(4)	3.0445(4)
M-Ga2 (×6)	2.524(2)	2.526(3)
Er_4MGa_{12}		
Er-Ga1 (×6)	3.0158(2)	3.0176(3)
Er-Ga2 (×6)	3.0404(4)	3.0429(4)
M-Ga2 (×6)	2.519(2)	2.526(2)

Dy_4PdGa_{12} consists of $PdGa_6$ octahedra corner-shared with the Ga framework and $DyGa_3$ cuboctahedra as shown in Figure 7.1. The lattice parameters of Ln_4MGa_{12} (Ln = Dy, Ho, Er; M = Pd, Pt) decrease linearly with the decrease in the rare earth atomic radii due to lanthanide contraction. The lattice parameters for the Ln_4PdGa_{12} (Ln = Dy, Ho, Er) are in agreement with those reported from polycrystalline data for Ln_4PdGa_{12} (Ln = Gd-Tm, Lu).[12] Six Ga1 atoms and six Ga2 atoms are coordinated to each lanthanide atom. The interatomic distances in the cuboctahedra of Ln_4MGa_{12} (Ln = Dy, Ho, Er; M = Pd, Pt) are listed in Table 7.3. They scale well with the summation of the values for the atomic radii of Ga (1.26 Å) and Dy (1.59 Å), Ho (1.58 Å), or Er (1.57 Å).[16] The Ln-Ga1 interatomic distances in Ln_4MGa_{12} (Ln = Dy, Ho, Er; M = Pd, Pt) are in agreement with those found in $LnGa_6$ (La - Yb)[17] and range from 3.188 Å to 3.307 Å.

Similarly, the Ln-Ga2 interatomic distances are also in agreement with those found in $LnGa_6$ (La - Yb), which range from 3.077 Å to 3.138 Å.[17] The Ga-Ga interatomic distances in Ln_4MGa_{12} (Ln = Dy, Ho, Er; M = Pd, Pt) are slightly larger than those found in the cuboctahedra
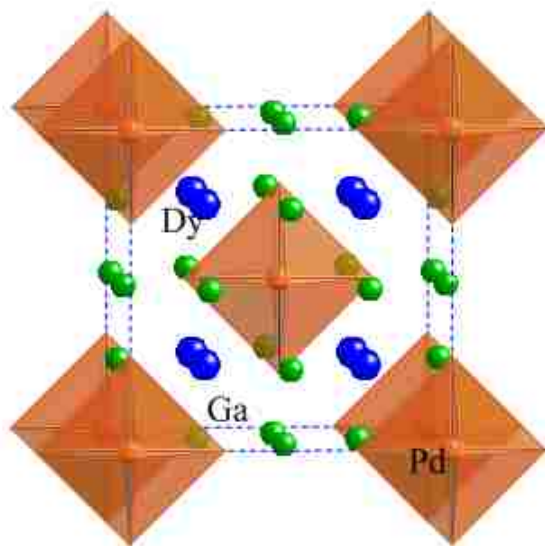
Figure 7.1   The crystal structure of Dy_4PdGa_{12} is shown along the *c*-axis.   Dysprosium, palladium, and gallium atoms are represented as blue, orange, and green spheres, respectively. The dashed lines represent the unit cell.

of *Ln*Ga_3 (La-Tm),[18] which range from 2.101 Å to 2.830 Å.   The ratio of *Ln*-Ga(1) to *Ln*-Ga(2) in each cuboctahedron is ~ 1, indicating that the cuboctahedra are highly symmetrical.

The transition metal environment in *Ln*$_4$*M*Ga_{12} (*Ln* = Dy, Ho, Er; *M* = Pd, Pt) is six-coordinate to gallium and forms *M*Ga_6 octahedra.   The interatomic distances are listed in Table 7.3.   The (Pd, Pt)-Ga interatomic distances, which range from 2.519(2) Å to 2.537(3) Å, are smaller than those reported for the $PdGa_6$ octahedra of Ce_8PdGa_{24} (2.633 Å − 2.927 Å).[19,20]   The (Pd, Pt)-Ga interatomic distance in the octahedra of Tb_4PdGa_{12} and Tb_4PtGa_{12} is 2.5444(3) Å and 2.5341(3) Å, respectively.[2]   The (Pd, Pt)-Ga interatomic distances in *Ln*$_4$*M*Ga_{12} (*Ln* = Dy, Ho, Er; *M* = Pd, Pt) are also comparable to those found in CePdGa and TbPdGa, which range from 2.5609 Å − 2.6350 Å.[21]

7.3.2 Physical Properties

Figure 7.2 shows the temperature-dependent magnetic susceptibility of single crystals of
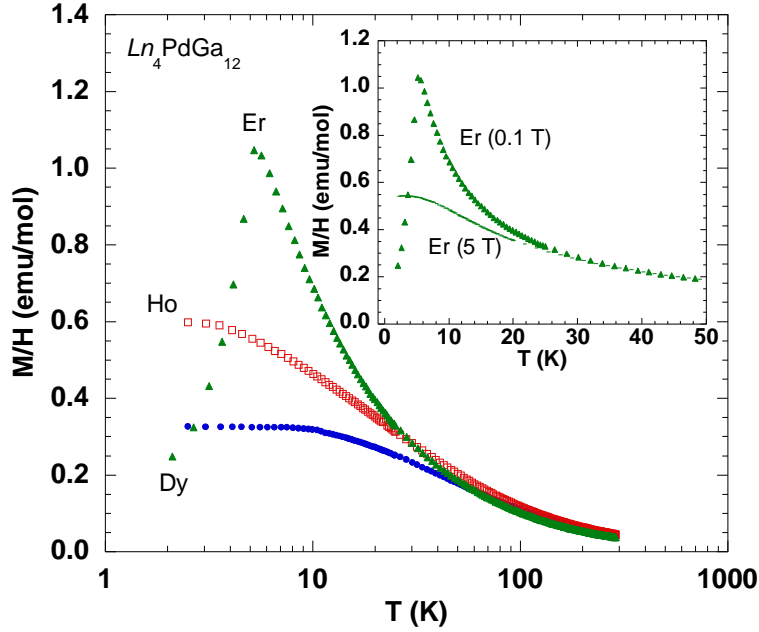
Figure 7.2 Zero-cooled magnetic susceptibility as a function of temperature of Ln_4PdGa_{12} (Ln = Dy, Ho, Er) at 0.1 T is shown. The inset shows magnetic susceptibility of Er_4PdGa_{12} at 0.1 T and 5 T.

Ln_4PdGa_{12} (Ln = Dy, Ho, Er) measured at an applied field of 0.1 Tesla. Dy_4PdGa_{12} shows magnetic ordering at 10 K. Fitting the inverse susceptibility data to a Curie-Weiss fit of the following form: $\chi(T) = C/(T - \theta)$, an effective moment of 10.53 μ_B/Dy atom was obtained, and a Weiss constant, $\theta = -27.28$ K, indicates antiferromagnetic correlations. No magnetic ordering is observed down to 2 K for Ho_4PdGa_{12} (open squares). The magnetic susceptibility data of Er_4PdGa_{12} (closed triangles) show an antiferromagnetic transition at $T_N = 5.2$ K. An effective moment of 9.47 μ_B/Er atom is obtained from the inverse magnetic susceptibility data with $\theta = -9.57$ K. The experimental moments for Dy_4PdGa_{12} and Er_4PdGa_{12} are close to the calculated values of 10.63 μ_B and 9.59 μ_B for Dy^{3+} and Er^{3+}, indicating that the magnetism in these materials is solely due to the trivalent rare earth atoms. The experimental magnetic moment of 10.48 μ_B and $\theta = -17.36$, obtained for paramagnetic Ho_4PdGa_{12} is also close to the full Hund's

value for Ho^{3+} of 10.60 μ_B. The negative Weiss constant in the Ho compound suggests antiferromagnetic correlations exist between the local moments in this system, and it could quite possibly display long-range order below 2 K.

Figure 7.3 shows the field-dependent isothermal magnetization of Ln_4PdGa_{12} (Ln = Dy, Ho, Er) measured at a constant temperature of 3 K. The magnetization for Dy_4PdGa_{12} (closed circles) increases linearly with field, which is typical for an antiferromanget. No long-range magnetic ordering for Ho_4PdGa_{12} was observed down to 2 K, and the magnetization versus field displays typical paramagnetic behavior and does not saturate up to 9 T. The magnetization of Er_4PdGa_{12}, however, (closed triangles) is very different from the other two. At low fields (< 1000 gauss) the magnetization increases more or less linearly with field. Above 5000 gauss, however, the magnetization increases sharply in a metamagnetic transition whose midpoint is ~ 1 T. Above 2 T, the magnetization displays paramagnetic behavior out to 9 T. Field-dependent
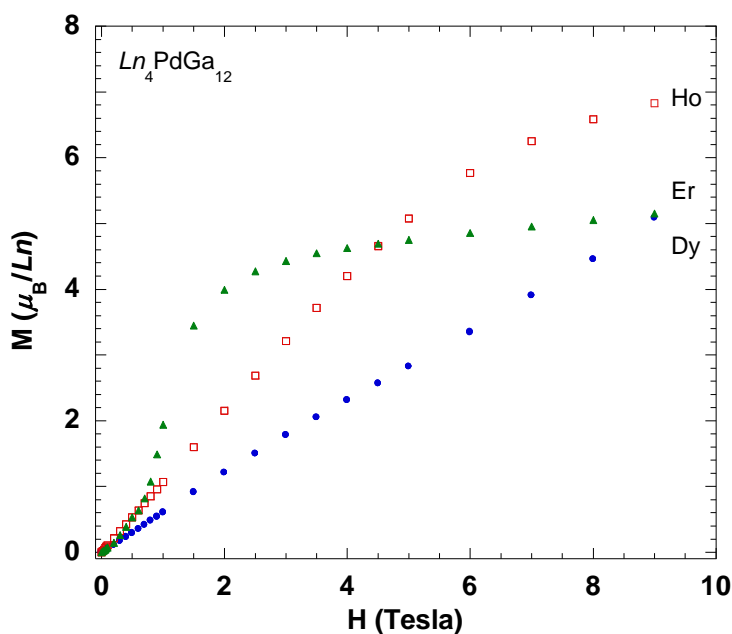
Figure 7.3 The magnetization as a function of field of Ln_4PdGa_{12} (Ln= Dy, Ho, Er) at 3 K.

neutron scattering measurements will be necessary to correctly determine the magnetic structure in this material, but the data suggest that the metamagnetism is associated with a spin-flip transition. Below T_N (Figure 7.2), the magnetization in the Er sample decreases rapidly and extrapolates to zero at zero temperature, suggesting the axis of the spins are well aligned parallel and antiparallel to the applied field (the field here being applied along one of the cubic axes directions.) As the field is increased above 5000 gauss, the spin system flips (discontinuously) to lower the energy. The transition in Fig. 7.3 is fairly broad (~ 1.5 T), since the measurement is performed at finite temperature close to T_N. A temperature sweep of the susceptibility at 5 Tesla (dashed curve, Fig. 7.2, inset) clearly shows the parallel susceptibility is completely suppressed below T_N.

The temperature-dependent magnetic susceptibility of Ln_4PtGa_{12} (Ln = Dy, Ho, Er) is shown in Figure 7.4 measured at 0.1 Tesla. We find the magnetic moment of 10.54 μ_B, 9.94 μ_B,
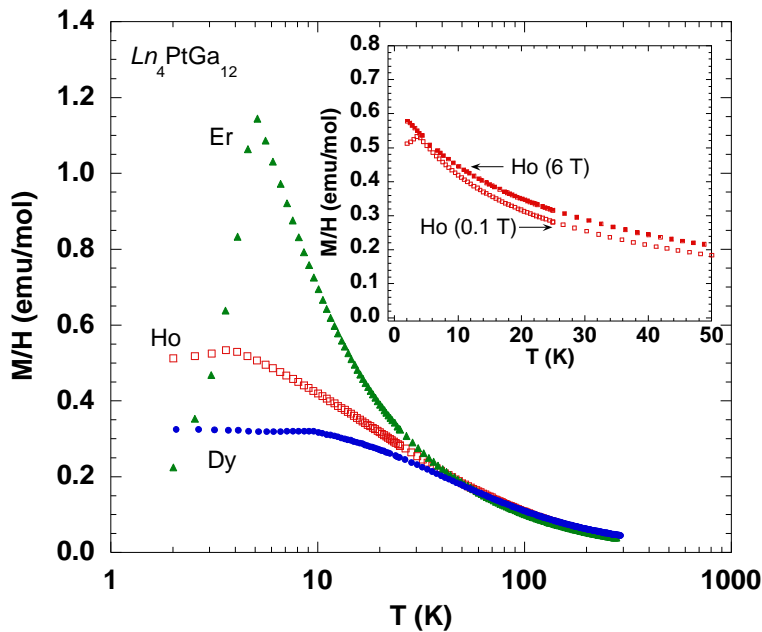
Figure 7.4 Zero-cooled magnetic susceptibility as a function of temperature of Ln_4PtGa_{12} (Ln = Dy, Ho, Er) at 0.1 T is shown. The inset shows magnetic susceptibility of Ho_4PtGa_{12} at 0.1 T and 6 T.

and 9.50 μ_B for Dy_4PtGa_{12} (closed circles), Ho_4PtGa_{12} (open squares), and Er_4PtGa_{12} (closed triangles). All three compounds order antiferromagnetically with ordering temperatures of 9.8 K, 3.6 K, and 5.1 K, respectively. The effective magnetic moments obtained for the three Pt-analogues are also close to the expected values for Dy^{3+} (10.63 μ_B), Ho^{3+} (10.60 μ_B) and Er^{3+} (9.59 μ_B). In addition, we have measured the temperature dependent magnetization of Ho_4PtGa_{12} and found that the ordering temperature disappears at 6 T. The AF behavior is destroyed and paramagnetism is recovered at high field.

The field dependent magnetization of Ln_4PtGa_{12} (Ln = Dy, Ho, Er) measured at 3 K is shown in Figure 7.5. Similar to the Pd-analog, the magnetization of Dy_4PtGa_{12} (closed circles) increases linearly with field and is typical of antiferromagnetic systems. The magnetization of Ho_4PtGa_{12} shows linearity up to 5 T and does not saturate up to 9 T. The magnetization of
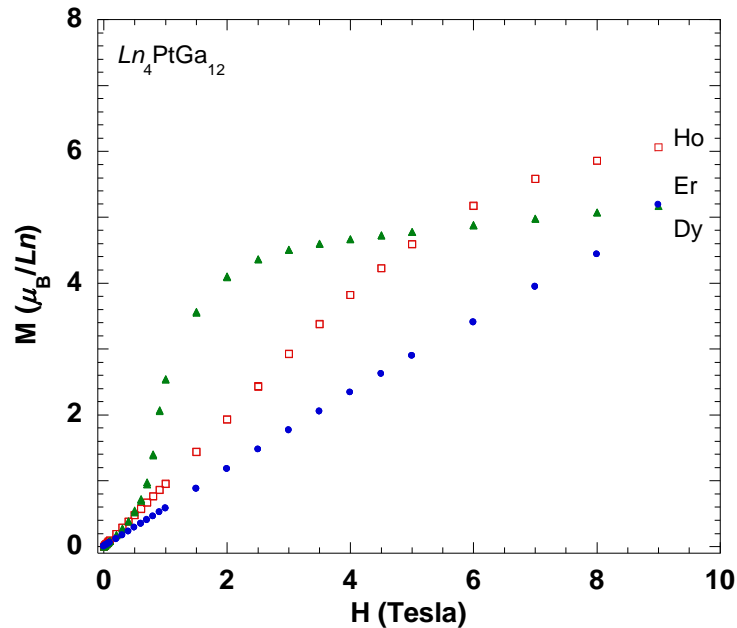
Figure 7.5 The magnetization as a function of field of Ln_4PdGa_{12} (Ln = Dy, Ho, Er) at 3 K.

Er$_4$PtGa$_{12}$ is very similar to the Pd material and shows a metamagnetic transition, again with a midpoint around 1 T. A summary of the magnetic properties of Ln_4MGa$_{12}$ (Ln = Dy, Ho, Er; M = Pd, Pt) is shown in Table 7.4.

Table 7.4 Magnetic Properties of Ln_4MGa$_{12}$ (Ln = Dy, Ho, Er; M = Pd, Pt)

	C	θ (K)	μ_{calc} (μ_B)	μ_{eff} (μ_B)	*Fit range* (K)	*Ordering* T_N (K)
Dy$_4$PdGa$_{12}$	13.858	-27.28	10.63	10.53	50-250	AFM, 10
Dy$_4$PtGa$_{12}$	13.873	-27.89	10.63	10.54	50-250	AFM, 9.8
Ho$_4$PdGa$_{12}$	13.728	-17.36	10.60	10.48	50-250	N/A
Ho$_4$PtGa$_{12}$	12.339	-15.44	10.60	9.94	50-250	AFM, 3.6
Er$_4$PdGa$_{12}$	11.216	-9.57	9.59	9.47	50-250	AFM, 5.2; MM, 1T
Er$_4$PtGa$_{12}$	11.275	-10.47	9.59	9.50	50-250	AFM, 5.1; MM, 1T

[a]Abbreviations: T_N, Néel temperature; AFM, antiferromagnetic; MM, metamagnetic.

The electrical resistivities as a function of temperature of single crystals of Ln_4PdGa$_{12}$ (Ln = Dy, Ho, Er) are shown in Figure 7.6. The samples show metallic behavior ($d\rho/dT > 0$) with RRR (residual resistivity ratio) values of 4.7, 3.3, and 3.1 for Dy$_4$PdGa$_{12}$, Ho$_4$PdGa$_{12}$ and Er$_4$PdGa$_{12}$, respectively. The inset of Fig. 7.6 shows a blow up of the low temperature resistivity data. Kinks in the resistivity are consistent with a decrease in the spin-disorder scattering at temperatures coinciding with magnetic ordering. As shown in Figure 7.7, the magnetoresistance (MR % = $(\rho_H - \rho_0)/\rho_0 \times 100$) data as a function of field of Ln_4PdGa$_{12}$ (Ln = Dy, Ho, Er) show positive values of 45 %, 10 %, and 16 % for Dy$_4$PdGa$_{12}$, Ho$_4$PdGa$_{12}$, and Er$_4$PdGa$_{12}$, respectively at 3 K and 9 T. The MR of the Er sample (open triangles) increases as H^2 until ~ 1 T, where there is a sharp peak in the MR, coinciding with the metamagnetic transition. Since the MR data were taken close to T_N, spin fluctuations in the AFM state likely play a role in the resistivity
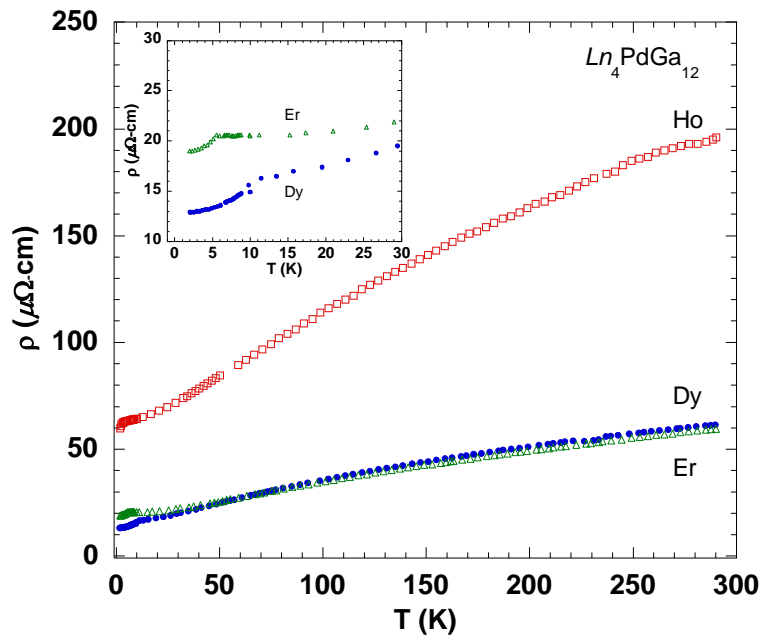
Figure 7.6 The electrical resistivity of single crystals of Ln_4PdGa_{12} (Ln = Dy, Ho, Er).
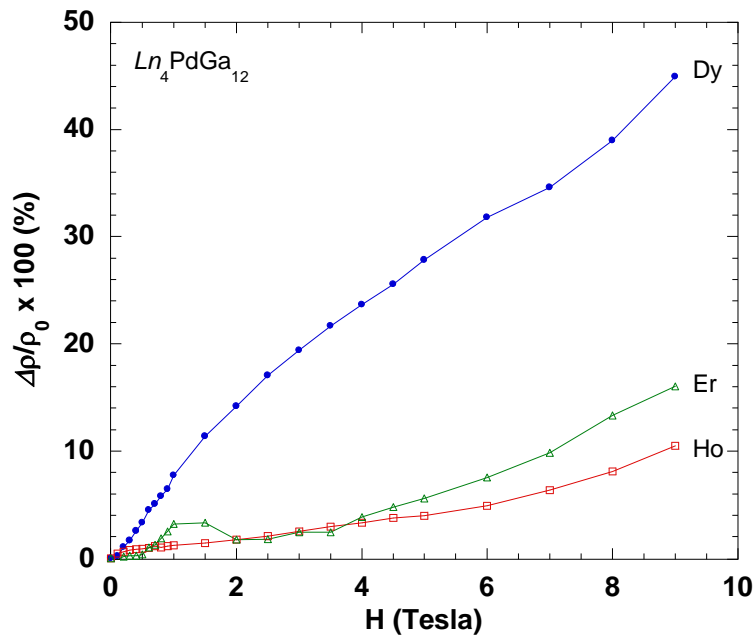
Figure 7.7 The magnetoresistance of Ln_4PdGa_{12} (Ln = Dy, Ho, Er) as a function of field at 3 K.

scattering processes. These are eliminated at higher fields above the metamagnetic transition.
Another possible explanation of the MR behavior would be field-dependent changes in the Fermi
surface topology. As such, this material is a good candidate for dHvA measurements, which we
will pursue in the near future. At fields above the metamagnetic transition, the MR is again $\sim H^2$.
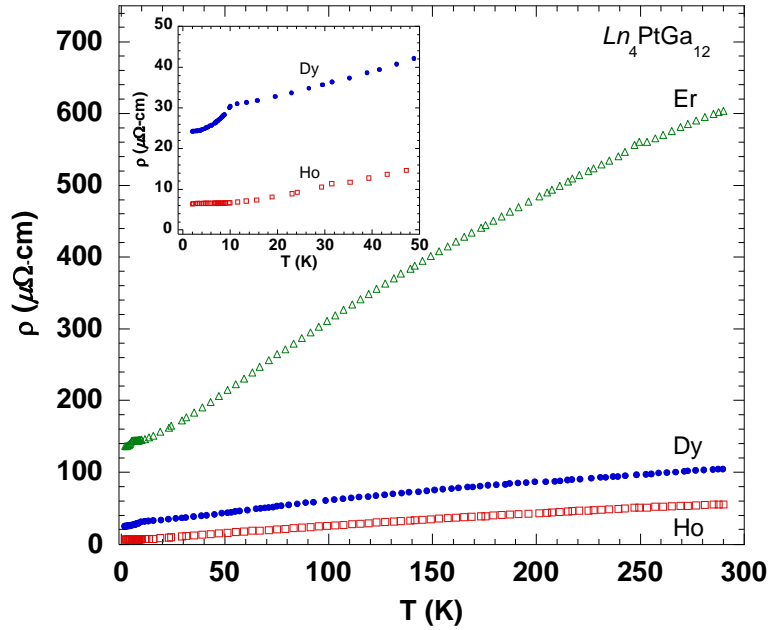
Figure 7.8 The electrical resistivity of single crystals of Ln_4PtGa_{12} (Ln = Dy, Ho, Er).

Figure 7.8 shows the electrical resistivity as a function of temperature of single crystals
of Ln_4PtGa_{12} (Ln = Dy, Ho, Er). These materials are also metallic ($d\rho/dT > 0$) with RRR
(residual resistivity ratio) values of 4.2, 8.6, and 4.4 for Dy_4PtGa_{12}, Ho_4PtGa_{12} and Er_4PtGa_{12},
respectively. A blow up (Fig. 7.8 inset) of the low temperature resistivity reveals kinks in the
data, concomitant with the Néel temperatures. The magnetoresistance of Ln_4PtGa_{12} (Ln = Dy,
Ho, Er) is shown in Figure 7.9. The Er compound (open triangles) shows behavior similar to its
Pd counterpart. A kink at the metamagnetic transition (~ 1 T) is observed, although the data do
not strictly follow H^2 behavior either below or above the transition. Interestingly, large positive
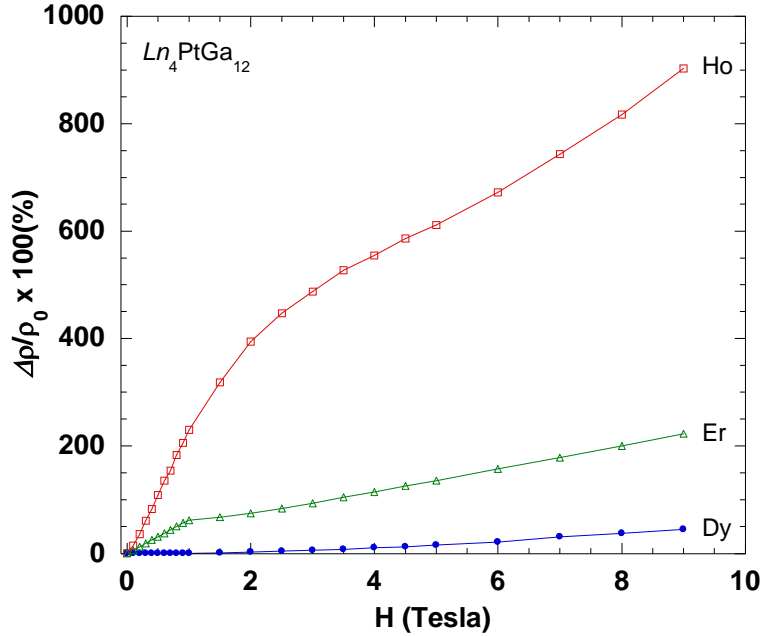
Figure 7.9 The magnetoresistance of Ln_4PtGa_{12} (Ln = Dy, Ho, Er) as a function of field at 3 K

.

MR of Ln_4PtGa_{12} (Ln = Dy, Ho, Er) with 50 %, 220 %, and 900 % at 3 K and 9 T are observed

for Dy_4PtGa_{12}, Er_4PtGa_{12} and Ho_4PtGa_{12}, respectively. Large positive magnetoresistance has

been reported in other Ln-M-Ga compounds, such as $YbCo_2Ga_8$[22] (200 % at 50 kOe/$\mu\Omega$cm and 2

K) and $SmPd_2Ga_2$[14] (100 % at 9 T and 2 K), respectively. Compared to Fig. 7.7, the data in Fig.

7.9 suggest that the MR in these two sets of materials depends sensitively upon the Pd or Pt d-

levels near the Fermi surface. The very large MR in the Ho sample is particularly interesting.

Furthermore, there are subtle features in its data set, such as the soft peak in its susceptibility

(Fig. 7.4) and the inflexion point in its MR data near 5.5 T (Fig. 7.9) that suggest that crystal

electric field (CEF) effects may be important in the analysis of its physical properties. As future

work, electronic structure calculations and field-dependent specific heat measurements can help

clarify these open questions.

7.4 References

(1)   Thomas E L, Millican J M, Okudzeto E K and Chan J Y. 2006 *Comments Inorg. Chem.* **27** 1.

(2)   Williams W M, Moldovan M, Young D P and Chan J Y. 2005 *J. Solid State Chem.* **178** 52.

(3)   Wawryk R, Henkie Z, Cichorek T, Geibel C and Steglich F. 2002 *Phys. Status Solidi B* **232** R4.

(4)   Wawryk R, Stepien-Damm J, Henkie Z, Cichorek T and Steglich F. 2004 *J. Phys.: Condens. Matter* **16** 5427.

(5)   Opahle I and Oppeneer P M. 2003 *Phys. Rev. Lett.* **90** 157001.

(6)   Millican J N, Macaluso R T, Young D P, Moldovan M and Chan J Y. 2004 *J. Solid State Chem.* **177** 4695.

(7)   Grin Y N, Yarmolyuk Y P and Gradyshevsky E I. 1979 *Kristallografiya* **24** 242.

(8)   Fisk Z, Hess D W, Pethick C J, Pines D, Smith J L, Thompson J D and Willis J O. 1988 *Science* **239** 33.

(9)   Stewart G R. 1984 *Rev. Modern Phys.* **56** 755.

(10)   Jardin R, Colineau E, Wastin F, Rebizant J and Sanchez J P. 2006 *Physica B* **378-380** 1031.

(11)   Akselrud L G, Jarmoljuk J P and Gladyshevskij E I. 1978 *Dopov Akad Nauk* 359.

(12)   Vasilenko L O, Noga A S, Grin Y N, Koterlin M D and Yarmolyuk Y P. 1988 *Russ. Metall.* **5** 216.

(13)   Zhuravleva M A, Wang X P, Schultz A J, Bakas T and Kanatzidis M G. 2002 *Inorg. Chem.* **41** 6056.

(14)   Williams W M, Moldovan M, Young D P and Chan J Y. 2003 *Inorg. Chem.* **42** 7315.

(15)   Sheldrick G M *SHELXL97: University of Göttingen*Germany, 1997.

(16)   Shannon R D. 1976 *Acta Crystallogr.* **A32** 751.

(17)   Pelleg J, Kimmel G and Dayan D. 1981 *J. Less-Common Met.* **81** 33.

(18)   Cirafici S and Franceschi E. 1981 *J. Less-Common Met.* **77** 269.

(19)   Gordon R A and DiSalvo F J. 1996 *Z. Naturforsh. B.* **51** 52.

(20)   Gordon R A, Jones C D W, Alexander M J and DiSalvo F J. 1996 *Physica B.* **225** 23.

(21)   Penc B, Szytula J, Hernandez-Velasco J and Zygmunt A. 2003 *J. Magn. Magn. Mater.* **256** 373.

(22)   Fritsch V, Bobev S, Moreno N O, Fisk Z, Thompson J D and Sarrao J L. 2004 *Phys. Rev. B: Condens. Matter* **70** 052410/1.

CHAPTER 8. SYNTHESIS, STRUCTURE, AND PHYSICAL PROPERTIES OF $LnAg_yX_{4-y}$ (Ln = La, Ce; X = Al, Ga; y ~ 0.72)[1]

8.1 Introduction

Ce-based intermetallic compounds have attracted much attention because of their interesting physical properties such as magnetism, heavy-fermion (HF) behavior, and superconductivity.[1-4] Heavy-fermions exhibit large effect masses ($m^* \approx 100$ - 1000 m_e), specific heat γ, and magnetic susceptibility (χ). These strongly correlated e⁻ systems occur as a result of competition between the local interaction of partially filled f electrons and weak interactions between f electrons and conduction electrons.[5] Among various Ce-containing intermetallic structures, Ce-based compounds adopting the $ThCr_2Si_2$ structure type have been studied extensively where the rare earth, transition metal, and Si occupy the $2a$, $4d$, and $4e$ sites, respectively. For example, $CeCu_2Si_2$ exhibits heavy-fermion superconductivity below T_C ~ 0.6 K.[6] Pressure induced heavy-fermion superconductivities have also been found for $CeCu_2Ge_2$, $CePd_2Si_2$, and $CeRh_2Si_2$ at P $\approx$ 7 GPa, 2.7 GPa, and 0.9 GPa, respectively.[7-11] Because of their robust structure, Ce-based intermetallic compounds with $ThCr_2Si_2$ structure have also been extended to Al or Ga compounds with late transition metal such as Ni, Pd, Pt, Cu, Ag, or Au.[12-21] For example, $CePd_{0.75}Ga_{3.25}$, which adopts the $ThCr_2Si_2$ structure shows a paramagnetic Curie-Weiss behavior above 80 K with no superconductivity down to 4.2 K.[22] However, $CeNi_xGa_{4-x}$ (x = 0.5 ~ 1.1) and $CeCu_2Ga_2$ order ferromagnetically at $T \approx$ 4 K and 6 K, respectively.[13,23] The $CeMAl_3$ (M = Cu, Au) compounds, which crystallize in the tetragonal $BaNiSn_3$ structure, a variant of $ThCr_2Si_2$ structure, show a Néel transition at 3 K and 1.5 K, respectively.[12,14-17] In addition, $CePtAl_3$, which also adopts the $ThCr_2Si_2$ structure, orders antiferromagnetically at 0.8

K.[15] The structures of several phases of the Ce-Ag-X (X = Al, Ga) system have also been reported.[18-21] In the Ce-Ag-Ga system, a series of polycrystalline CeAg$_x$Ga$_{4-x}$ compounds (x ~ 0.95) having the ThCr$_2$Si$_2$ structure are synthesized by arc-melting the constituents, and CeAg$_{0.65}$Ga$_{3.35}$ and CeAg$_{0.75}$Ga$_{3.25}$ among them show magnetic ordering at 3 K and 5 K, respectively.[18] However, structural refinement of CeAg$_{0.6}$Al$_{3.4}$ shows that Al atoms occupy 4d site, and this is because Ag atom is more electronegative than the Al atom.[24] In our study of Ce-based intermetallic compounds in the Ce-Ag-X (X = Al, Ga) system, we have grown single crystals of CeAg$_y$X$_{4-y}$ (X = Al, Ga; y ~ 0.72). To compare the phases to their non-magnetic analogues, crystals of LaAg$_y$X$_{4-y}$ (X = Al, Ga; y ~ 0.72) have also been synthesized. In this manuscript, we report the full structure determination of LaAg$_{0.7}$Al$_{3.3}$, magnetic susceptibility of CeAg$_{0.72}$Al$_{3.28}$ and electrical resistivities and heat capacities of LnAg$_y$X$_{4-y}$ (Ln = La, Ce; X = Al, Ga; y ~ 0.72) and will compare the properties of the Al and Ga analogues.

8.2 Experimental

8.2.1 Synthesis

Single crystals of LnAg$_y$X$_{4-y}$ (Ln = La, Ce; X = Al, Ga; y ~ 0.72) were synthesized by flux growth methods. La or Ce ingot (3N, Ames Laboratory), Ag powder (3N, Alfa Aesar), Al (5N, Alfa Aesar) and Ga (6N, Alfa Aesar) were placed into an alumina crucible in a 1:1.5:15 stoichiometric ratio. The crucible and its contents were then sealed into an evacuated fused silica tube and heated up to 1423 K for 7 h. After cooling to 773 K at a rate of 170 K/h, the tube was then slowly cooled to 673 K at a rate of 8 K/h and immediately inverted and spun with a centrifuge for the removal of excess Ga flux. The Al flux samples were etched in 6 M NaOH solution for 24 h to remove extra Al flux. Silver-color plate-like crystals were found, and typical crystal size ranged from 0.1 cm^3 to 0.5 cm^3. The crystals were not observed to degrade in air.

8.2.2 Single-Crystal X-ray Diffraction

$0.05 \times 0.05 \times 0.075$ mm^3 silver-colored fragments of $LnAg_yX_{4-y}$ (Ln = La, Ce; X = Al, Ga; $y \sim 0.72$) were mounted onto the goniometer of a Nonius KappaCCD diffractometer equipped with MoK$_\alpha$ radiation (λ = 0.71073 Å).

Table 8.1 Crystallographic Parameters for $LnAg_yX_{4-y}$ (Ln = La, Ce; X = Al, Ga; $y \sim 0.72$)

Crystal data		
Formula	LaAg$_{0.7}$Al$_{3.3}$	CeAg$_{0.72}$Al$_{3.28}$
a (Å)	4.3660(8)	4.3280(8)
c (Å)	10.9990(14)	11.0210(5)
V (Å^3)	209.66(6)	206.44(4)
Z	2	2
Crystal dimension (mm^3)	0.05×0.08×0.08	0.05×0.05×0.08
Crystal system	Tetragonal	Tetragonal
Space group	$I4/mmm$	$I4/mmm$
θ range (°)	3.70-30.01	3.70-30.03
μ (mm^{-1})	13.842	14.802
Data collection		
Measured reflections	215	306
Independent reflections	109	114
Reflections with $I > 2\sigma(I)$	109	111
R_{int}	0.0214	0.0167
h	-6→6	-6→6
k	-6→6	-4→4
l	-11→15	-15→15
Refinement		
[a]$R_1[F^2 > 2\sigma(F^2)]$	0.0141	0.0139
[b]$wR_2(F^2)$	0.0395	0.0345
Reflections	109	114
Parameters	10	10
$\Delta\rho_{max}$ (eÅ^{-3})	0.649	0.638
$\Delta\rho_{min}$ (eÅ^{-3})	-0.980	-1.077

Table 8.1 Continued

Crystal data		
Formula	LaAg$_{0.615}$Ga$_{3.385}$	CeAg$_{0.67}$Ga$_{3.33}$
a (Å)	4.3580(4)	4.3150(6)
c (Å)	10.7230(13)	10.757(2)
V (Å^3)	203.65(4)	200.29(5)
Z	2	2
Crystal dimension (mm^3)	0.05×0.05×0.08	0.05×0.05×0.08
Crystal system	Tetragonal	Tetragonal
Space group	*I*4/*mmm*	*I*4/*mmm*
θ range (°)	3.80-29.81	3.79-30.01
μ (mm^{-1})	35.029	36.206
Data collection		
Measured reflections	112	113
Independent reflections	110	109
Reflections with $I > 2\sigma(I)$	110	109
R_{int}	0.0331	0.0383
h	-6→6	-6→6
k	-4→4	-4→4
l	-14→9	-9→14
Refinement		
[a]$R_1[F^2 > 2\sigma(F^2)]$	0.0379	0.0335
[b]$wR_2(F^2)$	0.0880	0.0945
Reflections	112	113
Parameters	10	10
$\Delta\rho_{max}$ (eÅ^{-3})	3.990	2.713
$\Delta\rho_{min}$ (eÅ^{-3})	-2.741	-2.328

[a]$R_1 = \sum ||F_o| - |F_c|| / \sum |F_o|$

[b]$wR_2 = \sum [w(F_o^2 - F_c^2)] / \sum [w(F_o^2)^2]^{1/2}$

Table 8.2

(a) Atomic Positions and Thermal Parameters in $LaAg_{0.7}Al_{3.3}$ and $CeAg_{0.72}Al_{3.28}$

Atom	Wyckoff position	x	y	z	U_{eq} (Å^2)^a
La	2a	0	0	0	0.0096(3)
Al1	4d	0	1/2	1/4	0.0114(4)
T(1.4Ag2 + 2.6Al2)	4e	0	0	0.37852(8)	0.0142(4)
Ce	2a	0	0	0	0.0095(2)
Al1	4d	0	1/2	1/4	0.0088(4)
T(1.44Ag2 + 2.56Al2)	4e	0	0	0.37966(9)	0.0134(4)

(b) Atomic Positions and Thermal Parameters in $LaAg_{0.615}Ga_{3.385}$ and $CeAg_{0.67}Ga_{3.33}$

Atom	Wyckoff position	x	y	z	U_{eq} (Å^2)^a
La	2a	0	0	0	0.0072(6)
T(1.23Ag1 + 2.77Ga1)	4d	0	1/2	1/4	0.0110(6)
Ga2	4e	0	0	0.38408(12)	0.0111(6)
Ce	2a	0	0	0	0.0074(6)
T(1.34Ag1 + 2.66Ga1)	4d	0	1/2	1/4	0.0113(15)
Ga2	4e	0	0	0.38519(16)	0.0117(6)

$^aU_{eq}$ is defined as one-third of the trace of the orthogonalized U_{ij} tensor.

Table 8.3

(a) Selected Interatomic Distances (Å) of $LaAg_{0.7}Al_{3.3}$ and $CeAg_{0.72}Al_{3.28}$

$LaAg_{0.7}Al_{3.3}$		$CeAg_{0.72}Al_{3.28}$	
LaT$_4$ rectangular prism		*CeT$_4$ rectangular prism*	
La-T (×8)	3.3639(6)	Ce-T (×8)	3.3354(5)
T-T (×4) *ab*-plane	4.3660(8)	T-T (×4) *ab*-plane	4.3280(4)
T-T (×4) *c*-axis	2.6722(12)	T-T (×4) *c*-axis	2.6526(19)
T anti-square prism		*T anti-square prism*	
T-Al2 (×4)	2.6007(6)	T-Al2(×4)	2.5932(6)

T = mixed occupied by Ag or Al

(b) Selected Interatomic Distances (Å) of $LaAg_{0.615}Ga_{3.385}$ and $CeAg_{0.675}Ga_{3.325}$

$LaAg_{0.615}Ga_{3.385}$		$CeAg_{0.675}Ga_{3.325}$	
LaGa$_4$ rectangular prism		*CeGa$_4$ rectangular prism*	
La-Ga2 (×8)	3.3228(6)	Ce-Ga2	3.2916(8)
Ga2-Ga2 (×4) *ab*-plane	4.3580(4)	Ga2-Ga2 (×4) *ab*-plane	4.3150(6)
Ga2-Ga2 (×4) *c*-axis	2.486(3)	Ga2-Ga2 (×4) *c*-axis	2.470(3)
TGa$_4$ tetrahehedron		*TGa$_4$ tetrahehedron*	
T-Ga2 (×4)	2.6106(8)	T-Ga2 (×4)	2.6018(10)

T = mixed occupied by Ag or Ga

Data were collected up to $\theta = 30.0°$ at 293 K. Further crystallographic parameters for $LnAg_yX_{4-y}$ (Ln = La, Ce; X = Al, Ga; $y \sim 0.72$) are provided in Table 8.1. The space group and atomic positions from $ThCr_2Si_2$ were used as an initial structural model for the structure determination of $LnAg_yX_{4-y}$ (Ln = La, Ce; X = Al, Ga; $y \sim 0.72$) compound. The structural model was refined using SHELXL97. Data were also corrected for extinction and refined with anisotropic displacement parameters. Atomic positions and displacement parameters for both compounds are provided in Table 8.2, and selected interatomic distances are presented in Table 8.3. To ensure homogeneity and sample quality, single-crystal X-ray diffraction was performed on several single crystals from multiple batches of samples.

8.2.3 Physical Property Measurements

Magnetization data were obtained using a Quantum Design Physical Property Measurement System. The temperature-dependent magnetization data were obtained first under zero-field cooled (ZFC) conditions from 2 K to 300 K with an applied field 0.1 T. Magnetization data were then measured upon heating to obtain field-cooled (FC) data after cooling to 2 K under field. Field-dependent measurements were collected at 2 K with H swept between 0 T and 9 T. In addition, data were also collected for the crystals oriented with respect to the crystallographic axes. The electrical resistivity data were measured by the standard four-probe AC technique.

8.3 Results and Discussion

8.3.1 Structure

The structures of $CeAg_{0.72}Al_{3.28}$ and $CeAg_{0.675}Ga_{3.325}$ are shown in Figure 8.1. The $LnAg_yX_{4-y}$ (Ln = La, Ce; X = Al, Ga; $y \sim 0.72$) compounds adopt the $BaAl_4$ structure type and crystallize in the tetragonal $I4/mmm$ space group (No. 139) with Z = 2, similar to the reported

compounds $CeAg_{0.6}Al_{3.4}$ and $CeAg_{0.65}Ga_{3.35}$.[18,24] The *Ln*, Ag and Al atoms occupy the 2*a*, 4*e* and 4*d* Wyckoff positions respectively with Al also partially occupying the 4*e* sites consistent with the reported $CeAg_{0.6}Al_{3.4}$.[24] For *Ln*-Ag-Ga (*Ln* = La, Ce), Ag atoms occupy the 4*d* site with Ga partially occupying the 4*d* sites.
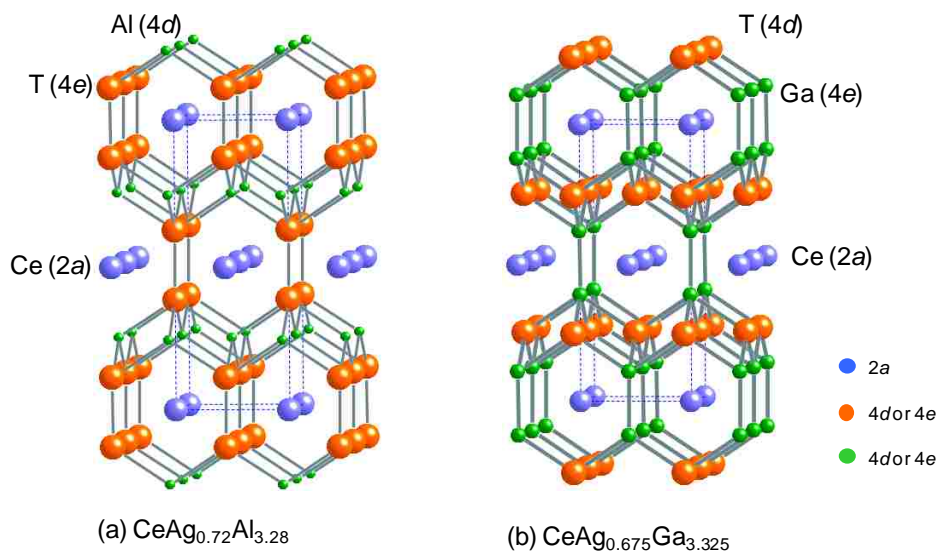
Figure 8.1 Crystal structures of (a) $CeAg_{0.32}Al_{3.28}$ and (b) $CeAg_{0.675}Ga_{3.325}$ are shown along the *c*-axis, where the blue, orange and green represent atoms occupying the 2*a* (Ce), 4*e* (T), and 4*d* (Al) positions in (a) $CeAg_{0.32}Al_{3.28}$ and the 2*a* (Ce), 4*d* (T), and 4*e* (Ga) positions in (b) $CeAg_{0.675}Ga_{3.325}$. Dashed lines are used to show the unit cell.

The structure of $CeAg_{0.72}Al_{3.28}$ can be described as consisting of layers of Ag_yAl_{4-y} and layers of Ce. In this structure, Ce atoms are surrounded by eight T (T = Ag or Al) atoms forming a face-sharing rectangular prism. Within Ce rectangular prism, interatomic distances of Ce-Ag or Ce-Al are 3.3354(5) Å in $CeAg_{0.72}Al_{3.28}$. These distances are in good agreement with Ce-Ag or Ce-Al bonds in other binary and ternary compounds such as Ce-Ag (3.242 Å ~ 3.370 Å) in CeAg, $CeAg_2$, $CeAg_{4.12}Ga_{6.88}$, and $CeAg_{1.25}Ga_{4.25}$.[21,25-28] Ce-Al distances range from 2.984 Å to 3.529 Å in CeAl, Ce_3Al, $CeAl_2$, Ce_3Al_2, $CeAl_3$ and $CeAl_4$.[29-33] The *T-T* (T = Ag or Al) and *T*-

Al2 bond distances between 2.5932 Å and 2.6526 Å in $CeAg_{0.72}Al_{3.28}$ agree with the interatomic distances in Ag-Al binaries such as Ag_2Al and Ag_3Al.[34,35]

The Ce-Ga interatomic distance of 3.2916(8) Å within Ce rectangular prism in $CeAg_{0.675}Ga_{3.325}$ is also in good agreement with typical Ce-Ga bond distances in other binary and ternary compounds such as CeGa, $CeGa_2$, Ce_3Ga_2, Ce_5Ga_3, $CeGa_6$, $CeCu_2Ga_2$, $CeAg_{4.12}Ga_{6.88}$, and $CeAg_{1.25}Ga_{4.25}$.[13,21,36-38] In addition, Ga-Ga bond distances (2.470(3) Å in $CeAg_{0.675}Ga_{3.325}$) along the *c*-axis are consistent with the sum of the covalent radii of Ga (1.25 Å) and Ga. The selected bond distances for La analogue are summarized in Table 8.3.

It is well known that transition metals prefer to occupy tetrahedral sites (4*d* sites) to avoid short transition-transition metal contacts.[39] However, in some cases such as the *Ln*-Ag-Al (*Ln* = La, Ce) and $CaZn_2Al_2$, the site preference of more electronegative atoms such as Ag and Zn occur at the vertices of tetrahedron (4*e* sites).[24,40] In $CeAg_{0.72}Al_{3.28}$, Ag atoms are positioned in the 4*e* sites with statistical occupation of 1.44Ag1 + 2.56Al1, similar to the reported stoichiometry of $CeAg_{0.6}Al_{3.4}$.[24] Atomic positions and occupancies are shown in Table 8.2. Ag and Al atoms in $CeAg_{0.72}Al_{3.28}$ ($CaZn_2Al_2$ type) result in 8 coordinated face-sharing square anti-prisms and Ag and Ga atoms in $CeAg_{0.675}Ga_{3.325}$ ($ThCr_2Si_2$ type) result in 4 coordinated edge-sharing tetrahedra. Ag atoms are surrounded by 4 *T* (*T* = Ag or Al at 4*e* sites) atoms with bond distances of 2.5932(6) Å and 2.6007(6) Å in the square anti-prisms of $CeAg_{0.72}Al_{3.28}$ and $LaAg_{0.7}Al_{3.3}$ consistent with the typical interatomic distances in Ag-Al binaries.[34,35] However, the Ag atoms in $LaAg_{0.615}Ga_{3.385}$ and $CeAg_{0.675}Ga_{3.325}$ partially occupy the 4*d* sites. Given the similarity of electronegativity, this is not unexpected. Each 4*d* site element of $CeAg_{0.675}Ga_{3.325}$ and $LaAg_{0.615}Ga_{3.385}$ is coordinated to 4 Ga atoms by bond distances of 2.6106(10) Å and 2.6018(8) Å, respectively. These bond distances are similar to typical bond distances in Ag-Ga

binaries and *Ln*-Ag-Ga ternaries, such as Ag_2Ga, $CeAg_{4.12}Ga_{6.88}$, $CeAg_{1.25}Ga_{4.25}$, and $LaAg_xGa_{4-x}$ ($X = 0.5 \sim 0.8$).[18,21,41] While electronegativity plays a role in site preferences, we note that in $SmPd_2Ga_2$[42], the more electronegative Pd atoms occupy $4d$ sites, and hence one should also consider coordination preference of transition metals.

8.3.2 Physical Properties
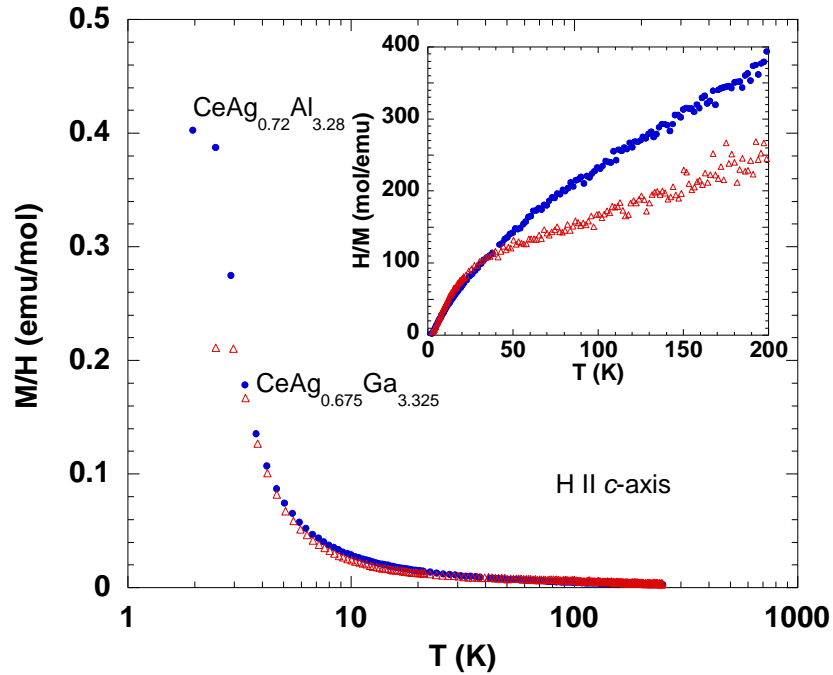
Figure 8.2 Magnetic susceptibility (emu/mol Ce) of $CeAg_{0.72}Al_{3.28}$ (blue circles) and $CeAg_{0.675}Ga_{3.325}$ (red triangles) as a function of temperature at H = 0.1 T for field along the *c*-axis. The inset shows inverse susceptibility as a function of temperature.

Temperature dependent magnetic susceptibilities of $CeAg_{0.72}Al_{3.28}$ and $CeAg_{0.675}Ga_{3.325}$ are shown in Figure 8.2. A magnetic field of 0.1 T was applied along the *c*-axis. The data show magnetic transitions ($\sim$ 3 K) for both compounds. The linear portion of the inverse magnetic susceptibility is fitted between 100 K and 200 K in $CeAg_{0.72}Al_{3.28}$ and is shown in the inset of Figure 8.2. From this linear fit, the effective moment, μ_{eff}, above transition temperature between
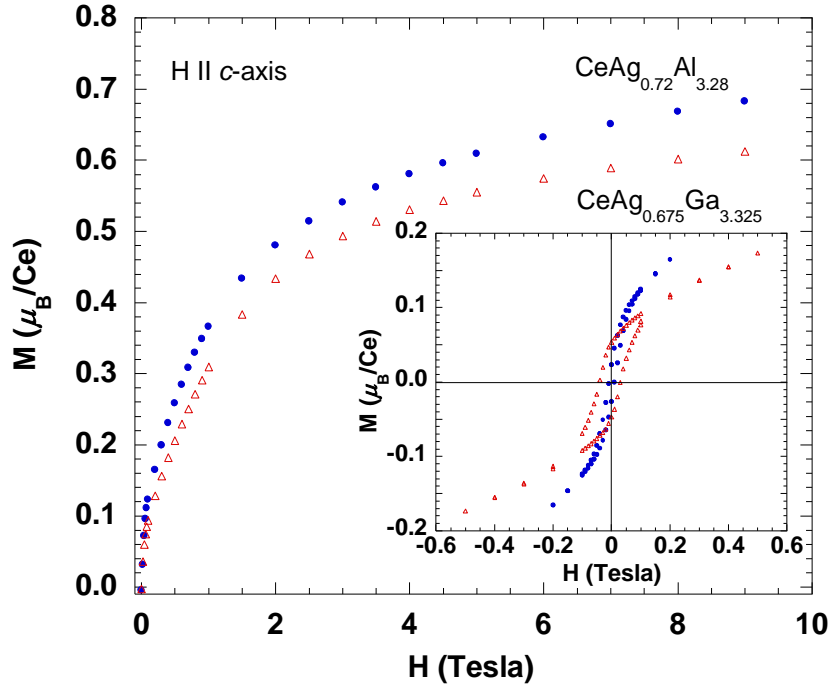
Figure 8.3 Magnetization of $CeAg_{0.72}Al_{3.28}$ (blue circles) and $CeAg_{0.675}Ga_{3.325}$ (red triangles) as a function of magnetic field at 3 K. The inset shows hysteresis as a function of field at 2 K.

100 K and 200 K is 2.35 μ_B, which is smaller than but close to the calculated Ce^{3+} moment, $\mu_{eff} =$ 2.54 μ_B, with a large (negative) Curie-Weiss temperature $\theta = -62.01$ K. Also, the inverse magnetic susceptibility for $CeAg_{0.675}Ga_{3.325}$ between 100 K and 200 K is fitted and is shown in the inset of Figure 8.2. The effective moment, μ_{eff}, above the ordering temperature between 100 K and 200 K is 2.98 μ_B with $\theta = -81.31$ K.

Figure 8.3 shows magnetization data at 3 K as a function of external magnetic field up to 9 T. The magnetization of both materials at this temperature appears paramagnetic. Above 2 T, the magnetization begins to saturate up to 0.68 μ_B and 0.62 μ_B for $CeAg_{0.72}Al_{3.28}$ and $CeAg_{0.675}Ga_{3.325}$, respectively, suggesting itinerant magnetism in these materials. However, at 2 K, hysteresis in the magnetization is observed in both materials (inset Figure 8.3), indicating ferromagnetic order with Curie temperatures between 2 K and 3 K. A coercivity (H_C) of 100 Oe

and 400 Oe are observed in $CeAg_{0.72}Al_{3.28}$ and $CeAg_{0.675}Ga_{3.325}$, respectively. The remanent magnetization, M_r, is 0.02 μ_B and 0.052 μ_B for $CeAg_{0.72}Al_{3.28}$ and $CeAg_{0.675}Ga_{3.325}$, respectively.

Figure 8.4 shows the electrical resistivity of single crystals of $LnAg_yX_{4-y}$ (Ln = La, Ce; X = Al, Ga) as a function of temperature along the ab-plane. As shown in Figure 8.4, each compound shows metallic behavior over the temperature range. The kink coincides with the magnetic ordering T_C (~ 3 K) for both Ce compounds.
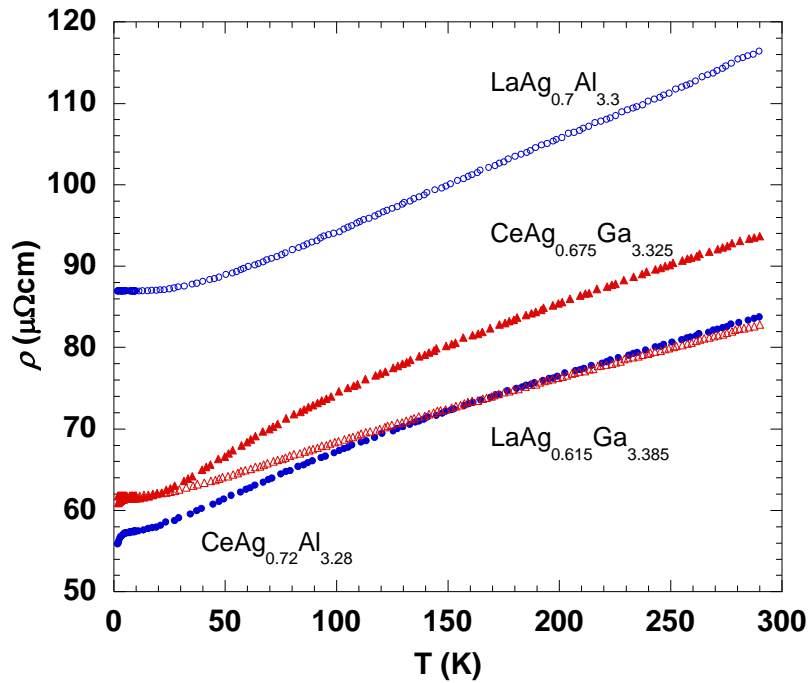
Figure 8.4 Normalized electrical resistivity of $LnAg_yX_{4-y}$ (Ln = La, Ce; X = Al, Ga) as a function of temperature. The data are measured for the current perpendicular to the c-axis.

The specific heat as a function of temperature for $LnAg_yX_{4-y}$ (Ln = La, Ce; X = Al, Ga; y ~ 0.72) at zero-field are shown in Figure 8.5. From each specific heat plot for $CeAg_{0.72}Al_{3.28}$ and $CeAg_{0.615}Ga_{3.325}$, transitions near 3 K, which are consistent with their magnetic ordering, are observed. Also, the inset of Figure 8.5 shows the magnetic contribution to the specific heat, which is found by subtracting the lattice part (non-magnetic analogue) from the total specific

heat of $CeAg_yX_{4-y}$ (X = Al, Ga; $y \sim 0.72$). The peaks are consistent with a magnetic phase transition. From the data in the inset, the magnetic contribution to the specific heat has a value
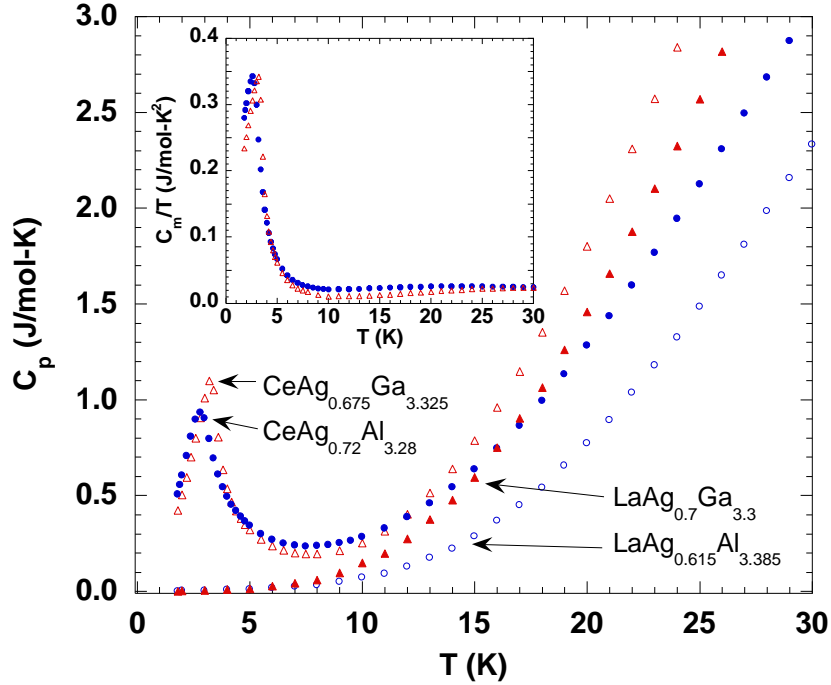
Figure 8.5 The zero-field specific heat as a function of temperature of $LnAg_yX_{4-y}$ (Ln = La, Ce; X =Al, Ga; $y \sim 0.72$).

of ~20 mJ/mol-K^2 just before the onset of the ferromagnetic transitions, indicating a slight enhancement to the effective mass.

In Figure 8.6, the field dependent specific heat is shown for $CeAg_{0.72}Al_{3.28}$. Data for the Ga analogue look similar. The sharp ferromagnetic transition near 3 K moves up in temperature with increasing field and evolves into a more second-order-like phase transition. This behavior is reminiscent of what is observed in another heavy-fermion ferromagnet, UIr_2Zn_{20}.[43] But unlike in UIr_2Zn_{20}, where the magnetic field suppresses the electronic specific heat coefficient, here we

see an enhancement with field, as increases from ~20 mJ/mol-K^2 at H = 0, to ~50 mJ/mol-K^2 at H = 9 T.
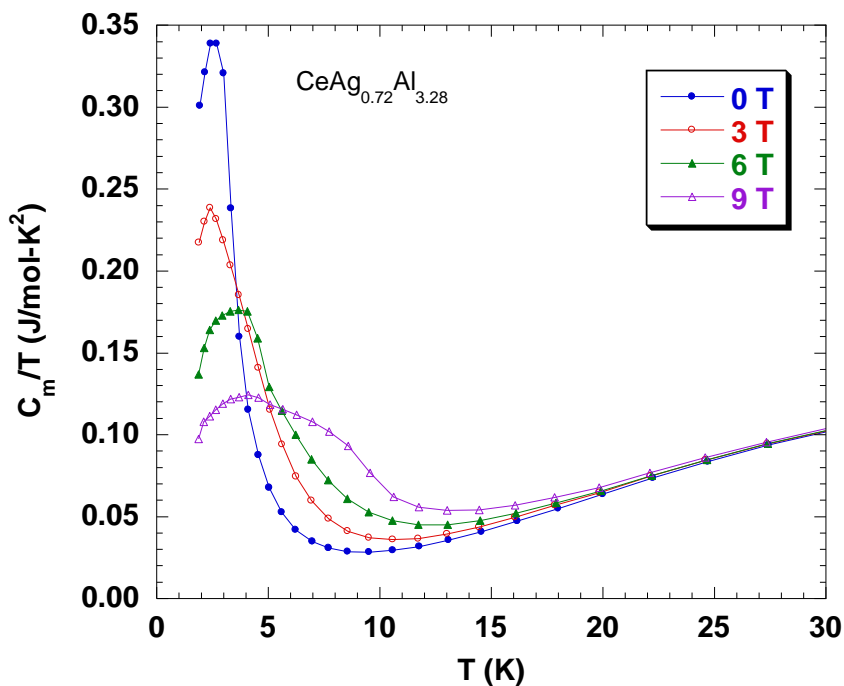
Figure 8.6 The magnetic field dependent specific heat of CeAg$_{0.72}$Al$_{3.28}$.

For future work, we plan on investigating the transport properties of the Ce compounds down to lower temperatures and screen for superconductivity both at ambient and under high pressure conditions. Both of these compounds represent rare examples of ferromagnets in this class of materials.

8.4 References

(1)   Stewart, G. R. *Rev. Mod. Phys.* **1984**, *56*, 755-787.

(2)   Fisk, Z.; Sarrao, J. L.; Smith, J. L.; Thompson, J. D. *Proc. Natl. Acad. Sci. USA* **1995**, *92*, 6663-6667.

(3)   Fisk, Z.; Sarrao, J. L.; Thompson, J. D. *Curr. Opin. Solid State Mater. Sci.* **1996**, *1*, 42-46.

(4)   Thomas, E. L.; Millican, J. N.; Okudzeto, E. K.; Chan, J. Y. *Comments Inorg. Chem.* **2006**, *27*, 1-39.

(5)   Fisk, Z.; Hess, D. W.; Pethick, C. J.; Pines, D.; Smith, J. L.; Thompson, J. D.; Willis, J. O. *Science* **1988**, *239*, 33-42.

(6)   Steglich, F.; Aarts, J.; Bredl, C. D.; Lieke, W.; Meschede, D.; Franz, W.; Schaefer, H. *Phys. Rev. Lett.* **1979**, *43*, 1892-1896.

(7)   Jaccard, D.; Behnia, K.; Sierro, J. *Phys. Lett. A* **1992**, *163*, 475-480.

(8)   Wassilew-Reul, C.; Kunz, M.; Hanfland, M.; Hausermann, D.; Geibel, C.; Steglich, F. *Physica B* **1997**, *230-232*, 310-312.

(9)   Vargoz, E.; Jaccard, D. *J. Magn. Magn. Mater.* **1998**, *177-181*, 294-295.

(10)   Movshovich, R.; Graf, T.; Mandrus, D.; Thompson, J. D.; Smith, J. L.; Fisk, Z. *Phys. Rev. B: Condens. Matter* **1996**, *53*, 8241-8244.

(11)   Grosche, F. M.; Julian, S. R.; Mathur, N. D.; Lonzarich, G. G. *Physica B* **1996**, *223&224*, 50-52.

(12)   Mentink, S. A. M.; Bos, N. M.; van Rossum, B. J.; Nieuwenhuys, G. J.; Mydosh, J. A.; Buschow, K. H. J. *J. Appl. Phys.* **1993**, *73*, 6625-6627.

(13)   Nicklas, M.; Moreno, N. O.; Borges, H. A.; Bauer, E. D.; Sarrao, J. L.; Thompson, J. D. *J. Magn. Magn. Mater.* **2004**, *272-276*, E111-E112.

(14)   Moze, O.; Buschow, K. H. J. *J. Alloys Compd.* **1996**, *245*, 112-115.

(15)   Mock, S.; Pfleiderer, C.; Lohneysen, H. v. *J. Low Temp. Phys.* **1999**, *115*, 1-14.

(16)   Paschen, S.; Felder, E.; Ott, H. R. *Eur. Phys. J. B: Condens. Matter Phys.* **1998**, *2*, 169-176.

(17)   Hulliger, F. *J. Alloys Compd.* **1995**, *218*, 255-258.

(18)   Grin, Y. N.; Hiebl, K.; Rogl, P.; Eibler, R. *J. Less-Common Met.* **1986**, *115*, 367-372.

(19)   Denysyuk, O. V.; Stel'makhovych, B. M.; Kuz'ma, Y. B. *J. Solid State Chem.* **1994**, *109*, 172-174.

(20)   Zhak, O. V.; Stel'makhovich, B. M.; Kuz'ma, y. B. *Metally* **1995**, 158-161.

(21)   Gumeniuk, R. V.; Akselrud, L. G.; Stel'makhovych, B. M.; Kuz'ma, Y. B. *J. Alloys Compd.* **2005**, *389*, 127-132.

(22) Grin, Y. N.; Rogl, P.; Hiebl, K.; Eibler, R. *J. Less-Common Met.* **1986**, *118*, 335-342.

(23) Sampathkumaran, E. V.; Das, I. *Solid State Commun.* **1992**, *81*, 901-904.

(24) Cordier, G.; Doersam, G.; Roehr, C. *J. Less-Common Met.* **1990**, *166*, 115-124.

(25) Stratton, R. P.; Kitchingman, W. J. *Acta Cryst.* **1964**, *17*, 1471.

(26) Dwight, A. E.; Downey, J. W.; Conner, R. A., Jr. *Acta Cryst.* **1967**, *23)(Pt 5*, 860-862.

(27) Steeb, S.; Godel, D.; Loehr, C. *J. Less-Common Met.* **1968**, *15*, 137-141.

(28) Delfino, S.; Ferro, R.; Capelli, R.; Borsese, A. *J. Less-Common Met.* **1975**, *41*, 59-64.

(29) Becle, C.; Lemaire, R. *Acta Cryst.* **1967**, *23*, 840-846.

(30) Havinga, E. E. *J. Less-Common Met.* **1975**, *41*, 241-254.

(31) Asmat, H.; Barbara, B.; Gignoux, D. *J. Solid State Chem.* **1977**, *22*, 179-184.

(32) Rao, B. A.; Kistaiah, P.; Reddy, N. R. S.; Murthy, K. S. *J. Less-Common Met.* **1983**, *95*, 93-97.

(33) Cordier, G.; Doersam, G.; Henseleit, R.; Mehner, A.; Thies, S.; Geibel, C. *J. Alloys Compd.* **1992**, *186*, 161-175.

(34) Neumann, J. P.; Chang, Y. A. *Trans. Met. Soc. AIME* **1968**, *242*, 700-702.

(35) El-Boragy, M.; Schubert, K. *Z. MetaIlkd.* **1971**, *62*, 667-675.

(36) Dayan, D.; Pelleg, J.; Guisser, R. *J. Less-Common Met.* **1979**, *68*, 199-205.

(37) Yatsenko, S. P.; Semyannikov, A. A.; Semenov, B. G.; Chuntonov, K. A. *J. Less-Common Met.* **1979**, *64*, 185-199.

(38) Kimmel, G.; Dayan, D.; Grill, A.; Pelleg, J. *J. Less-Common Met.* **1980**, *75*, 133-140.

(39) Parthe, E.; Chabot, B. *Handbook on the Physics and Chemistry of Rare Earths*; Elsevier Science Publishers B. V., 1984.

(40) Cordier, G.; Czech, E.; Schaefer, H. *Z. Naturforsch.* **1984**, *39B*, 1629-1632.

(41) Halder, S. K.; Sen Gupta, S. P. *Acta Crystallogr., Sect. A: Found. Crystallogr.* **1974**, *A30*, 844-845.

(42)   Williams, W. M.; Macaluso, R. T.; Moldovan, M.; Young, D. P.; Chan, J. Y. *Inorg. Chem.* **2003**, *42*, 7315-7318.

(43)   E. D. Bauer,; A. D. Christianson,; J. S. Gardner,; V. A. Sidorov,; J. D. Thompson,; J. L. Sarrao,; M. F. Hundley, *Phys. Rev. B: Condens. Matter* **2006**, *74*, 155118/1-155118/6.

APPENDIX 1. LETTERS OF PERMISSION TO USE THE COPYRIGHTED MATERIAL

American Chemical Society

Publications Division
Copyright Office

VIA FAX: 225-578-3458   DATE: September 25, 2008

1155 Sixteenth Street, NW
Washington, DC 20036
Phone: (1) 202-872-4368 or -4367
Fax: (1) 202-776-8112 E-mail: copyright@acs.org

TO: Jung Young Cho, Department of Chemistry, Louisiana State University
       232 Choppin Hall, Baton Rouge, LA 70803

FROM: C. Arleen Courtney, Copyright Associate   *C. Arleen Courtney*

Thank you for your request for permission to include **your** paper(s) or portions of text from **your** paper(s) in your thesis. Permission is now automatically granted; please pay special attention to the implications paragraph below. The Copyright Subcommittee of the Joint Board/Council Committees on Publications approved the following:

Copyright permission for published and submitted material from theses and dissertations
ACS extends blanket permission to students to include in their theses and dissertations their own articles, or portions thereof, that have been published in ACS journals or submitted to ACS journals for publication, provided that the ACS copyright credit line is noted on the appropriate page(s).

Publishing implications of electronic publication of theses and dissertation material
Students and their mentors should be aware that posting of theses and dissertation material on the Web prior to submission of material from that thesis or dissertation to an ACS journal **may** affect publication in that journal. Whether Web posting is considered prior publication may be evaluated on a case-by-case basis by the journal's editor. If an ACS journal editor considers Web posting to be "prior publication", the paper will not be accepted for publication in that journal. If you intend to submit your unpublished paper to ACS for publication, check with the appropriate editor prior to posting your manuscript electronically.

If your paper has **not yet been published by ACS**, we have no objection to your including the text or portions of the text in your thesis/dissertation in **print and microfilm formats**; please note, however, that electronic distribution or Web posting of the unpublished paper as part of your thesis in electronic formats might jeopardize publication of your paper by ACS. Please print the following credit line on the first page of your article: "Reproduced (or 'Reproduced in part') with permission from [JOURNAL NAME], in press (or 'submitted for publication'). Unpublished work copyright [CURRENT YEAR] American Chemical Society." Include appropriate information.

If your paper has already been published by ACS and you want to include the text or portions of the text in your thesis/dissertation in **print or microfilm formats**, please print the ACS copyright credit line on the first page of your article: "Reproduced (or 'Reproduced in part') with permission from [FULL REFERENCE CITATION.] Copyright [YEAR] American Chemical Society." Include appropriate information.

Submission to a Dissertation Distributor: If you plan to submit your thesis to UMI or to another dissertation distributor, you should not include the unpublished ACS paper in your thesis if the thesis will be disseminated electronically, until ACS has published your paper. After publication of the paper by ACS, you may release the entire thesis (**not the individual ACS article by itself**) for electronic dissemination through the distributor; ACS's copyright credit line should be printed on the first page of the ACS paper.

Use on an Intranet: The inclusion of your ACS unpublished or published manuscript is permitted in your thesis in print and microfilm formats. If ACS has published your paper you may include the manuscript in your thesis on an intranet that is **not** publicly available. Your ACS article cannot be posted electronically on a publicly available medium (i.e. one that is not password protected), such as but not limited to, electronic archives, Internet, library server, etc. The only material from your paper that can be posted on a public electronic medium is the article abstract, figures, and tables, and you may link to the article's DOI or post the article's author-directed URL link provided by ACS. This paragraph does not pertain to the dissertation distributor paragraph above.   06/07/06

To whom it may concern:

I am Jung Young Cho at Louisiana State University. I would like to request copyright permissions for the full reference citation to my dissertation for Ph. D. I published one paper to IOP ("Crystal growth and magnetic properties of Ln4MGa12 (Ln = Dy-Er; M = Pd, Pt)", J. Phys.: Condens. Matter, 19, (2007), 266224(11pp)). My mailing address and fax number are below. Thank you.

—

Cho, Jung Young
Ph.D. Candidate
Louisiana State University
Department of Chemistry
232 Choppin Hall
Baton Rouge, LA 70803-1804
Lab: (225)578-5380
Fax: (225)578-3458

PERMISSION TO REPRODUCE AS REQUESTED
IS GIVEN PROVIDED THAT:

(a) the consent of the author(s) is obtained.
(b) the source of the material including author/editor, title, date and publisher is acknowledged. ⊛

IOP Publishing Ltd
Dirac House
Temple Back
BRISTOL
BS1 6BE

Date 12/9/28

Rights & Permissions

⊛ Please include the IOP copyright line, mention the journal homepage at: www.iop.org/journals/jpcm and provide a link back to the article's abstract on our website from the electronic version of your thesis (if applicable).

Thank you!

ELSEVIER LICENSE
TERMS AND CONDITIONS

Sep 16, 2008

This is a License Agreement between Jung Young Cho ("You") and Elsevier ("Elsevier"). The license consists of your order details, the terms and conditions provided by Elsevier, and the payment terms and conditions.

Supplier	Elsevier Limited The Boulevard,Langford Lane Kidlington,Oxford,OX5 1GB,UK
Registered Company Number	1982084
Customer name	Jung Young Cho
Customer address	Louisiana State University Baton Rouge, LA 70803
License Number	2030790380554
License date	Sep 16, 2008
Licensed content publisher	Elsevier
Licensed content publication	Physica B: Condensed Matter
Licensed content title	Physical properties of $LnAg_yX_{4-y}$ (Ln=La, Ce; X=Al, Ga; y&#x
Licensed content author	Jung Young Cho, Monica Moldovan, David P. Young, Nathan D. Lowhorn and Julia Y. Chan
Licensed content date	1 April 2008
Volume number	403
Issue number	5-9
Pages	2
Type of Use	Thesis / Dissertation
Portion	Full article
Format	Both print and electronic
You are an author of the Elsevier article	Yes
Are you translating?	No
Purchase order number	
Expected publication date	Dec 2008
Elsevier VAT number	GB 494 6272 12
Permissions price	0.00 USD
Value added tax 0.0%	0.00 USD

Total   0.00 USD
Terms and Conditions

INTRODUCTION

1. The publisher for this copyrighted material is Elsevier. By clicking "accept" in connection with completing this licensing transaction, you agree that the following terms and conditions apply to this transaction (along with the Billing and Payment terms and conditions established by Copyright Clearance Center, Inc. ("CCC"), at the time that you opened your Rightslink account and that are available at any time at <http://myaccount.copyright.com>).

GENERAL TERMS

2. Elsevier hereby grants you permission to reproduce the aforementioned material subject to the terms and conditions indicated.

3. Acknowledgement: If any part of the material to be used (for example, figures) has appeared in our publication with credit or acknowledgement to another source, permission must also be sought from that source. If such permission is not obtained then that material may not be included in your publication/copies. Suitable acknowledgement to the source must be made, either as a footnote or in a reference list at the end of your publication, as follows:

"Reprinted from Publication title, Vol /edition number, Author(s), Title of article / title of chapter, Pages No., Copyright (Year), with permission from Elsevier [OR APPLICABLE SOCIETY COPYRIGHT OWNER]." Also Lancet special credit - "Reprinted from The Lancet, Vol. number, Author(s), Title of article, Pages No., Copyright (Year), with permission from Elsevier."

4. Reproduction of this material is confined to the purpose and/or media for which permission is hereby given.

5. Altering/Modifying Material: Not Permitted. However figures and illustrations may be altered/adapted minimally to serve your work. Any other abbreviations, additions, deletions and/or any other alterations shall be made only with prior written authorization of Elsevier Ltd. (Please contact Elsevier at permissions@elsevier.com)

6. If the permission fee for the requested use of our material is waived in this instance, please be advised that your future requests for Elsevier materials may attract a fee.

7. Reservation of Rights: Publisher reserves all rights not specifically granted in the combination of (i) the license details provided by you and accepted in the course of this licensing transaction, (ii) these terms and conditions and (iii) CCC's Billing and Payment terms and conditions.

8. License Contingent Upon Payment: While you may exercise the rights licensed immediately upon

issuance of the license at the end of the licensing process for the transaction, provided that you have disclosed complete and accurate details of your proposed use; no license is finally effective unless and until full payment is received from you (either by publisher or by CCC) as provided in CCC's Billing and Payment terms and conditions. If full payment is not received on a timely basis, then any license preliminarily granted shall be deemed automatically revoked and shall be void as if never granted. Further, in the event that you breach any of these terms and conditions or any of CCC's Billing and Payment terms and conditions, the license is automatically revoked and shall be void as if never granted. Use of materials as described in a revoked license, as well as any use of the materials beyond the scope of an unrevoked license, may constitute copyright infringement and publisher reserves the right to take any and all action to protect its copyright in the materials.

9. Warranties: Publisher makes no representations or warranties with respect to the licensed material.

10. Indemnity: You hereby indemnify and agree to hold harmless publisher and CCC, and their respective officers, directors, employees and agents, from and against any and all claims arising out of your use of the licensed material other than as specifically authorized pursuant to this license.

11. No Transfer of License: This license is personal to you and may not be sublicensed, assigned, or transferred by you to any other person without publisher's written permission.

12. No Amendment Except in Writing: This license may not be amended except in a writing signed by both parties (or, in the case of publisher, by CCC on publisher's behalf).

13. Objection to Contrary Terms: Publisher hereby objects to any terms contained in any purchase order, acknowledgment, check endorsement or other writing prepared by you, which terms are inconsistent with these terms and conditions or CCC's Billing and Payment terms and conditions. These terms and conditions, together with CCC's Billing and Payment terms and conditions (which are incorporated herein), comprise the entire agreement between you and publisher (and CCC) concerning this licensing transaction. In the event of any conflict between your obligations established by these terms and conditions and those established by CCC's Billing and Payment terms and conditions, these terms and conditions shall control.

14. Revocation: Elsevier or Copyright Clearance Center may deny the permissions described in this License at their sole discretion, for any reason or no reason, with a full refund payable to you. Notice of such denial will be made using the contact information provided by you. Failure to receive such notice will not alter or invalidate the denial. In no event will Elsevier or Copyright Clearance Center be responsible or liable for any costs, expenses or damage incurred by you as a result of a denial of your permission request, other than a refund of the amount(s) paid by you to Elsevier and/or Copyright Clearance Center for denied permissions.

LIMITED LICENSE

The following terms and conditions apply to specific license types:

15. **Translation**: This permission is granted for non-exclusive world **English** rights only unless your license was granted for translation rights. If you licensed translation rights you may only translate this content into the languages you requested. A professional translator must perform all translations and reproduce the content word for word preserving the integrity of the article. If this license is to re-use 1 or 2 figures then permission is granted for non-exclusive world rights in all languages.

16. **Website**: The following terms and conditions apply to electronic reserve and author websites:
Electronic reserve: If licensed material is to be posted to website, the web site is to be password-protected and made available only to bona fide students registered on a relevant course if:
This license was made in connection with a course,
This permission is granted for 1 year only. You may obtain a license for future website posting,
All content posted to the web site must maintain the copyright information line on the bottom of each image,
A hyper-text must be included to the Homepage of the journal from which you are licensing at http://www.sciencedirect.com/science/journal/xxxxx or the Elsevier homepage for books at http://www.elsevier.com , and
Central Storage: This license does not include permission for a scanned version of the material to be stored in a central repository such as that provided by Heron/XanEdu.

17. **Author website** for journals with the following additional clauses:
This permission is granted for 1 year only. You may obtain a license for future website posting,
All content posted to the web site must maintain the copyright information line on the bottom of each image, and
The permission granted is limited to the personal version of your paper. You are not allowed to download and post the published electronic version of your article (whether PDF or HTML, proof or final version), nor may you scan the printed edition to create an electronic version.
A hyper-text must be included to the Homepage of the journal from which you are licensing at http://www.sciencedirect.com/science/journal/xxxxx , or the Elsevier homepage for books at http://www.elsevier.com and
Central Storage: This license does not include permission for a scanned version of the material to be stored in a central repository such as that provided by Heron/XanEdu.

18. **Author website** for books with the following additional clauses:
Authors are permitted to place a brief summary of their work online only.
A hyper-text must be included to the Elsevier homepage at http://www.elsevier.com
This permission is granted for 1 year only. You may obtain a license for future website posting,
All content posted to the web site must maintain the copyright information line on the bottom of each image, and
The permission granted is limited to the personal version of your paper. You are not allowed to download and post the published electronic version of your article (whether PDF or HTML, proof or final version), nor may you scan the printed edition to create an electronic version.
A hyper-text must be included to the Homepage of the journal from which you are licensing at http://

www.sciencedirect.com/science/journal/xxxxx , or the Elsevier homepage for books at http://www. elsevier.com and

Central Storage: This license does not include permission for a scanned version of the material to be stored in a central repository such as that provided by Heron/XanEdu.

19. **Website** (regular and for author): "A hyper-text must be included to the Homepage of the journal from which you are licensing at http://www.sciencedirect.com/science/journal/xxxxx."

20. **Thesis/Dissertation**: If your license is for use in a thesis/dissertation your thesis may be submitted to your institution in either print or electronic form. Should your thesis be published commercially, please reapply for permission. These requirements include permission for the Library and Archives of Canada to supply single copies, on demand, of the complete thesis and include permission for UMI to supply single copies, on demand, of the complete thesis. Should your thesis be published commercially, please reapply for permission.

v1.2

21. **Other conditions:**

None

VITA

Jung Young Cho was born in December, 1974, to his parents Yong Jik Cho and Young Sook Kwon in Puyeo, South Korea. He is the youngest of six children and the husband of Eun Jeong Choi of Kwang Ju, South Korea. Jung Young graduated from Chung-Nam high school in February, 1993. He then attended Chung-Ang University in Seoul, South Korea, where he was motivated by science and received a Bachelor of Science degree in chemistry in February, 2001. He decided to extend his academic career by joining the inorganic research group of Professor Il-wun Shim at Chung-Ang University. After he received his Master of Science degree in chemistry in February, 2003, he came to the United States and joined the group of Professor Julia Y. Chan at Louisiana State University in January 2005.

During his doctoral study at Louisiana State University, Jung Young attended several national meetings and a workshop: the International Conference on Strongly Correlated Electron Systems in Houston, Texas (2007), NIST workshop on Representational Analysis of Complex Magnetic Structures (2007), the 235th ACS National Meeting & Exposition in New Orleans, Louisiana (2008), the 25th Rare Earth Research Conference in Tuscaloosa, Alabama (2008), the Gordon Research Conference (Solid State Chemistry) in New London, New Hampshire (2008). He also earned several awards: a Strongly Correlated Electron Systems Conference Young Investigator Award (2007), a Research Scholar for Outstanding Research Achievement (2007), a LSU Dissertation Fellowship Award (2007), an I2CAM Travel Award (2008), and a Coates Travel Award (2008). He also served as a vice president of Korean Student Association (2005-2006).

Jung Young will graduate from Louisiana State University on December 19, 2008, and be awarded with a Doctor of Philosophy degree in chemistry.